PhD_Thesis_Ashok_Kumar_combined_for_plag_check.pdf

by Ashok Kumar

Submission date: 19-Jun-2026 02:20PM (UTC+0530)
Submission ID: 2985988988
File name: PhD_Thesis_Ashok_Kumar_combined_for_plag_check.pdf (8.45M)
Word count: 36660
Character count: 199567

Chapter 1

Introduction

1.1 Introduction

Rare-earth orthovanadates, particularly $LaVO_4$ and its Nb-substituted derivatives, have received substantial interest for their outstanding multifunctional capabilities. The materials of these groups have excellent electrical and optical properties that is due to its flexible crystal chemistry and structural polymorphism which makes them suitable for variety of industrial applications. Its main applications include fuel cells [1], solid-state lasers, dielectric ceramics and photocatalysis [2]. These orthovanadates are linked inside multiple lattice framework which consist of Tetrahedral VO_4^{3-} units. There are various methods to enhance its stability and characteristics such as changing the synthesis method, temperature and modifying ionic substitution.

$LaVO_4$ have monoclinic monazite type crystal structure having space group $P2_1/n$ with a twisted network of VO_4 tetrahedra and a LaO_9 polyhedra at room temperature [3]. Distortion is seen in this low-symmetry structure when isovalent or aliovalent type of dopants are added to these structures. On the other hand, $LaNbO_4$ have a scheelite-type tetragonal structure that contains more LaO_8 coordination [4]. The comparable synthesis and doping circumstances of these two substances opens up new ideas for structural and property manipulation for them. The substitution of Nb^{5+} at the V^{5+} site in $LaVO_4$ is of specific interest because both cations share the same oxidation state but differ in ionic radius and electronic configuration [5]. This enables the tuning of crystal field effects, defect chemistry, and bonding characteristics. The introduction of Nb into the lattice imposes a form of internal strain often referred to as 'chemical pressure,' resulting in phase transitions from the native monazite phase to scheelite and, at higher doping or thermal conditions, to fergussonite (I2/a) phase [6]. These phase transitions are often accompanied by a significant change in dielectric, optical, and electrical behaviour, thus enabling phase-engineering as a strategic route to functional optimization.

Structurally, the ability to engineer $LaV_{1-x}Nb_xO_4$ compositions along the monazite–scheelite–fergussonite continuum allows precise tuning of the local symmetry, bond

angles, and lattice parameters. Such transitions are detectable by X-ray diffraction (XRD) and Raman spectroscopy and are further validated by Rietveld refinement, which reveals shifts in lattice constants and changes in site occupancy. The transition from monoclinic to tetragonal symmetry is often driven by the size mismatch between V and Nb and the enhanced polarization of Nb–O bonds [7].

From a materials science standpoint, these transitions affect not only the macroscopic structure but also the local defect chemistry. Nb^{5+} Doping produces oxygen vacancies by charge compensation or lattice accommodation, which influences electrical conductivity and dielectric characteristics. The resulting materials feature mixed conduction routes, with both ionic and electronic contributions, making them ideal for applications like as fuel cells and sensors. $LaVO_4$'s large bandgap (3.5 - 4.2 eV) restricts its photocatalytic activity to UV light [8]. However, Nb doping reduces the bandgap by forcing the Nb-4d orbitals to hybridise with the already present V - 3d and O - 2p states. This enhances apparent absorption and improves the efficiency of photocatalytic degradation for organic dyes. Furthermore, this bandgap modulation is critical in modifying dielectric relaxation behaviour at high frequencies.

The goal of this study is to synthesise and analyse the structure-property relationships of $LaV_{1-x}Nb_xO_4$ molecules ($0 \leq x \leq 1$), to understand the fundamental principles underlying improved performance through complete research that includes structural characterisation (XRD, Raman, XPS), morphological investigations (SEM, TEM), and dielectric/impedance measurements. In addition, the emphasis is on phase identification, relaxation processes, grain-boundary contributions, and conductivity modelling using Jonscher's power law [9] and equivalent circuit fitting.

The chapter provides background for the investigation by summarising previous work on $LaVO_4$, $LaNbO_4$, and their derivatives. It seeks to provide the scientific justification for Nb doping, detail known structure-property connections, and identify literature gaps that this study fills. The following parts provide an extensive literature overview, theoretical analysis, and discussion of potential applications.

1.2 Structural Polymorphism of $LaVO_4$ and Related Compounds

The structural polymorphism observed in $LaVO_4$ and its niobium-substituted derivatives is one of most crucial factors governing their functional performance in various technological domains. This polymorphism refers to the existence of the same compound in more than one crystal structure, each with distinct symmetries, coordination environments, and bonding configurations. The ability to tailor these phases through doping, synthesis route, or thermal treatment has made $LaV_{1-x}Nb_xO_4$ systems a rich subject for research in advanced ceramics [10].

At ambient conditions, $LaVO_4$ typically adopts monoclinic monazite-type structure (space group $P2_1/n$), which exhibits lower symmetry and a greater degree of flexibility in accommodating lattice distortions and ionic substitutions [3]. However, depending on processing conditions and compositional changes, especially via substitution of V^{5+} with Nb^{5+}, $LaVO_4$ can transform into tetragonal scheelite-type ($I4_1/a$) or even monoclinic fergussonite-type (I2/a) structures [11]. These transformations are known to substantially influence properties like dielectric behaviour, band structure, and electrical conductivity.

1.2.1 Monazite-Type Structure ($P2_1/n$)

The monazite structure consists of twisted VO_4 tetrahedra and nine-fold coordinated La^{3+} cations, resulting in LaO_9 polyhedra [12]. The V-O bond lengths are unequal, causing significant local distortion and decreased symmetry. This structure is commonly stabilised in un-doped $LaVO_4$, characterised by anisotropic lattice vibrations and increased unit cell volume. Because of its structural flexibility, it can easily absorb point defects, oxygen vacancies, and aliovalent dopants, making it ideal for adjusting dielectric and transport characteristics. Because of the poor crystal symmetry, vibrational modes in the monazite structure detected via Raman spectroscopy are well-separated and intense, making them suitable for phonon engineering. However, poor symmetry might result in intermediate dielectric constants and larger dielectric losses when compared to higher symmetry phases.

1.2.2 Scheelite-Type Structure ($I4_1/a$)

The scheelite structure consists of LaO_8 dodecahedra and VO_4 or NbO_4 tetrahedra arranged in a more symmetric and compact lattice [13]. This structure is generally more stable for $LaNbO_4$ and appears in Nb-rich $LaV_{1-x}Nb_xO_4$ compositions. With Nb^{5+} substitution, the increased B-site ionic radius introduces internal strain—referred to as chemical pressure—that destabilizes the monazite phase and stabilizes the scheelite lattice. Scheelite-type phases demonstrate improved dielectric properties due to their structural rigidity, reduced grain boundary defects, and enhanced polarizability. The VO_4/NbO_4 tetrahedra in scheelite structures are more regular, which contributes to a more uniform distribution of electronic charge, thereby influencing both the real and imaginary components of permittivity.

1.2.3 Fergusonite-Type Structure (I2/a)

Fergusonite structure is monoclinic derivative of scheelite phase and is generally stabilized at higher doping levels or elevated synthesis temperatures [14]. It represents a slightly distorted form of the scheelite structure with elongated unit cells and further reduced symmetry. The transformation from scheelite to fergusonite is often accompanied by additional local distortions and strain, which enhance dielectric relaxation and charge carrier mobility. This phase is particularly useful for functional ceramics where a balance between symmetry and defect density is desired. It is also associated with increased oxygen vacancy concentration, which is favourable for conduction mechanisms in high-temperature dielectric and fuel cell applications.

1.2.4 Factors Affecting Phase Transitions

Several key factors determine the phase stability and structural transformation in $LaV_{1-x}Nb_xO_4$ systems:

- Chemical Doping: Introduction of Nb^{5+} increases the ionic radius at the B-site (V^{5+} ~0.36 Å → Nb^{5+} ~0.48 Å), thereby creating lattice strain that drives the phase change [14].
- Thermal Treatment: Higher calcination and sintering temperatures assist in overcoming kinetic barriers and help in transforming lower symmetry monazite structures to scheelite or fergusonite phases.

- Synthesis Method: Wet chemical methods like sol-gel and hydrothermal synthesis can stabilize metastable phases at lower temperatures, while solid-state reactions favour thermodynamically stable structures.
- Crystallite Size: Smaller crystallite sizes have lower surface energy because of which they can stabilizes higher energy phase as described by the Gibbs–Thomson effect [15].

An illustrative diagram showing relative stability with doping/temperature for different type of structures is shown in Figure 1.1.

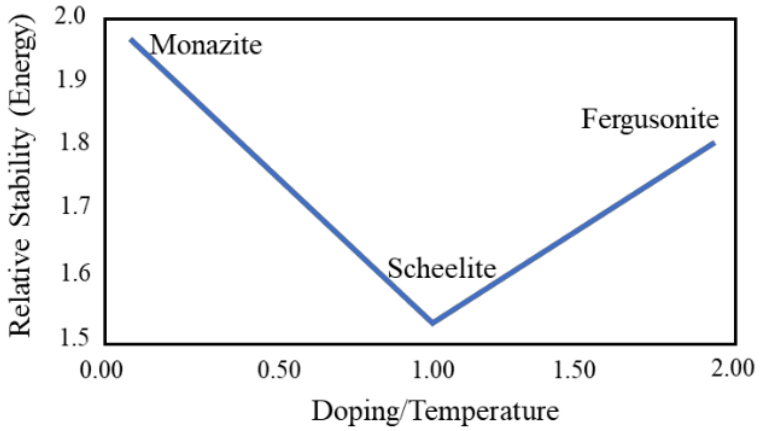


Fig. 1.1: Phase transition showing relative stability in terms of energy with doping/temperature.

1.2.5 Impact on Material Properties

Every structural variant has different characteristics which they impart to the material. For instance:

- Fergusonite: They have higher ionic conductivity and potential which are used in impedance-based capacitors and sensors.
- Scheelite: They have higher dielectric constant values, more frequency stability, and better strength.
- Monazite: They can be tuned using defect chemistry, and have moderate dielectric constant values. They are having high capacity for the incorporation of dopants.

Further, these transitions can be used to alter vibrational spectra, changing the bandgap and microstructure development. These study helps in finding new materials in regard of energy storage applications and optoelectronics.

1.3 Electronic Structure and Bonding Analysis

Electronic structure and bonding properties of $LaVO_4$ and its Nb-doped derivatives considerably impact their optical, dielectric, and electrical properties [16]. These characteristics are determined by the distribution and interaction of valence and conduction bands, which principally include O-2p, V-3d, and Nb-4d orbitals. Substituting vanadium with niobium in the $LaV_{1-x}Nb_xO_4$ lattice changes the band structure, introduces localised states, and transforms the chemical bonding environment, allowing for certain functions [7].

1.3.1 Band Structure and Density of States (DOS)

In pure $LaVO_4$, electronic band structure exhibits wide bandgap semiconductor behaviour, ranging from 3.5 to 4.2 eV depending on the structural phase. The valence band is dominated by oxygen 2p states, whereas conduction band is made up of vanadium 3d orbitals. Doping with Nb^{5+} introduces extra 4d states on the conduction band edge, narrowing the bandgap and increasing electrical conductivity [17]. First-principles density functional theory (DFT) computations show that Nb substitution causes a redistribution of partial density of states (PDOS) [18]. The hybridisation of the Nb-4d and O-2p states decreases the bandgap while increasing charge carrier delocalisation, allowing for improved electrical transport and perhaps boosting photocatalytic activity. The emergence of mid-gap states may potentially facilitate trap-assisted recombination or transition pathways, depending on the structural quality and defect concentration. Additionally, variations in orbital overlap affect the alignment of the conduction band minimum (CBM) and valence band maximum (VBM), resulting in changes in effective mass and carrier mobility [19]. Optimising the electrical conductivity and dielectric loss properties of $LaV_{1-x}Nb_xO_4$ based devices requires consideration of these effects.

1.3.2 Optical Bandgap Tuning and Absorption Characteristics

Optical experiments utilising UV-Vis diffuse reflectance spectroscopy (DRS) [20] reveal significant red shift in absorption edge with increasing Nb concentration. Tauc plot research shows that the type of the bandgap (direct or indirect) can vary depending on the doping amount and structural phase [21]. The observed reduction in bandgap energy increases visible light absorption, which is advantageous for photocatalytic degradation of organic contaminants and light-activated sensor applications. Photoluminescence (PL) tests show that Nb doping reduces the recombination rates of photo excited charge carriers [22]. This suppression is due to increased charge delocalisation and improved electronic coupling between the Nb-O and V-O sub lattices. As a result, doped samples exhibit higher photocatalytic activity and better charge transport capabilities when illuminated. Figure 1.2 shows the change in bandgap of $LaVO_4$ when doped with Nb.

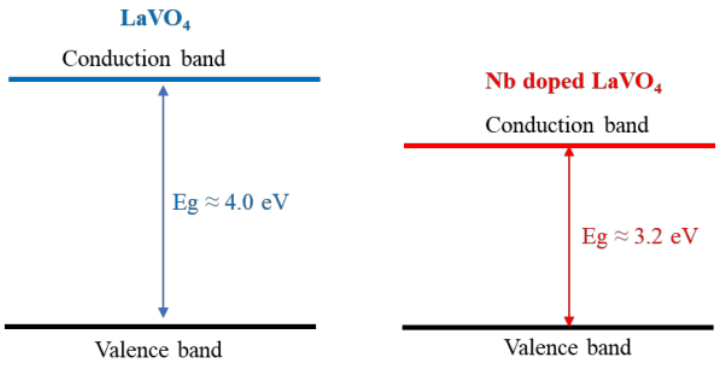


Fig. 1.2: Illustrative figure showing effect of Nb doping on Band gap of $LaVO_4$.

1.3.3 Bonding Environment and XPS Analysis

X-ray photoelectron spectroscopy (XPS) investigations offer information about local bonding arrangement. The binding energy variations in V 2p, Nb 3d, and O 1s peaks caused by Nb doping indicate changes in electron density distribution and bonding strength [23]. Bond valence sum (BVS) computations show that Nb-O contacts are stronger and more covalent than V-O interactions, which has an influence on lattice stability and vibration dynamics. Furthermore, Nb-O bonds are shorter and stiffer than V-O bonds, resulting in higher lattice stiffness. This effect is frequently associated with

reduced phonon scattering, which leads to lower dielectric losses. Increased covalency also affects electrical polarizability, which is an important characteristic in dielectric response.

1.3.4 Defects and Oxygen Vacancies

Nb substitution is isovalent (Nb^{5+} for V^{5+}), although size variations and local distortion can cause oxygen vacancies and defect states. These vacancies play an important function in increasing electrical conductivity through polaron hopping processes and contributing to space charge polarisation in dielectric response [24]. Electron paramagnetic resonance (EPR) [25] and thermogravimetric tests have confirmed the occurrence of such flaws in Nb-rich compositions. Additionally, the formation of Frenkel-type and Schottky-type defects becomes energetically favourable in Nb-doped lattices. These defects influence the activation energy for conduction and the frequency-dependent dielectric relaxation behaviour. The increased defect density also aids in interfacial polarization at grain boundaries, enhancing the Maxwell–Wagner-type dielectric dispersion.

1.3.5 Relationship with Functional Properties

- Dielectric Behaviour: The enhanced polarizability due to Nb–O bonding increases the relative permittivity and modifies dielectric dispersion [26]. The presence of defects and grain boundary effects further contribute to high dielectric constant and frequency-dependent behaviour.
- Photocatalysis: Narrower bandgap, enhanced visible light absorption, and improved charge separation improve visible-light-driven photocatalytic activity.
- Impedance and Conductivity: Defect-induced hopping, reduced bandgap, and Nb-related delocalization effects result in improved AC conductivity, better impedance response, and lower activation energy for carrier motion [27].
- Thermal and Optical Stability: Enhanced bonding stiffness and charge redistribution lead to improved thermal and optical resilience in high-temperature applications.

1.4 Chemical Pressure and Structural Distortion

Chemical pressure is created when we replace an ion with different ionic radii but same oxidation state inside a crystal lattice. It is a type of internal tension within the lattice. We can compare it with hydraulic pressure the only difference rises is that it is not produced physically instead it is produced chemically [27]. In case of $LaV_{1-x}Nb_xO_4$ this pressure comes into play when V^{5+} ions having an ionic-radii of nearly 0.36 Å are replaced by Nb^{5+} ions of bigger radii which is nearly equal to 0.48 Å. Due to this replacement the host lattice starts to expand and get deformed which in turn affects everything inside the unit cell starting from its volume to the bonding properties that results in change in the functional behaviour of material.

The effect of this stress can be seen in both long range as well as short range structural characteristics. The main effect of this can be seen in the form of disrupted symmetry, change in crystallographic location, which leads to the generation of either higher symmetry or deformed polymorphs. The transformation in the crystal field, defect landscape and the bonding environment can be seen with the gradual change from monazite ($P2_1/n$) to scheelite ($I4_1/a$) to fergusonite ($I2/a$) phases [28].

1.4.1 Origin and Mechanism of Chemical Pressure

The size mismatch between the dopant and the host ions is the only force responsible for the chemical pressure inside a lattice. When larger Nb^{5+} ions occupy sites originally held by V^{5+}, the tetrahedral coordination around B-site cations undergoes stress-induced deformation. Bond lengths elongate unevenly, and O–V–O or O–Nb–O bond angles deviate significantly from their ideal values, leading to angular and positional disorder. This internal strain builds up across the crystal, particularly in compositions with intermediate doping levels ($x \approx 0.2–0.6$), where phase coexistence is often observed. Rietveld refinement studies show systematic increases in lattice parameters and unit cell volumes with rising Nb content, while bond valence calculations confirm under- and over-coordination phenomena in selected regions of the lattice. Chemical pressure also modifies the crystal field splitting experienced by transition metal ions, altering electronic configurations and hybridization schemes. This affects not just the geometry of coordination polyhedral but also their reactivity and electronic contribution to the conduction and valence bands.

1.4.2 Structural Distortion and Bonding Consequences

The lattice distortion induced by chemical pressure is most evident in polyhedral deformation. VO_4 and NbO_4 tetrahedra show increased angular deviation, resulting in greater bond angle variance. Raman spectroscopy reveals broadening of the symmetric stretching modes (ν_1) and increased splitting of bending modes (ν_2, ν_4), which indicates lowered site symmetry. The asymmetric expansion also disrupts the orbital overlap between metal and oxygen atoms. This alters the covalency of M–O bonds and redistributes electron density across the lattice [29]. DFT studies suggest emergence of localized states in band structure due to lattice strain, which can impact electrical conductivity and defect migration. Moreover, the distortion affects the phonon transport and dielectric relaxation dynamics. A larger spread in vibrational frequencies contributes to more extensive dielectric dispersion, as seen in impedance spectroscopy. This provides opportunities for tailoring the material for broadband dielectric applications.

1.4.3 Influence on Microstructure and Grain Boundaries

Beyond the atomic scale, chemical pressure impacts the microstructure and mesoscale organization of the material:

- Crystallite Size and Morphology: The lattice strain suppresses grain growth during sintering by increasing grain boundary energy. SEM and TEM studies often show reduced crystallite sizes and irregular grain morphology in highly doped samples.
- Micro strain and Lattice Disorder: Peak broadening in X-ray diffraction patterns, evaluated using Williamson–Hall plots, confirms elevated micro strain and lattice curvature effects.
- Grain Boundary Resistivity: The changes in boundary chemistry and structure influence charge transport pathways, enhancing grain boundary resistance and contributing to complex impedance arcs in Nyquist plots.

Additionally, the accumulation of chemical pressure at grain junctions may promote the formation of intergranular defects, further modulating the electrical and mechanical behaviour of sintered pellets.

1.4.4 Impact on Functional Properties

Chemical pressure-driven structural changes manifest in a variety of property enhancements:

- Dielectric Constant: Increased local polarization due to distorted M–O bonds boosts permittivity values. The breakdown of centrosymmetry increases nonlinearity in dielectric response.
- Bandgap Engineering: The hybridization of Nb-4d states with the conduction band reduces the bandgap by 0.3–0.6 eV in typical samples. This improves light absorption in the visible region.
- Electrical Conductivity: Enhanced small polaron hopping is facilitated by asymmetric lattice potential wells. Activation energies decrease due to better orbital alignment for charge transfer.
- Mechanical Hardness: Chemical pressure stiffens the lattice, improving Young's modulus and making the material more resilient to fracture under mechanical load.
- Thermal Stability: The more compact scheelite and fergusonite phases exhibit lower thermal expansion coefficients, making them suitable for high-temperature capacitor and resonator applications.

1.4.5 Relevance in Material Design

Chemical pressure serves as a cost-effective and scalable method for tuning material behaviour. Unlike external pressure methods requiring specialized apparatus, chemical pressure can be introduced via routine doping in conventional synthesis techniques. This makes it particularly advantageous for:

- Phase Stabilization: Useful in stabilizing high-temperature or metastable phases at room temperature.
- Property Tailoring: Enables co-engineering of structural, electronic, and optical properties simultaneously.
- Device Integration: Allows design of custom materials for capacitors, thermistors, gas sensors, and photocatalysts.

In essence, chemical pressure is a silent but powerful tool in the material designer's toolkit influencing everything from lattice symmetry to device performance. In conclusion, the substitutional introduction of Nb^{5+} in $LaVO_4$ not only modifies the crystallographic phase but also alters bonding, microstructure, and macroscopic physical behaviour. The controlled use of chemical pressure in $LaV_{1-x}Nb_xO_4$ offers a versatile strategy for optimizing performance in multifunctional ceramic systems, bridging the gap between fundamental solid-state science and real-world applications.

1.5 Applications of $LaVO_4$, $LaNbO_4$, and their Composites

1.5.1 Photocatalysis and Environmental Remediation

$LaVO_4$ has emerged as a potent visible-light-driven photocatalyst due to its suitable bandgap (~2.9–3.2 eV), robust VO_4 tetrahedral structure, and chemical stability [8]. The incorporation of Nb^{5+} leads to improved charge separation efficiency by modifying the band alignment and suppressing electron–hole recombination. The resulting $LaV_{1-x}Nb_xO_4$ systems have shown enhanced photocatalytic degradation of methylene blue, rhodamine B, and tetracycline under visible light irradiation. The mechanism involves the excitation of electrons from O-2p to V-3d/Nb-4d levels, generating reactive oxygen species (•OH, $•O_2^-$) that degrade pollutants. Nb incorporation also improves surface area and defect site formation, crucial for catalytic performance.

1.5.2 High-k Dielectrics and Capacitors

$LaNbO_4$ is known for its high dielectric constant (>60), low dielectric loss, and thermal stability, making it suitable for microelectronic capacitors [30]. The Nb^{5+} substitution in $LaVO_4$ tunes the local dipole polarization, facilitating enhanced permittivity and stable tan δ across broad temperature and frequency ranges. The dielectric behaviour stems from both intrinsic lattice contributions and extrinsic Maxwell–Wagner-type polarization [31] at grain boundaries. $LaV_{1-x}Nb_xO_4$ compositions in the scheelite or mixed-phase regime exhibit optimal dielectric performance with tan δ values between 0.05–0.15 and high breakdown voltage characteristics, making them suitable for embedded capacitors and high-energy density devices.

1.5.3 Solid Oxide Fuel Cells (SOFCs)

$LaNbO_4$ based ceramics are notable proton conductors used as electrolyte materials in intermediate-temperature SOFCs [32]. Nb^{5+} doping in $LaVO_4$ increases the oxygen vacancy concentration and promotes proton transport by modifying the lattice strain and bond angles. In $LaV_{1-x}Nb_xO_4$, the mixed phase region supports both electronic and protonic conduction, useful for dual-functional electrodes. Studies have shown proton conductivity reaching 10^{-3} S/cm at 700 °C in $LaNbO_4$ rich samples. These materials are chemically stable in hydrogen environments and resistant to CO_2 poisoning, an advantage over traditional yttria-stabilized zirconia (YSZ).

1.5.4 Sensors and Thermistors

The semiconducting nature of $LaVO_4$ and $LaNbO_4$ allows their use in temperature and gas sensors. Nb doping modifies the band structure, increases activation energy for conduction, and enhances impedance contrast. $LaV_{1-x}Nb_xO_4$ samples with mixed monazite–scheelite or scheelite–fergusonite phases exhibit strong dielectric dispersion and relaxation peaks, which are highly sensitive to temperature, humidity, and gas exposure. These materials can be integrated into negative temperature coefficient (NTC) thermistors and capacitive gas sensors, where impedance changes serve as a detection metric. Moreover, their ceramic nature ensures thermal durability and long-term stability.

1.5.5 Laser Host and Phosphor Materials

Lanthanum orthovanadates doped with rare earth ions (e.g., Nd^{3+}, Eu^{3+}, Yb^{3+}) have been widely explored as laser hosts and phosphors due to their stable lattice and strong absorption/emission in the visible and near-IR regions [33]. Nb substitution offers phase stability and improves crystal transparency, which is crucial for optical gain media. $LaV_{1-x}Nb_xO_4$ can act as a host matrix for up conversion phosphors and near-UV excitation in white LEDs. The scheelite-type structure facilitates efficient energy transfer from VO_4/NbO_4 groups to activator ions, enabling high luminescence yield and colour purity. These materials show potential in solid-state lasers, bioimaging, and X-ray scintillators as shown in Figure 1.3.

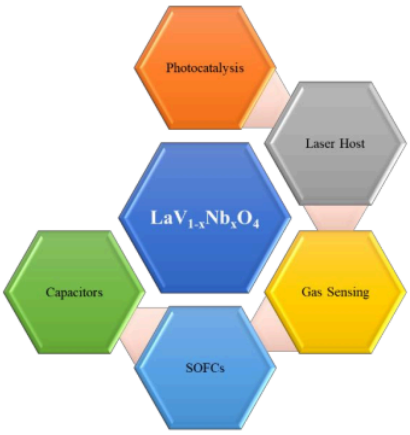


Fig. 1.3: Block diagram showing different applications of $LaVO_4$.

1.6 Conduction Mechanisms in $LaV_{1-x}Nb_xO_4$ Ceramics

Understanding the conduction mechanisms in $LaV_{1-x}Nb_xO_4$ ceramics is vital for tailoring their electrical and dielectric properties, which are essential for their implementation in advanced applications like high-frequency capacitors, oxygen sensors, thermistors, and electrochemical devices. The overall conduction in these materials arises from a combination of bulk lattice phenomena, defect chemistry, local distortion, and interfacial effects. As Nb^{5+} is introduced into the $LaVO_4$ framework, it not only modifies the local bonding environment but also alters the energy landscape for charge carrier movement by creating strain, oxygen vacancies, and mixed-valence states.

1.6.1 Small Polaron Hopping (SPH)

In undoped $LaVO_4$, electronic conduction predominantly occurs through hopping of electrons between adjacent V^{4+} and V^{5+} sites a process termed small polaron hopping. This mechanism is particularly relevant in transition metal oxides with localized d-electrons and strong electron-lattice coupling. The incorporation of Nb^{5+} further distorts the lattice, expanding the tetrahedral sites and modifying the Coulombic landscape, thereby influencing the activation barrier for carrier hopping. The temperature-dependent DC conductivity generally obeys the Arrhenius relation [34]:

$$\sigma = \sigma_0 \exp(-E_a/kT) \quad (1.1)$$

The lowering of E_a with Nb content suggests that lattice distortion and increased overlap of Nb 4d orbitals with oxygen orbitals enhance the probability of carrier hopping. SPH also contributes to increased polaron mobility, which is especially significant at elevated temperatures (above 400 °C), where thermal energy assists in overcoming potential barriers between localized sites.

1.6.2 Role of Oxygen Vacancies, Mixed Valency, and Defect Chemistry

Despite being isovalent, the larger ionic radius of Nb^{5+} disrupts the local symmetry around the B-site (V/Nb), promoting the formation of intrinsic defects such as oxygen vacancies and interstitials. These vacancies act as shallow donors, contributing to n-type conductivity. The generation of such defects follows the Kröger–Vink notation [35]:

$$O + 2e^- \rightleftharpoons O^{2-}$$

Oxygen vacancies also act as trapping centres for electrons or holes, influencing dielectric relaxation. Their concentration increases with Nb doping due to the local strain and thermodynamic tendency to relieve the mismatch between ionic radii. Mixed valency, often evidenced via XPS, shows the presence of V^{4+}/V^{5+} or Nb^{4+}/Nb^{5+} pairs, which facilitate intervalence charge transfer.

Defect clusters may form around Nb sites, and these complex configurations modify the electrostatic potential and charge neutrality in the lattice. Their interaction with mobile ions and electrons strongly affects long-range conduction and polarization behaviour.

1.6.3 AC Conductivity and Jonscher's Power Law

In alternating current (AC) settings, $LaV_{1-x}Nb_xO_4$ exhibits dispersive behaviour consistent with Jonscher's universal power law [36]:

$$\sigma(\omega) = \sigma_{dc} + A\omega^n \quad (1.2)$$

The exponent 'n' is temperature and doping level dependent, often falling between 0.6 and 0.9. It indicates the degree of interaction between mobile ions and lattice vibrations. The reduction in 'n' with rising temperature shows that the correlated barrier hopping

(CBH) process is dominant, in which carriers hop over potential barriers that are dynamically modified by local defects.

The high-frequency dispersion zone is due to localised dipole reorientation and charge carrier hopping over small distances, whereas the low-frequency plateau indicates long-range charge transport. This behaviour is consistent with disordered ionic systems and lends credence to the theory of mixed conduction incorporating both electronic and defect-mediated routes.

1.6.4 Grain and Grain Boundary Contributions

Electrical transport in polycrystalline ceramics, such as $LaV_{1-x}Nb_xO_4$, is influenced by both bulk and interfacial processes. Impedance spectroscopy frequently exhibits twin semi-circular arcs in Nyquist graphs.

- The high-frequency arc corresponds to grain (bulk) conduction.
- The low-frequency arc arises from grain boundary resistance and interfacial polarization.

As Nb concentration increases, bulk resistance (R_g) reduces due to increased carrier mobility and orbital overlap, however grain boundary resistance (R_{gb}) may stay high or rise due to dopant segregation and defect entrapment at the borders. Equivalent circuits often include parts such as $R_g \| C_g$ and $R_{gb} \| C_{gb}$, which can be configured in series or parallel.

Grain limits may operate as impediments to carrier movement, but they can also contribute to space charge polarisation, particularly when ornamented with charged defects or impurities. The engineering of grain size, distribution, and boundary chemistry thus plays a crucial role in determining the net conduction behaviour.

1.6.5 Temperature Dependent Conduction and Activation Energies

Activation energy (E_a) values derived from DC conductivity and relaxation time plots decrease from ~1.2 eV in undoped $LaVO_4$ to ~0.6 eV in Nb-rich samples. This reduction reflects the increasing ease of carrier movement due to dopant-induced structural changes. The activation energy also provides insights into the dominant mechanism:

- High E_a (~1.0–1.2 eV): Dominant ionic conduction, typical of undoped systems.
- Intermediate E_a (~0.7–0.9 eV): Mixed ionic and electronic conduction.
- Low E_a (<0.6 eV): Predominantly electronic conduction with delocalized carriers.

The transition in conduction type with doping and temperature supports the tunability of $LaV_{1-x}Nb_xO_4$ for application-specific requirements. Arrhenius plots for impedance and modulus peaks are commonly used to extract E_a values corresponding to bulk and grain boundary processes.

1.6.6 Dielectric Loss, Relaxation, and Interfacial Polarization

High-temperature dielectric spectroscopy reveals multiple relaxation processes that are influenced by Nb content. The dielectric loss tangent (tan δ) peaks shift to higher frequencies with increasing temperature, suggesting thermally activated dipole relaxation. Oxygen vacancies and local distortions serve as polar centres, contributing to Maxwell–Wagner-type polarization. Impedance and electric modulus analysis help isolate the relaxation associated with grains, grain boundaries, and electrode effects. The distribution of relaxation times becomes broader with doping, as evidenced by non-Debye behaviour and asymmetric peaks in the modulus spectra.

1.6.7 Relevance to Practical Applications

The rich conduction landscape in $LaV_{1-x}Nb_xO_4$ ceramics enables them to serve in a variety of functional applications:

- Thermistors: Tunable resistance with temperature makes them viable for temperature sensing.
- Solid-State Electrolytes: Ionic conduction at elevated temperatures supports their use in fuel cells and oxygen pumps.
- Resistive Switching Devices: Defect-driven conduction mechanisms allow for memory device applications.
- High-k Dielectrics: Stable dielectric properties and frequency dispersion make them suitable for capacitors and RF filters.

1.7 Computational Insights and DFT Studies

Computational modelling, based on density functional theory (DFT), is a transformational way to understand, forecast, and optimise the characteristics of complex oxide ceramics such as $LaV_{1-x}Nb_xO_4$. These simulations do more than just validate experimental results; they also assist comprehend the underlying atomic-scale processes, identify possible novel phases, and give prediction insights that are critical for the rational design of functional materials. In $LaV_{1-x}Nb_xO_4$ systems, where substitutional doping and defect chemistry play a prominent role, DFT provides unmatched insight into how Nb inclusion affects crystal symmetry, modifies electronic structure, stabilises certain phases, and influences charge transport.

1.7.1 Band Structure and Density of States (DOS)

Pure $LaVO_4$ has a broad bandgap semiconductor behaviour, with a typical gap of 3.5-4.2 eV, depending on phase. DFT investigations show that valence band maximum (VBM) is mostly made up of O 2p states, whereas conduction band minimum (CBM) is made up of V 3d orbitals. The insertion of Nb causes extra 4d states at the CBM, thus reducing the bandgap. Nb-doped $LaVO_4$ exhibits higher visible light absorption and photocatalytic activity, owing to these key modifications.

To better represent electronic states, DFT computations with generalised gradient approximation (GGA), hybrid functionals such as HSE06, and DFT+U techniques are commonly utilised. DFT+U helps correct for the underestimation of bandgaps in strongly correlated systems. The hybridization between Nb 4d and O 2p orbitals also modifies the density of states (DOS), introducing new intermediate bands that facilitate charge carrier transitions, which is crucial for tailoring materials for optoelectronic applications.

1.7.2 Structural Relaxation and Phase Stability

Structural relaxation calculations performed on $LaV_{1-x}Nb_xO_4$ supercells reveal lattice expansion and increased distortion around the Nb substitution sites. The total energy calculations suggest that the substitution of Nb stabilizes the scheelite or fergusonite phases over the monazite phase, in alignment with experimental phase diagrams. These

simulations show that even low concentrations of Nb doping can result in a structural phase transition driven by internal chemical pressure.

Formation energy analysis and stress-strain modelling indicate that Nb dopants create local stress fields, influencing grain orientation and symmetry breaking. Phonon stability studies and total energy vs volume plots further establish the preferred structural phase under varying synthesis conditions. Computational exploration of different Nb concentrations allows prediction of critical doping thresholds necessary for stabilizing specific polymorphs.

1.7.3 Defect Formation Energies and Oxygen Vacancy Behaviour

DFT is crucial for evaluating defect chemistry, especially the formation and energetics of oxygen vacancies, which are central to both ionic and electronic conduction. In $LaV_{1-x}Nb_xO_4$, the presence of Nb^{5+} alters the local chemical environment, making oxygen vacancy formation more favourable. Calculated formation energies for defects decrease with Nb content, supporting the experimentally observed rise in conductivity and dielectric relaxation.

Advanced DFT approaches such as Bader charge analysis, electron localisation functions (ELF), and charge density difference maps shed light on the charge distribution near defects. These investigations show that oxygen vacancies cluster near Nb-rich locations, causing asymmetric electron clouds that facilitate polaron production and increase conductivity. Such simulations also show that defect clustering is energetically advantageous at moderate doping levels, which influences long-range charge transport.

1.7.4 Dielectric and Phonon Properties

Phonon calculations employing density functional perturbation theory (DFPT) or finite displacement techniques provide insight into the vibrational modes that impact dielectric behaviour. In $LaV_{1-x}Nb_xO_4$, Nb doping alters phonon dispersion relations, particularly the low-frequency modes related to oxygen vibrations. These modifications are consistent with red-shifting and broadening of Raman modes observed experimentally.

The calculated static and dynamic dielectric tensors help distinguish between electronic and ionic contributions to permittivity. Simulations indicate that dielectric constant

increases with Nb concentration due to enhanced ionic displacement and polarizability. Furthermore, phonon lifetimes and group velocities derived from these calculations offer insights into thermal transport and phonon scattering essential for understanding dielectric losses at high frequency.

1.7.5 Charge Transport and Carrier Mobility

Electron and hole effective masses computed via band curvature analysis provide a quantitative measure of carrier mobility. In $LaV_{1-x}Nb_xO_4$, Nb doping reduces the electron effective mass due to the dispersion introduced by the Nb 4d states, which results in better electronic conduction. Mobility predictions using the Boltz Trap code, based on the Boltzmann transport equation, allow for estimating See beck coefficients, electrical conductivity, and power factor for thermoelectric applications. Charge density distributions also suggest that carriers in Nb-rich compositions are more delocalized, improving transport across grain boundaries. Calculated charge carrier lifetimes and scattering rates offer a microscopic understanding of the conduction mechanisms from band transport in scheelite phases to hopping-type behaviour in distorted or defect-rich monazite lattices.

1.7.6 Electronic Polarization and Ferroelectric Potential

Emerging studies also explore the possibility of intrinsic ferroelectricity in distorted $LaV_{1-x}Nb_xO_4$ structures due to off-centering of cations and asymmetric bonding. Berry phase calculations of polarization vectors, coupled with potential energy surface mapping, provide evidence for switchable polarization in Nb-substituted polymorphs under certain conditions. This introduces the possibility of multi functionality combining dielectric, semiconducting, and ferroelectric behaviour in a single phase.

1.7.7 Limitations and Future Outlook

Despite its power, standard DFT has limitations in handling strong electron correlation and highly localized defect states. Therefore, hybrid functional approaches (like HSE06), GW approximations, and time-dependent DFT (TD-DFT) are being increasingly adopted for better accuracy. Moreover, machine learning (ML) models trained on DFT data are

now being used for high-throughput screening of doping strategies, defect tolerance, and stability predictions.

Recent advances in computational infrastructure allow for large-scale modelling of supercells with thousands of atoms, enabling simulation of real grain boundaries, surface terminations, and phase interfaces. These methods will be essential in bridging the gap between idealized models and real ceramic microstructures.

DFT studies have provided deep insights into the complex interplay between structure, defects, and functionality in $LaV_{1-x}Nb_xO_4$ ceramics. From bandgap engineering and defect energetics to phase stability and charge transport, computational tools have become indispensable in predicting and validating multifunctional behaviour. As computational capabilities expand and integrate with AI and data science, the design of next-generation $LaVO_4$ based materials will become increasingly predictive and targeted for specific high-performance applications.

1.8 Comparison with Other Systems

A comprehensive analysis of $LaV_{1-x}Nb_xO_4$ ceramics gains further depth and meaning when juxtaposed with analogous systems in the broader family of functional oxides. This comparative approach not only highlights $LaV_{1-x}Nb_xO_4$'s strengths but also delineates its weaknesses and areas of potential improvement. Through comparisons with rare-earth orthovanadates, niobates, scheelites, monazites, perovskites, pyrochlores, and even hybrid oxide systems, one can establish a nuanced understanding of where $LaV_{1-x}Nb_xO_4$ stands in terms of structural adaptability, dielectric performance, electronic conduction, optical absorption, and multi functionality.

1.8.1 Comparison with Other Rare-Earth Orthovanadates ($LnVO_4$)

Rare-earth orthovanadates, yttrium denoted by lanthanides, are a structurally and electrically rich family. These compounds are having zircon-type (tetragonal) or monazite-type (monoclinic) structures dependent on the ionic radius of the Ln^{3+} cation. The zircon-type is preferred for smaller lanthanides like Y^{3+}, Lu^{3+} and Gd^{3+} whereas the monazite-type structure is stabilised by ions which are bigger like Ce^{3+}, La^{3+}, and Nd^{3+}.

- $GdVO_4$ and YVO_4: Structure of these materials is Zircon-type, they are widely used in photonic devices because of high optical transparency, mainly in UV-visible regions. However, they are having relatively poor dielectric properties [37].
- $CeVO_4$: Exhibits both Ce^{3+} and Ce^{4+} valence states, making it redox-active and suitable for catalytic oxidation. However, its limited thermal stability limits its use in high-temperature environments [38].
- $NdVO_4$ and $SmVO_4$: Known for sharp luminescence lines, they are best suited for laser applications but are not optimized for electrical conduction or dielectric uses [39].

In contrast, $LaV_{1-x}Nb_xO_4$ offers:

- Tunable phase transitions between monazite, scheelite, and fergusonite types
- Enhanced dielectric constant and reduced dielectric loss via Nb doping
- Defect-mediated conductivity and visible light bandgap engineering

Moreover, the combination of La's structural flexibility and Nb's chemical pressure effect makes $LaV_{1-x}Nb_xO_4$ a more versatile candidate for multifunctional applications compared to other $LnVO_4$ analogues.

1.8.2 Comparison with $LaNbO_4$ and Other Niobates

$LaNbO_4$ is structurally similar to the Nb-rich end of $LaV_{1-x}Nb_xO_4$ and crystallizes in a stable scheelite phase. It has been explored extensively for high-temperature dielectric applications due to its large permittivity and low dielectric loss. However, it suffers from limited optical tunability and higher synthesis temperatures.

Other niobates such as:

- $BaNb_2O_6$ and $SrNb_2O_6$: Exhibit nonlinear optical properties but are structurally rigid and sensitive to atmosphere.
- $KNbO_3$: A perovskite-type ferroelectric material with excellent piezoelectric properties but complex phase transitions [40].

$LaV_{1-x}Nb_xO_4$ provides:

- Intermediate structural flexibility

- Enhanced oxygen vacancy formation for improved conductivity
- Controlled bandgap engineering for photocatalysis

Thus, while $LaNbO_4$ provides excellent dielectric performance, $LaV_{1-x}Nb_xO_4$ goes beyond, combining electrical, optical, and structural tunability in one system.

1.8.3 ABO_4 Type Scheelites and Monazites ($BiVO_4$, $CaWO_4$, etc.)

Other ABO_4 type compounds with scheelite or monazite structures are prominent in scintillators, photocatalysts, and dielectric materials.

- $BiVO_4$: A benchmark visible-light photocatalyst with a narrow bandgap (~2.4 eV). However, it suffers from fast charge recombination and poor long-term stability [41].
- $CaWO_4$ and $SrWO_4$: Popular in medical imaging and scintillator applications. High structural stability but poor dielectric response.
- $YNbO_4$ and YVO_4: Show good mechanical properties but limited compositional flexibility.

$LaV_{1-x}Nb_xO_4$ integrates:

- Superior tunability in structure and bandgap
- Defect-induced conduction and high dielectric response
- High thermal and phase stability

This positions it as a more adaptable material compared to most monofunctional ABO_4 counterparts.

1.8.4 Comparison with Doped Perovskites and Pyrochlores

Doped perovskites (ABO_3) and pyrochlores ($A_2B_2O_7$) are widely used in electronics due to their superior dielectric, ferroelectric, and magnetic responses.

- $BaTiO_3$: Benchmark ferroelectric material with high dielectric constant, but suffers from aging and environmental instability [42].

- $SrTiO_3$: Known for quantum paraelectric behaviour, limited by high leakage currents.
- $Gd_2Ti_2O_7$, $Nd_2Zr_2O_7$: Pyrochlores with good structural and thermal stability but low permittivity.

Compared to these:

- $LaV_{1-x}Nb_xO_4$ combines moderate dielectric constant with high tunability
- Shows better chemical stability and thermal compatibility
- Provides defect-controlled conductivity without loss of structural integrity

This makes $LaV_{1-x}Nb_xO_4$ an excellent compromise between performance and reliability.

1.8.5 Comparison with Hybrid Systems and Multicomponent Oxides

Recent material developments focus on hybrid perovskites, composite oxides, and heterostructures to integrate multiple functionalities:

- $BiFeO_3$–$BaTiO_3$ composites: Combine ferroelectric and magnetic properties but have complex phase diagrams [43].
- TiO_2–$BiVO_4$ heterostructures: Enhanced photocatalytic performance but poor long-term stability [44].
- Zr-doped $Ba_{0.5}Sr_{0.5}TiO_3$: High-k dielectric behaviour but sensitive to processing parameters [45].

$LaV_{1-x}Nb_xO_4$ stands out for:

- Maintaining single-phase integrity despite doping
- Simultaneous control over dielectric, optical, and electronic behaviour
- Scalable synthesis and compatibility with industrial sintering techniques

1.8.6 Application-Specific Comparisons

- In Photocatalysis: $BiVO_4$ and TiO_2 based materials are efficient but unstable. $LaV_{1-x}Nb_xO_4$ offers visible light activity with improved stability.
- In Dielectric Capacitors: Perovskites have higher permittivity, but $LaV_{1-x}Nb_xO_4$ offers better frequency response and thermal endurance.

- In Gas Sensors: Transition metal oxides like SnO_2 are sensitive but lack selectivity. Nb-doped $LaVO_4$ can provide tuneable selectivity with better thermal resistance.
- In Solid Oxide Fuel Cells (SOFCs): Doped ceria is commonly used but expensive. $LaV_{1-x}Nb_xO_4$ offers a cost-effective alternative with mixed conduction.

$LaV_{1-x}Nb_xO_4$ ceramics exhibit a rare balance of structural flexibility, electronic tunability, and thermal/chemical stability. When compared across structural types and functional families, they emerge as strong contenders for multifunctional applications that demand simultaneous performance in optical, electrical, and mechanical domains. Their ability to adapt via compositional tuning, maintain phase purity under doping, and operate under harsh environments places them among the most promising ABO_4 type ceramic systems.

Future comparative studies involving experimental benchmarking and computational screening could further reveal synergistic doping strategies and structural modifications, paving the way for next-generation materials based on the $LaV_{1-x}Nb_xO_4$ compositional space.

1.9 Objectives of the Present Work

1. Synthesize $LaV_{1-x}Nb_xO_4$ ($0 \leq x \leq 1$) via the solid-state reaction method
2. Analyse phase evolution and crystal structure using XRD and Rietveld refinement
3. Study vibrational dynamics through Raman spectroscopy
4. Explore microstructure using SEM and HR-TEM
5. Investigate bonding environments using XPS
6. Evaluate dielectric constant, loss tangent, and complex impedance as functions of temperature and frequency
7. Correlate phase composition with conduction mechanisms and relaxation behaviour

1.10 Thesis Organization

The present thesis is structured into six comprehensive chapters, each designed to systematically build the narrative from foundational knowledge to the original contributions of this research. A brief overview of the content and purpose of each chapter is given below:

- **Chapter 1**: Introduction and Literature Review
- **Chapter 2**: Synthesis and Characterization
- **Chapter 3**: Published Paper on Vibrational, Structural and Electronic Properties of Nb substituted orthovanadates $LaV_{1-x}Nb_xO_4$
- **Chapter 4**: Published Paper on Dielectric Behaviour and Impedance Spectroscopy of Nb Substituted Lanthanum Orthovanadates
- **Chapter 5**: Accepted paper on "Physical and Dielectric Properties of Polycrystalline $LaV_{0.5}Nb_{0.5}O_4$"
- **Chapter 6**: Conclusion, Future Scope and Social Impact

Chapter 2

Synthesis and Characterization Techniques

2.1 Introduction

The synthesis and characterization of functional oxide materials are foundational to understanding and tailoring their physical and chemical properties for advanced applications. In this chapter, the detailed synthesis strategy and multi-technique characterization of niobium-substituted lanthanum orthovanadate ($LaV_{1-x}Nb_xO_4$) ceramics are presented. The rationale for selecting the $LaV_{1-x}Nb_xO_4$ system is based on the complementary roles of $LaVO_4$ and $LaNbO_4$ in delivering structural stability, electronic flexibility, and dielectric tunability. $LaVO_4$ exists predominantly in the monoclinic monazite structure at ambient conditions, whereas $LaNbO_4$ stabilizes in a monoclinic fergusonite-type structure. The progressive substitution of V^{5+} with Nb^{5+} introduces chemical strain and distortion into the lattice, resulting in phase transitions and altered bonding environments. Understanding how these atomic-level changes affect macroscopic behaviour requires systematic synthesis followed by comprehensive structural, vibrational, and electronic analysis. The successful implementation of such a study demands a rigorous approach to both material synthesis and characterization. Solid-state reaction synthesis offers excellent reproducibility and is widely accepted for ceramic oxides. Coupled with high-temperature processing, it ensures sufficient diffusion for atomic mixing and proper crystallization.

Subsequently, an extensive set of analytical tools is employed. X-ray diffraction (XRD) provides crystal structure and phase composition, Raman spectroscopy captures lattice dynamics and local distortions, X-ray photoelectron spectroscopy (XPS) reveals oxidation states and chemical environments, and dielectric spectroscopy elucidates frequency and temperature-dependent electrical behaviour. Microscopy tools such as scanning electron microscopy (SEM) and high-resolution transmission electron microscopy (HR-TEM) contribute crucial insights into the morphology and microstructure of the synthesized powders. This chapter describes each of these components in detail, beginning with the reagents and protocols used for synthesis,

followed by the working principles, instrumentation, and application of the various characterization methods adopted in this research.

2.2 Overview of Synthesis Methods for Ceramic Oxides

A wide variety of synthesis techniques are used in the preparation of complex oxide ceramics, each with distinct benefits and limitations. Below is a comprehensive explanation of the most widely employed methods.

2.2.1 Solid-State Reaction Method

The solid-state reaction method involves mixing solid-state precursors (usually oxides, carbonates, or nitrates) in stoichiometric ratios and reacting them at elevated temperatures (typically 800–1500 °C). The high temperature facilitates interdiffusion of ions and formation of the desired crystalline phase [1]. The main steps involve weighing and mixing of precursors in which stoichiometric proportions of precursors are manually or mechanically mixed, often using agate mortar or planetary ball mills then the mixed powders are heated at an intermediate temperature to initiate solid-state diffusion and phase formation. Further the intermediate products are reground to improve homogeneity and subjected to repeated calcination to complete the reaction. Final densification is achieved at higher temperatures to develop grain growth and reduce porosity.

The key advantage of solid-state reaction method is that it is simple, cost-effective, easily scalable for bulk production, and suitable for high-temperature stable phases. Its main disadvantages arises because it requires long processing times, it often results in large, agglomerated particles and homogeneity depends heavily on mixing efficiency. Solid state reaction method is widely used for synthesizing perovskites, garnets, ferrites, and orthovanadates.

2.2.2 Sol-Gel Method

The sol-gel method involves the transformation of a liquid “sol” (a colloidal suspension of particles) into a solid “gel” through hydrolysis and polycondensation reactions of metal alkoxides or salts [2]. The first step in this process is solution preparation in

which metal alkoxides or chlorides are dissolved in alcohol or water. After that hydrolysis and condensation takes place in which water is added under controlled pH to hydrolyze the precursors and form a network of metal-oxygen-metal bonds. The next step includes gelation process in which the sol transforms into a gel with a three-dimensional porous network. Further the gel is dried to remove solvents and then calcined to remove organic residues and form the oxide network.

The key advantage of sol gel method is that it gives excellent control over stoichiometry and homogeneity at the molecular level, yields nanostructured materials with high surface area, and it operates at lower synthesis temperature than solid-state methods. The main disadvantage of sol gel method is that it is sensitive to ambient humidity and pH, also the gelation and aging steps are time consuming and there is residual carbon contamination is possible if not calcined properly. The main application of sol gel process is that it is common for preparing nanophosphors, oxide thin films, catalysts, and high-purity ceramic powders.

2.2.3 Co-precipitation Method

In this wet-chemical route, cations are precipitated simultaneously from solution, typically as hydroxides or carbonates, followed by filtration, drying, and calcination [3]. The process involved in co-precipitation method includes solution preparation in which metal nitrate or chloride solutions are mixed in desired stoichiometry than the solution was precipitated using precipitating agent such as NH_4OH or NaOH is added dropwise to precipitate metal hydroxides. Precipitate is then aged, filtered, and washed to remove ionic impurities. Further the sample was dried and powder is thermally decomposed to yield metal oxides.

The key advantages of co-precipitation method is that fine particle size with uniform distribution is formed with high compositional homogeneity, good yield and reproducibility. This method requires rigorous control of pH, precipitation kinetics which is one of its disadvantages. Also, its washing may be labour-intensive to remove nitrates or chlorides and risk of co-precipitate segregation in multi-cation systems are its other disadvantages. This method is widely used in the preparation of doped ferrites, perovskites, and luminescent materials.

2.2.4 Hydrothermal Method

This technique involves crystal growth from aqueous solutions at high pressure and temperature, typically inside a sealed autoclave. The high-pressure environment enhances solubility and reactivity of precursors [4]. The key steps included in synthesis using hydrothermal method includes solution preparation in which metal precursors are dissolved or suspended in water or basic/acidic media after that the solution is placed in a Teflon-lined stainless-steel autoclave than the solution was heated to 120–250 °C for several hours to days under autogenous pressure after that products are filtered, washed, and dried.

Hydrothermal method produces well-crystallized materials at low temperature, enables growth of exotic morphologies (nanorods, sheets, etc.) and environmentally benign; uses water as solvent. The main disadvantages of hydrothermal method include limited batch size, requires pressure-resistant equipment, and difficulty to scale up. This method is ideal for synthesizing nanostructured oxides, zeolites, and photocatalysts.

2.2.5 Combustion Synthesis

Combustion synthesis is based on exothermic redox reaction between metal nitrates (oxidizers) and fuels like urea, glycine, or citric acid. The reaction propagates through the mixture, yielding oxide products with high porosity [5]. This method includes solution preparation using nitrate salts and fuel are mixed in a precise oxidizer-to-fuel ratio than a viscous gel may be formed prior to ignition, further the gel was heated or ignited using a spark or external source; reaction becomes self-sustaining. The product is usually fluffy, porous oxide ash requiring sintering. The main advantage of Combustion method is processing time. It is extremely fast synthesis (seconds to minutes), no external heating required post-ignition and nanoporous structures ideal for catalysis and sensing are synthesized. Its disadvantages include poor crystallinity unless followed by sintering, high surface area may not be ideal for dielectric applications, and residual carbon or nitrogen is possible. It is mainly used in ferrites, catalysts, magnetic materials, and nanoceramics.

Table 2.1: Comparison of different synthesis methods

Method	Temp (°C)	Size Control	Crystallinity	Complexity	Scalability
Solid-State	1000–1400	Poor	High	Low	High
Sol-Gel	400–800	Excellent	Moderate	High	Low
Co-precipitation	500–900	Good	Moderate	Medium	Medium
Hydrothermal	120–250	Very Good	High	Medium	Low
Combustion	600–900	Fair	Poor–Moderate	Medium	Medium

2.3 Solid-State Synthesis of $LaV_{1-x}Nb_xO_4$

The solid-state reaction method remains one of the most trusted and scalable routes for synthesizing complex ceramic materials like $LaV_{1-x}Nb_xO_4$ (x = 0.0 to 1.0) [6]. The goal is to form a phase-pure polycrystalline compound by diffusing cations at high temperatures under controlled conditions. The schematic synthesis process using solid state reaction method is shown in Figure 2.1.

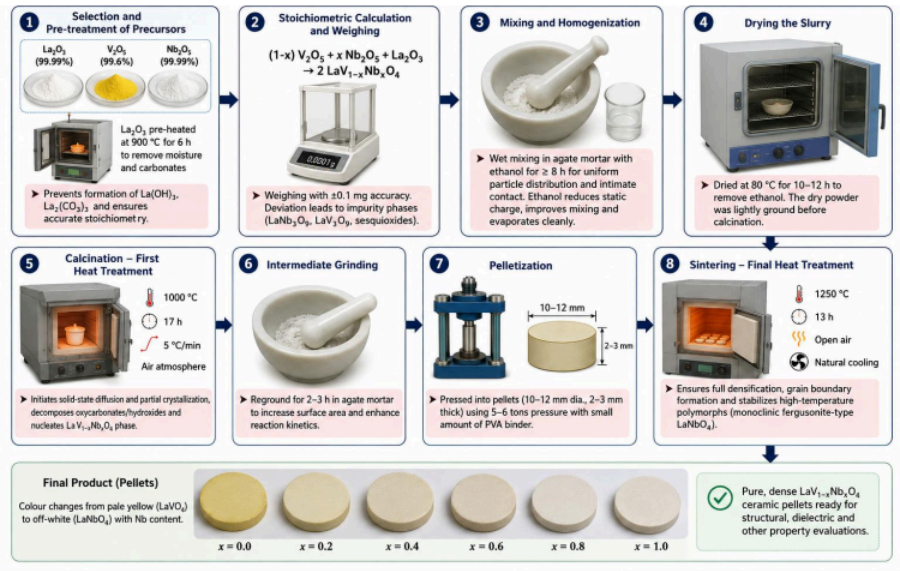


Fig. 2.1: Schematic diagram showing step by step synthesis using solid state route.

Step 1: Selection and Pre-treatment of Precursors

Materials Used

- La_2O_3 (99.99%) – hygroscopic, must be dried
- V_2O_5 (99.6%) – volatile, requires careful thermal handling
- Nb_2O_5 (99.99%) – thermally stable, used as received

La_2O_3 was pre-heated at 900 °C for 6 hours to remove adsorbed moisture and carbonates, as La_2O_3 is highly hygroscopic and forms $La(OH)_3$ or $La_2(CO_3)_3$ upon exposure to air. This step ensures accurate stoichiometry and avoids impurity phases like $La_2O_2CO_3$. Drying rare-earth oxides before weighing is a mandatory step in solid-state synthesis to avoid phase errors due to mass overestimation.

Step 2: Stoichiometric Calculation and Weighing

$$(1-x)V_2O_5 + xNb_2O_5 + La_2O_3 \rightarrow 2LaV_{1-x}Nb_xO_4$$

The weights for each oxide were calculated based on their molecular weights and desired mole fraction (x = 0.0 to 1.0). A precision balance with ±0.1 mg accuracy was used to measure the weights. Any deviation from stoichiometry can result in impurity phases such as $LaNb_3O_9$, LaV_3O_9, or mixed sesquioxides.

Step 3: Mixing and Homogenization

We thoroughly mixed precursors in agate mortar using ethanol as a wet medium for at least 8 hours to achieve uniform particle distribution and prevent localized overheating. We used ethanol because it reduces static charge buildup, improves wet mixing and evaporates cleanly without residues. Wet mixing helps break agglomerates and ensures intimate contact between reacting species.

Step 4: Drying the Slurry

The ethanol-wet slurry was dried at 80 °C for 10–12 hours in an oven to remove residual solvent. The resulting dry powder was lightly ground before calcination.

Step 5: Calcination – First Heat Treatment

The dried powder was placed in alumina crucibles and calcined at 1000 °C for 17 hours in air atmosphere. Heating rate was kept 5 °C/min and the sample was cooled naturally. We kept the temperature 1000 °C because it is sufficient to initiate solid-state diffusion and partial crystallization and below this, reaction kinetics are too slow for phase formation. This step ensures nucleation of $LaV_{1-x}Nb_xO_4$ phase and decomposes intermediate oxycarbonates or hydroxides.

Step 6: Intermediate Grinding

The calcined powder was reground for 2–3 hours using a fresh agate mortar. This enhances reaction kinetics during final sintering by increasing surface area and reducing diffusion distances.

Step 7: Pelletization

The reground powder was pressed into cylindrical pellets (~10–12 mm diameter, 2–3 mm thick) using a uniaxial hydraulic press by applying a pressure of 5–6 tons and a small amount of polyvinyl alcohol (PVA) binder was added to aid pressing. Pelletization improves densification and ensures mechanical integrity for dielectric measurements. Pellets were then sintered at 1250 °C for 13 hours in an open-air furnace to get full densification and grain boundary formation and stabilize high-temperature polymorphs such as monoclinic fergusonite-type $LaNbO_4$. The colour of pallets varied from pale yellow ($LaVO_4$) to off-white ($LaNbO_4$), indicating compositional variation.

2.4 X-ray Diffraction (XRD) Analysis

Francesco Maria Grimaldi, an Italian mathematician, made the earliest known observations of diffraction, which were published in 1665. His experiments revealed an apparent bending of light behaviour that the optics known at the time could not account for. W. L. and W. H. Bragg, father and son, did not begin analysing materials using diffraction until 1912 [7]. M. Laue carried out the first practical X-ray experiment earlier that year, using a copper sulphate crystal as the diffraction grating. The Braggs identified a unique X-ray diffraction pattern for crystalline samples. The locations of the high intensity reflections were discovered to be related to the X-ray beam wavelength

and incidence angle. Crystalline solids comprise approximately 90% of all solid substances. Diffraction patterns are the outcome of X-ray interactions with crystalline materials. X-rays have a wavelength of 1.5 Å, similar to the gap between crystalline solids. They may be found in the electromagnetic spectrum, between gamma rays and ultraviolet. The discovery of X-rays in 1895 allowed researchers to investigate objects at microscopic level. X-rays are highly effective instruments for studying crystalline materials at the atomic level due to their systematic approach. This is possible due to similarities in interplanar spacing (d), upright distance between adjacent atoms, and X-ray wavelength.

X-ray diffraction (XRD) is a fundamental technique used to determine the crystallographic structure, phase purity, and lattice parameters of materials [8]. It is particularly critical in solid-state chemistry, where small variations in structure (such as phase transitions or atomic substitution) can drastically influence physical properties. In $LaV_{1-x}Nb_xO_4$ compounds, XRD is used to Confirm phase formation after calcination and sintering. Further we can use XRD to detect structural transitions (monoclinic to tetragonal or fergusonite types). We used the recorded XRD pattern to calculate the crystallite size, strain, and symmetry of the synthesized sample. We also observed the phase changes based on the composition across our substitution series of x = 0.0 – 1.0.

2.4.1 Working Principle of XRD

XRD is based on Bragg's Law, which defines condition for constructive interference of X-rays scattered from different lattice planes in a crystalline material [9]

$$n\lambda = 2dsin\theta \tag{2.1}$$

Where n is the diffraction order (usually 1), λ is the X-ray wavelength here we used Cu as X-ray source for which λ is equal to 0.154 nm, d is the interplanar spacing, and θ is the angle of incidence.

The Scherer equation (2.2) [10] is used to determine the average crystallite size of materials under examination. In the 2θ scales, β represents full breadth and half maximum, d represents crystallite size, and λ = 1.5404 Å represents the wavelength with the highest X-ray diffraction intensity.

$$d = \frac{0.9\lambda}{\beta cos\theta} \tag{2.2}$$

When a beam of monochromatic X-rays strikes a crystalline powder, each set of crystal planes diffracts the X-rays at characteristic angles depending on its spacing. These diffracted beams are recorded as peaks in the XRD pattern. Each material has a fingerprint XRD pattern, enabling phase identification. Figure 2.2 represents the working of XRD setup.

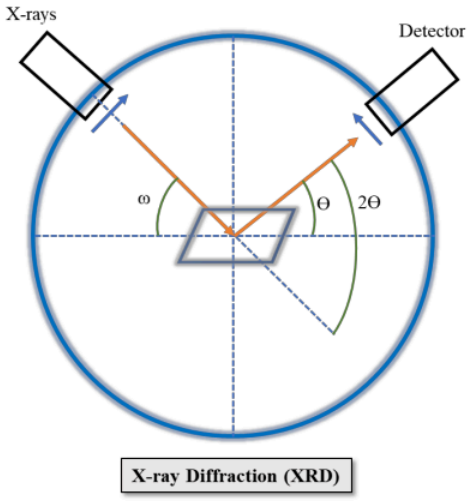


Fig. 2.2: X-ray diffraction working principle.

2.4.2 Instrumentation Details

- **Instrument:** PANalytical X'Pert Powder Diffractometer
- **Radiation Source:** Copper radiation, CuK_α (λ = 1.5406 Å)
- **Configuration:** θ–2θ geometry

- **Scan Range:** $2\theta = 10°$ to $90°$
- **Step Size:** 0.033°
- **Count Time:** ~0.5 s per step
- **Sample Mounting:** Flat sample holders, gently pressed powder surface to minimize preferred orientation
- **Environment:** Room temperature, ambient air

2.4.3 Data Analysis and Rietveld Refinement

The structural analysis used a very successful approach for validating the structure of the synthesized compound. The Rietveld process is an improvement procedure that requires a preliminary examination of the crystal structure [11]. The model contains detailed information on the chemistry and structure, such as the lattice constant, space group atom placements, and thermal properties. The examination was carried out using the application FULLPROF and its graphical interface WINPLOTR. The refining process decreases discrepancies between investigational data and the model, which has been evaluated using the least-squares approach. A collection of included points can be utilised in the analysis to account for the background. Additional parameters include peak anisotropic temperature, broadening, absorption, and shape. The factors χ^2, R_{wp}, and R_{exp} determine how well the fitting fits. The product of the squares of R_{wp} and R_{exp} yields χ^2. R_{wp} is the residual weighted by intensity, while R_{exp} is the anticipated residual value. Once convergence is achieved and the goodness of fit χ^2 value approaches one, the refining phase is complete.

What is Rietveld Refinement?

It is a whole-pattern fitting technique that compares the experimental diffraction pattern to a theoretical one generated from crystallographic models. The goal is to minimize the difference (χ^2) between the observed and calculated intensities by adjusting parameters such as unit cell dimensions, atomic positions, occupancy factors, crystallite size and strain (via peak broadening). The key parameters that are refined using this technique are Phase fractions (monoclinic vs. tetragonal vs. fergusonite), Lattice constants (a, b, c,

and β for monoclinic systems) and Crystallite size (via Scherrer equation or refined micro-strain). Goodness-of-fit values (χ^2) less than 2.5 and low R_{wp} values indicated acceptable refinement quality.

2.4.4 Observations for $LaV_{1-x}Nb_xO_4$ Series

- x = 0.0 ($LaVO_4$): Exhibited a monoclinic monazite-type structure (space group $P2_1/n$), typical for undoped $LaVO_4$.
- x = 0.2–0.8: Showed mixed-phase behaviour, with coexistence of monoclinic and tetragonal phases due to lattice distortion from Nb^{5+} substitution.
- x = 1.0 ($LaNbO_4$): Stabilized into a monoclinic fergusonite-type structure (space group I2/a), confirming complete substitution.
- x = 0.5 ($LaV_{0.5}Nb_{0.5}O_4$): samples at two different sintering temperatures of 1000°C and 1250°C reveals the coexistence of monoclinic monazite-type and tetragonal scheelite-type phases, noting how higher sintering temperatures increase the tetragonal phase fraction and improve crystallinity.

The progressive shift of peaks to lower 2θ values with increasing x confirms lattice expansion due to the larger ionic radius of Nb^{5+} (0.64 Å) compared to V^{5+} (0.54 Å). XRD served as the primary technique to validate the structural evolution of $LaV_{1-x}Nb_xO_4$. It helped confirm single-phase or mixed-phase formation, detect phase transitions, and support the successful incorporation of Nb^{5+} into the V^{5+} sublattice. These insights are essential for correlating microstructure with dielectric and electronic behaviour, as discussed in later chapters. XRD showed the successful phase formation and compositional control across the substitution series and provided clear evidence of structural phase evolution from $LaVO_4$ to $LaNbO_4$ with increasing x. The XRD findings also support later analysis of Raman, XPS, and dielectric results, linking structure to property.

2.5 Scanning Electron Microscopy (SEM)

A scanning electron microscope uses restricted stream of electrons (high energy) to create wide range of signals on surfaces of materials. Interactions between electrons and samples reveal information on the material's outer texture, chemical configuration, crystal-like structure, and composite ingredient alignment. Bulk uses include taking measurements over a certain portion of a material's surface and producing a 2D picture to show longitudinal changes in these qualities. Traditional SEM technologies allow for examination of regions and widths from 1.0 cm to 5.0 microns. SEM may also evaluate specific spots (pointwise) on a material. Scanning Electron Microscopy (SEM) is a powerful tool used to analyse the surface morphology, grain size, porosity, and microstructural features of solid materials at high spatial resolution [12]. For ceramic materials like $LaV_{1-x}Nb_xO_4$, which exhibit complex polycrystalline textures, SEM plays crucial role in understanding link between synthesis parameters, phase formation, and physical properties such as dielectric response and electrical conductivity. In this research, SEM analysis provided visual confirmation of sintering and densification quality, information on grain boundaries, particle size, agglomeration and insights into the effect of Nb^{5+} substitution on grain growth behaviour. Figure 2.3 shows the ray diagram of how electrons travel inside a scanning electron microscope setup.

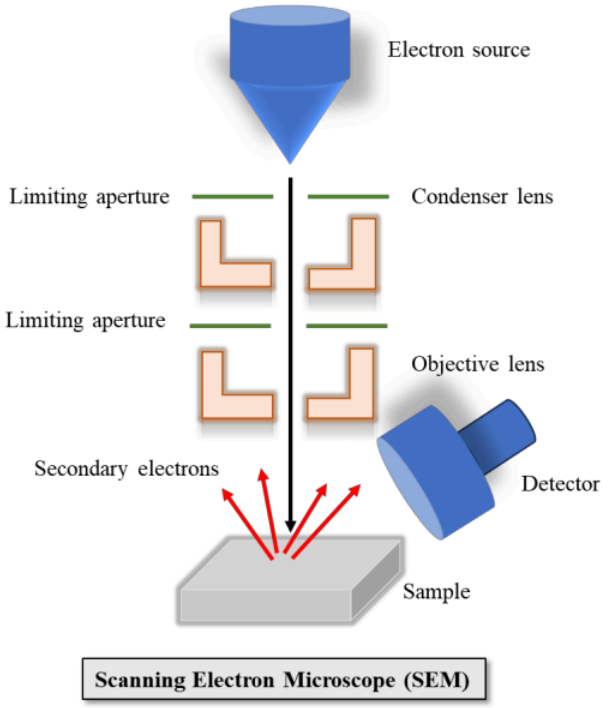


Fig. 2.3: Diagram showing path of electron beam inside SEM.

2.5.1 Principle of SEM

SEM operates by scanning a finely focused high-energy electron beam across sample surface. When accelerated electrons encounter a sample in a SEM, they release a lot of kinetic energy in the form of signal variability due to interactions with the material. These signals are used to identify mineral inclinations and crystal morphologies. They are made up of secondary and diffracted backscattered electrons, which are employed to create SEM pictures. Backscattered and secondary electrons can be used to scan samples. Secondary electrons are best for displaying the shape and geometry of the compound, whereas backscattered electrons highlight elemental variations in interfacial specimens. The SE signal is most commonly used for imaging morphology and grain structure. The resolution of SEM varies up to a few nanometres with an excellent depth of field allowing 3D surface visualization and a magnification range from 20X to over 1,00,000X.

2.5.2 Instrumentation and Operating Conditions

- **Instrument Used:** JEOL JSM-7800F Prime Field Emission SEM
- **Accelerating Voltage:** 15–20 kV
- **Detector:** Secondary electron and backscattered electron detectors
- **Vacuum Mode:** High-vacuum operation for maximum resolution
- **Sample Coating:** Thin layer of **gold (Au)** sputter-coated to prevent charging on the non-conducting oxide surface

We used gold sputter coating which is essential for insulating ceramic samples like $LaV_{1-x}Nb_xO_4$ to prevent charging artifacts and improve image clarity.

2.5.3 Sample Preparation

The pellets are polished for getting cross-sectional SEM, though in the top-view imaging is usually sufficient for our work. Then the samples were mounted on carbon tape on standard SEM stubs. A uniform gold layer (~10–15 nm) was applied using a sputter coater (Quorum Q150R) to render the sample surface conductive and the coated samples were dried in a vacuum desiccator before imaging. Uniform coating is vital for preventing beam damage and maintaining resolution at high magnification.

2.5.4 Observations Across $LaV_{1-x}Nb_xO_4$ Series

In our sample with x = 0.0 ($LaVO_4$) grain size is in the range of ~0.6–0.8 μm, smooth, uniform grains, relatively dense microstructure. For samples with x = 0.2–0.6 slight increase in grain size (~0.9–1.2 μm), emergence of intergranular porosity, some anisotropic grain shapes due to mixed-phase presence were seen. In case of doping with x = 0.8–1.0 ($LaNbO_4$) larger, more irregular grains (~1.5–2.0 μm), diffuse grain boundaries due to enhanced sintering is observed. The grain growth trend suggests that Nb^{5+} incorporation facilitates densification and alters grain boundary mobility, consistent with literature on $LaNbO_4$. SEM images were analyzed using ImageJ software to extract average grain size distributions. A histogram plot was generated for each composition, showing particle frequency vs. size. Statistical parameters like mean grain size, standard deviation, and grain boundary aspect ratio were calculated. Quantitative image analysis supplemented the qualitative SEM interpretation and allowed correlation with electrical properties.

2.5.5 Energy Dispersive X-ray Spectroscopy (EDS)

Although not essential for phase-pure ceramics, EDS was used for elemental mapping [13]. EDS confirmed presence of La, V, Nb, and O with no foreign impurities and provided semi-quantitative data on elemental distribution homogeneity across grains.

2.5.6 Significance of SEM in This Work

SEM analysis provided a direct visual link between synthesis conditions and microstructure, which is pivotal for interpreting grain boundary-related dielectric losses, impedance relaxation mechanisms, porosity and its influence on conduction pathways. In complex oxide systems, dielectric behaviour is not only a function of crystal structure but also of microstructural features such as grain size, porosity, and grain boundary integrity. SEM analysis was indispensable for characterizing the microstructural evolution of $LaV_{1-x}Nb_xO_4$ ceramics. The systematic change in grain morphology and size with increasing niobium content highlights the strong influence of compositional tuning on densification and microstructure. These findings support the dielectric and impedance results discussed in later chapters.

2.6 High-Resolution Transmission Electron Microscopy (HR-TEM) and Selected Area Electron Diffraction (SAED)

Transmission Electron Microscopy (TEM), particularly in its high-resolution mode (HR-TEM), is one of the most powerful characterization techniques for observing the internal atomic-level structure, lattice fringes, crystal defects, grain boundaries, and nanoscale phases of materials [14]. It allows direct imaging of planes and defects within grains, which XRD or SEM cannot resolve. When combined with Selected Area Electron Diffraction (SAED) [15], TEM also provides local crystallographic information from specific regions of interest. In this research, HR-TEM and SAED were used to validate the crystal structure at the atomic scale, interplanar spacing (d-spacing), crystallinity, phase formation, interface, boundary contrast and diffraction symmetry to support XRD findings.

2.6.1 Working Principle

TEM operates by transmitting a beam of high-energy electrons (typically 200 kV) through an ultra-thin specimen (<100 nm). As electrons pass through the sample they

interact with the internal atomic structure and the diffracted electrons produce contrast based on atomic mass and crystal orientation. The image formed reveals atomic lattice fringes. HR-TEM enables imaging of individual lattice planes (<0.2 nm resolution), showing defects, stacking faults, and strain. SAED Mode generates an electron diffraction pattern from a specific area of the sample, offering crystallographic information such as symmetry (monoclinic, tetragonal, etc.), zone axes, and phase purity. Figure 2.4 represents how electron beam generates image using a transmission electron microscope.

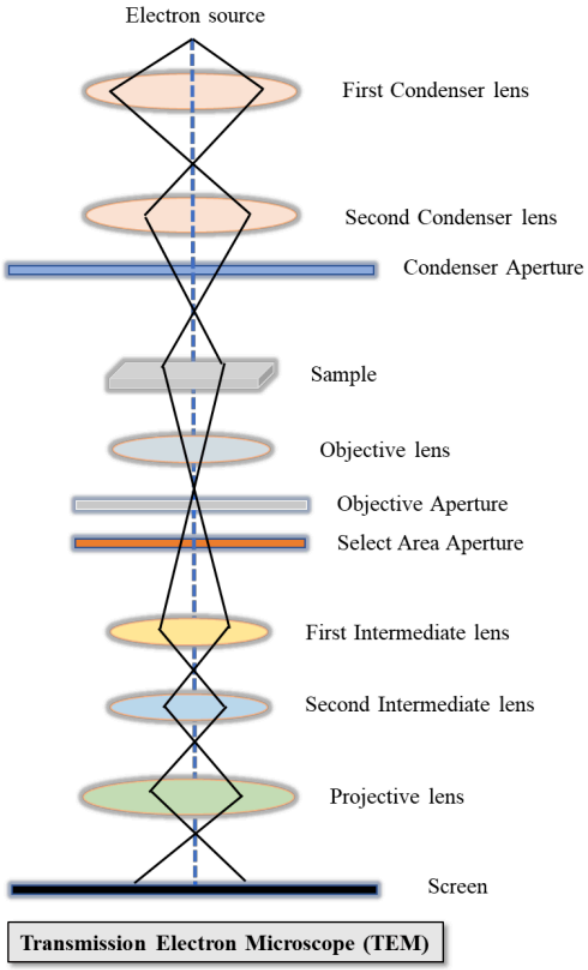


Fig. 2.4: Image formation using a Transmission Electron Microscope.

2.6.2 Instrumentation and Operating Conditions

- **Instrument Used:** JEOL JEM-F200 High-Resolution TEM
- **Accelerating Voltage:** 200 kV
- **Detector:** OneView CMOS camera (4k × 4k)
- **Electron Source:** Field emission gun (FEG)
- **Resolution:** <0.2 nm in HR-TEM mode
- **Working Modes:** Bright field imaging, HR-TEM, SAED

2.6.3 Sample Preparation for TEM

TEM requires ultrathin samples (~100 nm or less) to allow electron transmission. The steps include dispersing small amounts of calcined and sintered powder using ultrasonicator in ethanol for 30 minutes. A few drops of the suspension were placed on carbon-coated copper grids (300 mesh). Then the grids were dried under infrared light or vacuum overnight to eliminate residual solvent and the grids were transferred to the TEM holder under a clean, dust-free environment. Careful dispersion and drying are critical to avoid aggregation and contamination during TEM imaging which were kept in mind while preparing samples.

2.6.4 HR-TEM Observations for $LaV_{1-x}Nb_xO_4$

The obtained images revealed that for x = 0.0 ($LaVO_4$) clear and periodic lattice fringes with d-spacing matching the (121) and (200) planes of monoclinic monazite-type $LaVO_4$ were present. For x = 0.4 and 0.6 lattice fringes appeared less regular; overlapping phases and slight distortion indicated coexistence of monoclinic and tetragonal domains. In case of x = 1.0 ($LaNbO_4$) exhibited well-defined fringes corresponding to monoclinic fergusonite-type structure; measured d-spacing aligned with (−111) and (020) planes. Thus, the HR-TEM confirmed lattice distortion and interplanar rearrangements due to substitutional effects of Nb^{5+}. The SAED patterns further confirmed for x = 0.0 indexed to monazite-type $LaVO_4$ with distinct spot arrays showing monoclinic symmetry, x = 0.4 to 0.8 showed ring + spot hybrid patterns suggesting partial crystallinity or multi-phase coexistence and x = 1.0 pattern matched

monoclinic $LaNbO_4$ with typical two-fold symmetry and sharp spots, confirming high crystallinity. The SAED analysis provides localized crystallographic evidence, supporting XRD-derived phase transitions across the $LaV_{1-x}Nb_xO_4$ series.

2.6.5 Interplanar Spacing (d-spacing) Analysis

Using ImageJ with TEM plugins the lattice fringes were measured directly from HR-TEM micrographs. Experimental d-spacing values were compared with standard ICSD/PDF values which are in agreement with XRD data validated that the structural assignments. TEM imaging at atomic resolution is essential to capture subtle structural evolution that occurs due to Nb substitution, and complements the bulk data from XRD and Raman spectroscopy. The HR-TEM and SAED analysis provided atomic-scale confirmation of phase formation, crystallinity, and interplanar spacing in $LaV_{1-x}Nb_xO_4$ ceramics. These findings were crucial for validating the substitutional effects of Nb^{5+} on the $LaVO_4$ host lattice, supporting structural transitions and heterogeneities observed in XRD and Raman results.

2.7 Raman Spectroscopy

Raman spectroscopy provides detailed information on phase, organic structure, polymorphic behaviour, molecular interactions, and crystallinity. This method evaluates a material's vibrational energy modes using dispersed light. C. V. Raman, an Indian scientist, and K. S. Krishnan discovered Raman scattering in 1928 [16]. Raman spectroscopy provides structural evidence and identifies compounds through unique Raman fingerprints. This information is gathered by analysing the scattering properties of the substance (Raman). When a molecule scatters light, the molecular electron cloud becomes polarised due to the changing electromagnetic field. As a result, the molecule gains energy and absorbs the photon. This is sometimes referred to as the molecule's virtual state and involves a brief response between the molecule and photon. Due to the unstable virtual state, photons are promptly reemitted as diffused light. In scattering trials, atoms' energy is unaltered by photon interaction, resulting in scattered photons with the same wavelength as entering photons. The basic process, Rayleigh scattering (elastic), happens here. Inelastic scattering, which allocates energy between atoms and

dispersed photons, is a less common phenomenon. Stokes scattering occurs when a photon loses energy and expands in wavelength due to energy acquisition by atoms. Anti-Stokes scattering occurs when scattered photons gain energy by relaxing to a higher level, resulting in shorter wavelengths [17]. Quantum physics suggests that anti-Stokes and Stokes processes are equally feasible. Raman spectroscopy detects Stokes Raman scatter, which is often stronger than anti-Stokes scatter. Raman spectroscopy is a powerful, non-destructive tool for probing lattice vibrations (phonons), local structural symmetry, and bonding environments in crystalline materials. It is particularly useful for detecting subtle structural changes, defect formation, and phase coexistence that might not be fully resolved by XRD. In the context of $LaV_{1-x}Nb_xO_4$ ceramics, Raman spectroscopy was employed to confirm phase formation and detect monoclinic-to-tetragonal transformations, analyse the evolution of V–O and Nb–O vibrational modes, track disorder or distortion introduced by B-site ($V^{5+} \rightarrow Nb^{5+}$) substitution and correlate vibrational features with electronic and dielectric properties.

2.7.1 Principle of Raman Spectroscopy

When monochromatic light (usually from a laser) is incident on a material, most photons are elastically scattered (Rayleigh scattering). A small fraction (~1 in 10^6–10^8) undergoes inelastic scattering, exchanging energy with vibrational modes of the material. The energy shift of the scattered photons corresponds to vibrational transitions and is detected as Raman shifts (in cm^{-1}). There are three types of modes detected using raman that are stretching modes of V–O or Nb–O bonds, bending modes in VO_4/NbO_4 tetrahedra and lattice modes at low wavenumbers (<200 cm^{-1}), sensitive to phase changes. Working principle of Raman Spectroscope is shown in Figure 2.5.

2.7.2 Instrumentation and Measurement Parameters

- **Instrument Used:** Renishaw inVia Confocal Raman Microscope
- **Laser Excitation Sources:** 633 nm
- **Power Output:** 0.1–1.0 mW (to avoid sample heating)
- **Grating:** 2400 lines/mm

- **Spectral Resolution:** ~1 cm^{-1}
- **Scan Range:** 100–1100 cm^{-1}
- **Data Analysis Software:** Igor Pro 9, using **Lorentzian peak fitting**

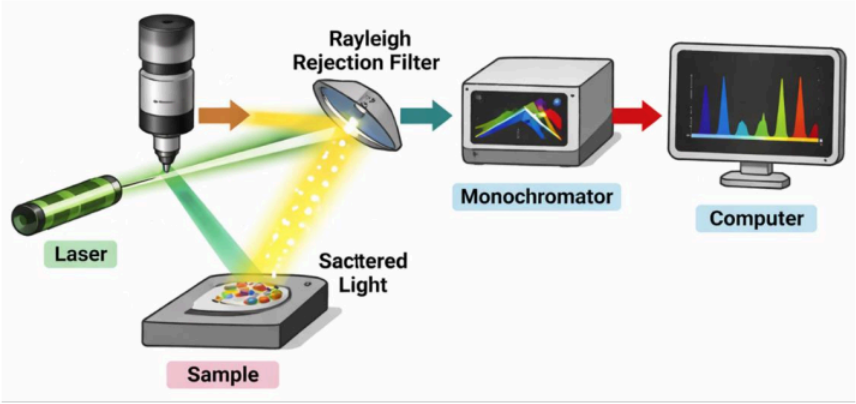


Fig. 2.5: Block diagram representation of working of Raman Spectroscope.

2.7.3 Raman Active Modes in $LaVO_4$ and $LaNbO_4$

Both $LaVO_4$ and $LaNbO_4$ crystallize in low-symmetry monoclinic structures, which give rise to a rich spectrum of Raman-active modes. In $LaVO_4$ (monazite-type, $P2_1/n$) 18 Raman-active modes in the range of 100–1000 cm^{-1} were observed. Strong bands were observed near 865–870 cm^{-1} for V–O symmetric stretching, 780–790 cm^{-1} for V–O asymmetric stretching, 360–470 cm^{-1} for VO_4 bending modes, and 150–200 cm^{-1} for La–O translational modes. In $LaNbO_4$ (fergusonite-type, I2/a) Nb^{5+} forms distorted NbO_4 tetrahedra or NbO_6 octahedra (depending on local environment). The key bands observed at 870–910 cm^{-1} for Nb–O symmetric stretch and 700–800 cm^{-1} for Nb–O asymmetric stretch. The Substitution of Nb^{5+} for V^{5+} causes blue-shift of V–O modes and appearance of new Nb–O related modes, confirming B-site substitution.

2.7.4 Peak Fitting and Quantitative Analysis

All Raman peaks were deconvoluted using multi-peak Lorentzian fitting and Full Width at Half Maximum (FWHM) was used to assess crystallinity and disorder. The area under peaks used to estimate relative mode intensities. Increase in FWHM and decrease in V–O peak intensity with increasing x reflects enhanced lattice distortion due to size mismatch (Nb^{5+} > V^{5+}) [18]. The coexistence of Raman-active bands from both end phases confirms two-phase regions, consistent with XRD and SAED observations. Raman spectroscopy provided crucial insight into the evolution of the bonding environment in $LaV_{1-x}Nb_xO_4$. The progressive disappearance of V–O stretching modes and emergence of Nb–O bands with increasing niobium content validates B-site substitution and associated lattice distortion. These findings correlate strongly with structural transformations captured in XRD and TEM, reinforcing the complementary role of vibrational spectroscopy in phase analysis.

2.8 X-ray Photoelectron Spectroscopy (XPS)

X-ray Photoelectron Spectroscopy (XPS) is a surface-sensitive analytical technique used to investigate the chemical states, oxidation numbers, and electronic environments of elements within a material [19]. It is highly effective for examining oxides, particularly complex ceramics, where multiple oxidation states and ion substitution may alter chemical bonding and functional behaviour. In $LaV_{1-x}Nb_xO_4$, XPS was employed to confirm the oxidation states of La, V, Nb, and O and to analyse the evolution of the electronic structure with Nb^{5+} substitution. The binding energy shifts indicative of bond polarity, charge redistribution, or lattice distortion and successful substitution of V^{5+} with Nb^{5+} at the B-site is also studied.

2.8.1 Principle of XPS

When a material is irradiated with monochromatic X-rays (usually Al Kα, 1486.6 eV), photoelectrons are ejected from the core levels of atoms [20]. The kinetic energy (KE) of these electrons is measured, and the binding energy (BE) is calculated using:

$$BE = h\nu - KE - \phi \tag{2.3}$$

Where ϕ is the spectrometer work function. The binding energy is element-specific and sensitive to the chemical environment, making XPS an excellent tool for distinguishing oxidation states. Figure 2.6 represents how sample is characterized using X-ray photoelectron spectroscopy.

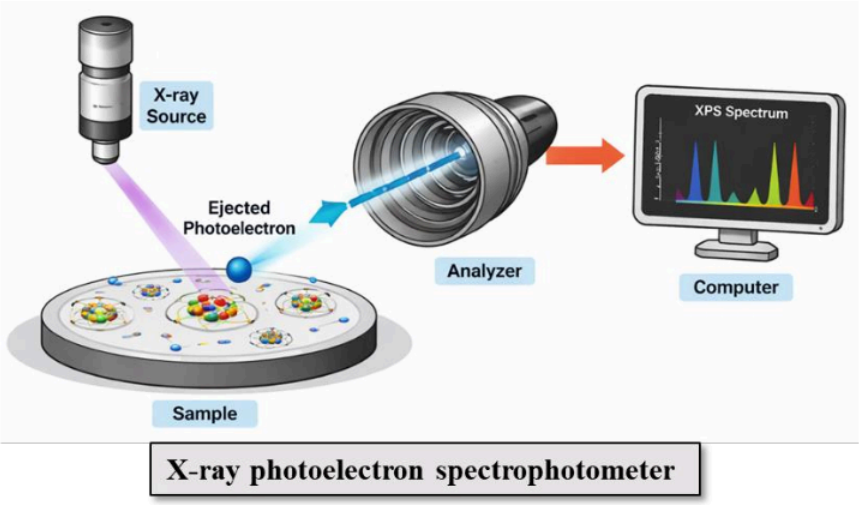


Fig. 2.6: Schematics of X-ray photoelectron spectroscopy.

2.8.2 Instrumentation and Parameters

- **Instrument Used:** AXIS Supra (Kratos Analytical Ltd.)
- **X-ray Source:** Monochromatic Al K_α (1486.6 eV)
- **Pass Energy:** 20 eV (high-resolution scans)
- **Step Size:** 0.1 eV (core-level scans)
- **Charge Compensation:** Flood gun used to neutralize surface charging
- **Calibration:** C 1s peak fixed at 284.6 eV
- **Software**: Igor Pro 9, Voigt-function peak fitting

2.8.3 Core-Level Spectra and Peak Assignments

XPS analysis was employed to assign peals to different states of elements. For La 3d Spectrum two main doublets La $3d_{5/2}$ at 834 eV and La $3d_{3/2}$ at 851 eV were observed.

The satellite peaks at 837 eV and at 854 eV arise due to final-state effects that confirms La^{3+} oxidation state [21]. For V 2p Spectrum (for $x \leq 0.6$) the V $2p_{3/2}$ at 516.8 eV and V $2p_{1/2}$ at 524.3 eV was observed which are consistent with V^{5+} oxidation state in VO_4^{3-} tetrahedra that disappears at x = 1.0 (i.e. full Nb substitution). In case of Nb 3d Spectrum (for $x \geq 0.2$) the Nb $3d_{5/2}$ at 207.3 eV and Nb $3d_{3/2}$ at 210.1 eV corresponds to Nb^{5+} in NbO_4/NbO_6 coordination. The peak shifts observed as a function of x. In O 1s Spectrum the main peak at 530.1 eV (lattice oxygen) and shoulder at 531.5 eV attributed to surface hydroxyls or adsorbed water. The peak broadening may suggest oxygen vacancies or bonding variation. The Binding Energy Shifts Interpretates the gradual positive shift in La 3d and O 1s peaks with increasing x and reflects increased electronegativity difference and stronger metal–oxygen bonding with Nb^{5+} incorporation which suggests enhanced lattice polarization and possible impact on dielectric properties. The binding energy shifts in XPS are a fingerprint of subtle electronic structure rearrangements and bond polarization changes within oxide lattices.

2.8.4 Peak Deconvolution and Area Analysis

Peak fitting employed Voigt functions (Gaussian–Lorentzian hybrid) to account for instrument broadening and natural line width [22]. The peak area ratios and relative intensities used for estimating atomic ratios (La/V/Nb/O), validating Nb substitution trend and assessing surface oxygen species contribution. In this work we validated that both V and Nb retain their +5 oxidation states throughout the series and confirmed no reduction to lower valence states, which could affect conductivity. This study supported the B-site substitution mechanism and linked chemical shifts to structural distortion and corroborated phase evolution trend seen in XRD and Raman studies. XPS offered surface-level chemical state insight, bridging structural and electronic domains of analysis in substituted oxide systems [23]. XPS analysis was vital in confirming the successful substitution of Nb^{5+} at the V^{5+} site without altering the oxidation states of the constituent cations. It provided rich detail on bonding environments and surface chemistry, complementing the bulk structural and vibrational data from XRD and Raman. These findings contribute directly to the understanding of dielectric and electronic behaviour explored in subsequent chapters.

2.9 Dielectric and Impedance Spectroscopy

Dielectric and impedance spectroscopy techniques are crucial for understanding the electrical transport, polarization mechanisms, and interfacial phenomena in polycrystalline materials [24]. They provide frequency and temperature - dependent insights into the dielectric constant (ε′) and loss (tan δ), impedance and modulus spectra, conduction mechanisms (hopping, grain boundary effects), and relaxation behaviour and defect-related dynamics [25]. In $LaV_{1-x}Nb_xO_4$, dielectric and impedance studies were used to evaluate the impact of Nb^{5+} substitution on dielectric properties, relaxation and conduction models, and high-temperature response suitable for applications in capacitors, sensors, or SOFCs.

2.9.1 Fundamental Concepts

Dielectric Constant (ε′)

Dielectric constant quantifies the material's ability to store electric charge via polarization when exposed to an alternating electric field [26]. It can be calculated using the equation 2.4 where C is the measured capacitance, d is the sample thickness, A is the electrode area used, and ε_0 is the permittivity of free space.

$$\varepsilon' = \frac{C.d}{\varepsilon_0.A} \tag{2.4}$$

Dielectric Loss (tan δ)

Dielectric loss represents the energy dissipated due to polarization lag which is shown in equation 2.5

$$tan\delta = \frac{\varepsilon''}{\varepsilon'} \tag{2.5}$$

Complex Impedance (Z)

$$Z^*(\omega) = Z'(\omega) - jZ''(\omega) \tag{2.6}$$

Here Z′ is real part i.e. resistive component, and Z″ is imaginary part i.e. capacitive/reactive component. It is often plotted as Nyquist plots (Z" vs Z') to separate grain, grain boundary, and electrode contributions. M is the complex modulus which is

useful for identifying relaxation processes suppressed in impedance spectra represented in equation 2.7.

$$M^*(\omega) = \frac{1}{\varepsilon^*(\omega)} = M' + jM'' \quad (2.7)$$

2.9.2 Experimental Setup and Measurement Conditions

- **Instrument:** (Implied) precision impedance analyser or LCR meter
- **Sample:** Sintered pellets (~10 mm diameter, ~2 mm thick)
- **Electrodes:** Silver paste or sputtered Au for good ohmic contact
- **Frequency Range:** 100 Hz to 1 MHz
- **Temperature Range:** Room temperature to 600 °C
- **Measurement Atmosphere:** Ambient air; stable heating ramp

2.9.3 Dielectric Response Across $LaV_{1-x}Nb_xO_4$

Dielectric Constant (ε′)

As we increase temperature ε′ also increases, typical for thermally activated dipolar or defect-based polarization [27]. The Nb substitution enhanced ε′ in the intermediate range (x = 0.2–0.8), likely due to increased space charge polarization, grain boundary contributions and distortion of lattice symmetry.

Dielectric Loss (tan δ)

It is low at room temperature and increases with temperature. The peaks in tan δ suggest relaxation phenomena which is shifted to higher frequencies at elevated temperatures [28]. This indicates Debye-like relaxation modulated by temperature and composition.

2.9.4 Impedance Spectra (Nyquist Plots)

The Nyquist plots exhibited semicircular arcs which are characteristic for materials [29]. The high frequency arc is the grain (bulk) resistance (R_1) and the low frequency arc is the grain boundary resistance (R_2). For x = 0.0 to 0.6, both arcs visible, implying significant grain boundary effects while for x = 1.0, a single arc dominated which

attributed to improved densification and decreased grain boundary resistance. Arc compression and merging at higher x-values point toward reduced electrical inhomogeneity due to Nb^{5+} incorporation [30].

2.9.5 Modulus Spectra (M′ vs. M″), AC Conductivity and Jonscher's Power Law

The M″ plots displayed peaks shifting toward higher frequencies with increasing temperature. These peaks represent relaxation processes, governed by hopping or trapped charges [31]. The broadened, asymmetric peaks suggest non-Debye relaxation which is the distribution of relaxation times [32]. The AC conductivity was calculated by the equation 2.8 which showed dispersion at high frequencies, plateau at low frequencies and it was fitted using Jonscher's universal power law shown in equation 2.9. Here σ_{dc} is frequency independent conductivity, A is pre-exponential factor and s is the frequency exponent ($0 < s < 1$).

$$\sigma_{ac}(\omega) = \varepsilon_0 . \varepsilon'' . \omega \tag{2.8}$$

$$\sigma(\omega) = \sigma_{dc} + A\omega^s \tag{2.9}$$

For x = 0.0–0.8: exponent s decreases with temperature which is due to Overlapping Large Polaron Tunnelling (OLPT) [33], and for x = 1.0 value of s increases with T which is due to Non-Overlapping Small Polaron Tunnelling (NSPT) [34].

2.9.6 Activation Energy and Relaxation Times

Arrhenius plots (log σ_{dc} vs. 1/T) showed linear behaviour, confirming thermally activated conduction [35]. It is calculated using the equation 2.10 and the relaxation times τ was estimated from M″ peaks using equation 2.11. The value of τ decreased with increasing T, consistent with rapid dipolar reorientation.

$$\sigma_{dc} = \sigma_0 \exp\left(-\frac{E_a}{kT}\right) \tag{2.10}$$

$$\tau = \frac{1}{2\Pi f_{max}} \tag{2.11}$$

Impedance and dielectric spectroscopy provided a comprehensive understanding of charge transport and dielectric behaviour in $LaV_{1-x}Nb_xO_4$ ceramics. The study revealed

that enhancement of ε′ and suppression of grain boundary resistance with Nb substitution can be seen. Composition-dependent relaxation dynamics and switching of conduction mechanism from OLPT to NSPT with increasing x is also studied. These results, when correlated with microstructure and chemical states, form the basis for evaluating $LaV_{1-x}Nb_xO_4$ as a promising dielectric or sensing material.

2.10 Summary

In this chapter, we have systematically presented the synthesis methodology and comprehensive characterization techniques employed in the investigation of the $LaV_{1-x}Nb_xO_4$ (x = 0.0 to 1.0) ceramic system. The chapter began with an overview of common synthesis techniques for ceramic oxides, including solid-state reaction, sol-gel, co-precipitation, hydrothermal, and combustion methods. A detailed justification was provided for selecting the conventional solid-state route, owing to its scalability, cost-effectiveness, and suitability for high-temperature phase formation in rare-earth vanadates and niobates. The step-by-step synthesis protocol was outlined, including drying of precursors, stoichiometric mixing, prolonged grinding, calcination at 1000 °C, and final sintering at 1250 °C. These steps ensured homogeneity, phase purity, and densification of the ceramic pellets, which were then subjected to multi-technique characterization. Each characterization method was elaborated with its principle, instrumental details, analysis procedures, and specific findings:

- **XRD** confirmed crystal structure, phase evolution, and lattice distortion via Rietveld refinement.
- **SEM** revealed grain morphology, porosity, and densification trends, supported by particle size analysis.
- **HR-TEM and SAED** provided atomic-scale images of lattice fringes, d-spacing, and diffraction patterns, corroborating phase identification.
- **Raman Spectroscopy** identified vibrational modes, phase coexistence, and bond distortion due to B-site substitution.
- **XPS** established oxidation states, chemical shifts, and charge redistribution with increasing niobium content.

- **Impedance and Dielectric Spectroscopy** offered insights into conduction mechanisms, relaxation processes, and grain/grain boundary responses as a function of frequency, temperature, and composition.

Together, these results laid the foundation for understanding the structure–property relationships of $LaV_{1-x}Nb_xO_4$ ceramics, forming the basis for the detailed analysis and discussion presented in subsequent chapters.

Chapter 3

Structural, Vibrational and Electronic Properties of Nb Substituted Orthovanadates $LaV_{1-x}Nb_xO_4$

In this chapter, we investigate the structural, vibrational, morphological, and electronic properties of Nb substituted orthovanadate $LaV_{1-x}Nb_xO_4$ samples prepared by the solid-state reaction method. The x-ray diffraction (XRD) analysis reveals the presence of three crystal structures [monoclinic monazite ($m-m$) type for the $x = 0$, two-phase equilibrium of monoclinic monazite ($m-m$) and tetragonal scheelite ($t-s$) type for the $0.2 \leq x \leq 0.8$, and monoclinic fergusonite ($m-f$) type for the $x = 1$ samples] with an increase in Nb^{5+} concentration. The Raman spectroscopy and x-ray photoelectron spectroscopy (XPS) were employed to study the vibrational and electronic properties of all the samples, respectively. In order to choose an excitation wavelength that does not cause undesirable fluorescence and has observable intensities of all the vibrational modes, the Raman spectra are collected using 532 nm, 633 nm, and 785 nm laser lines. With increasing the Nb^{5+} concentration, new Raman modes associated with Nb-bonds are clearly visible and the intensity of V-bonds assigned modes is decreasing. The XPS analysis shows the unchanged 3+ oxidation state of La ion where the intensity of the V 2*p* core-level decreases while the Nb 3*d* core-level increases with *x*. The equal spin-orbit energy splitting of the states is confirmed by the average energy difference (across La core-level spectra for all the samples) for state I as well as bonding and anti-bonding of state II. Interesting, the relative intensity of La 3*d* state I and state II show systematic change with Nb doping altering the metal ligand overlap. We discuss and provide insight into the evolution of the structural, morphological, and chemical features with Nb substitution in $LaV_{1-x}Nb_xO_4$ samples.

3.1 Introduction

In various polycrystalline oxides, rare earth orthovanadates (RVO_4; R-Rare earth elements) are interesting because of their potential applications in catalysis, polarizers, luminescent materials, and laser host materials [1– 3]. Also, researchers have reported that complex oxide materials show interesting structural, magnetic and electronic properties [4–7], and may be utilized for various applications such solid oxide fuel cells and as an electrode material for Lithium-ion batteries due of their high specific capacity and cycle stability [8]. It is interesting to note that the lanthanum based orthovanadates $LaVO_4$ shows the structural trend in rare-earth family, it crystallizes in tetragonal–zircon (*t*–*z*) type polymorphs with space group $I4_1/amd$ and monoclinic–monazite (*m* − *m*) type polymorph with space group $P2_1/n$. However, it thermally stabilizes in *m* − *m* type, whereas the *t* − *z* structure remains in metastable state at room temperature, because of the largest ionic radius of La^{3+} in lanthanide series, it has a higher oxygen coordination number (9) in *m* − *m* type structure as compared to 8 in *t* − *z* type [9]. The zircon structure contains a pattern of VO_4 tetrahedra (having four identical V-O bonds) [10] and RO_8 dodecahedra (coordination no. 8), sharing their edges alternatively and linked together in chains along the *c*–axis. In the monazite structure, deformed VO_4 tetrahedra with four different V-O bonds [11] are connected to RO_9 polyhedra (coordination no. 9) and sharing their edges. The zircon type $LaVO_4$ sample is difficult to prepare at ambient conditions by conventional solid state reaction method but few reports say that it can be synthesized and stabilized by hydrothermal and precipitation methods [12–14].

The structural and electronic properties of lanthanum orthovanadate with pentavalent niobium substitution are vital to understand for their practical use. Though the parent compound $LaVO_4$ with substitution at the La site has been extensively explored [15, 16], there are very few studies to understand the effect of substitution at V site [17, 18]. As the niobium is located just below vanadium in the periodic table and has many advantages like Vanadium prices have recently risen to about 300% higher, niobium (Nb^{5+}) is biocompatible, isoelectronic to vanadium ion and has a larger ionic radius (0.48 Å) with four coordination numbers in comparison to vanadium ion (0.36 Å) [19]. The $LaNbO_4$ is a rare earth niobate and shows a well-known temperature and composition/substitution-induced structural transformation. For example, the $LaNbO_4$ undergoes a thermally

induced structural transition from monoclinic fergusonite ($m-f$) with space group I2/a to tetragonal scheelite ($t-s$) with space group $I4_1/a$) phase at ~495 °C [20]. Similarly, it undergoes structural transformation by substituting Nb^{5+} at V^{5+} site [21]. It has been reported that lanthanum niobate shows interesting properties and very useful for technological applications such as proton conductivity [22, 23], good dielectric, high energy emission using X-ray excitation [24] and its potential for applications in a variety of fields, including sensors [25], contrast agents, waveguides, ferroelectrics [26], phosphors [27], laser crystals [28], luminophores, LEDs [29], etc.

In this chapter, we study the structural, vibrational, morphological, and electronic properties of $LaV_{1-x}Nb_xO_4$ using various experimental tools like x-ray powder diffraction (XRD), scanning electron microscopy (SEM), high resolution transmission electron microscopy (HR-TEM), selected area electron diffraction (SAED), Raman spectroscopy, and x-ray photoelectron spectroscopy (XPS). We find the phase purity and structural transition by performing the Rietveld refinement of the measured XRD patterns at room temperature. The Raman spectra of $LaV_{1-x}Nb_xO_4$ samples are measured with different excitation wavelengths of 532 nm, 633 nm, and 785 nm, where we find significant intensity of all the Raman active modes as well as interesting changes with Nb substitution. The Raman spectra exhibit a pattern of maximum intensity peaks that is compatible with Badger's rule. The structural phase transition observed in the XRD analysis of $LaV_{1-x}Nb_xO_4$ is also supported by the intensity variation in the Raman mode observed in the samples with increasing Nb concentration. Through the SEM micrographs, we identify that the samples contain fine particles along with pores as well as changes in particle size and shape can be seen in the surface images of the samples. The core-level photoemission reveals the oxidation state and electronic structure of the constitute elements in these samples. The intensity of the core-level spectra of all the samples varied systematically with an increase in Nb^{5+} concentration, as shown by XPS analysis. The average energy difference (for the La core-level spectra of all the samples) for state I, state II bonding, and state II anti-bonding verified the equal spin-orbit energy splitting of the states. Moreover, we find a systematic change in the relative intensity of La 3*d* state I and state II with Nb doping, which suggest an altering in the metal ligand overlap.

3.2 Experimental

We use solid-state reaction method to prepare $LaV_{1-x}Nb_xO_4$ (x = 0 to 1) samples by mixing V_2O_5 (99.6%, Sigma), Nb_2O_5 (99.99%, Sigma), and La_2O_3 (99.99%, Sigma) as precursors in the stoichiometric proportions. The La_2O_3 was pre-dried for 6 hrs at 900°C to remove the moisture. After that the mixture was ground evenly for 8 hours, then heated for 17 hrs at 1000°C. The mixture was then reground and sintered at 1250°C for 13 hrs to improve the crystallinity of the samples. The phase purity and structural parameters of $LaV_{1-x}Nb_xO_4$ were determined using Panalytical XPert^3 powder x-ray diffractometer at room temperature using the Cu source of Kα radiation (λ = 1.5406 ˚A). We use the step size of 0.033° for each XRD scan taken in the 2θ range from 10° to 90°. The lattice parameters are extracted by the Rietveld refinement of XRD patterns using FullProf software, where linear interpolation is used to fit the background. We use Jeol JSM-7800F Prime field emission scanning electron microscope (FE-SEM) with LN_2 free SDD X-max 80 EDS detector in high vacuum mode to produce the scanning electron microscope (SEM) micrographs of the materials' surfaces. The analysis of particle size and change in morphology of $LaV_{1-x}Nb_xO_4$ was done using ImageJ software by analyzing SEM micrographs at the surface of the pellet samples. In order to execute FE-SEM, the non-conducting $LaV_{1-x}Nb_xO_4$ pellets were turned into conducting by coating the surface with a thin layer of Au using a sputter coater. We use the JEOL/JEM-F200 microscope, equipped with thermal electron field emission and OneView CMOS camera (4k × 4k pixels), to collect HR-TEM data by operating the system at an acceleration voltage of 200 keV.

The Raman spectra were recorded at room temperature with the Renishaw inVia confocal Raman microscope using 2400 lines/mm grating, 10X objective, and three different wavelengths; (i) 532 nm, gas laser with a power of 1 mW, (ii) 633 nm, where the semiconductor diode laser with a power of 1 mW, (iii) 785 nm semiconductor diode laser with a power of 0.1 mW. The samples can be identified by their particular Raman fingerprint, and their structural and chemical information can be discovered through the examination of several Raman active modes in $LaV_{1-x}Nb_xO_4$. The x-ray photo emission spectroscopy (XPS) measurements are done using AXIS Supra instrument (Kratos Analytical Ltd). The survey spectra and core level spectra (La 3*d*, Nb 3*d*, V 2*p*, and O 1*s*, for each sample), were recorded at room temperature using the monochromatic X-ray source: Al Kα-1486.6 eV (step size 1 eV for the survey and 0.1 eV for core level spectra),

with a charge neutralizer, is used to offset the charging impact in these insulating materials. The pass energy of the analyser was 160 eV and 20 eV for the survey and core-level spectra, respectively. For all the wide scans and core-level spectra, the C 1*s* peak is fitted to obtain the peak binding energy (BE) and the calibration for charge correction was done using the C 1*s* BE reference at 284.6 eV for each sample. We utilize the Igor Pro 9 software to analyze the observed Raman spectra and fitted the modes using the Lorentzian peak function as well as XPS spectra using the Voigt function.

3.3 Results and Discussion

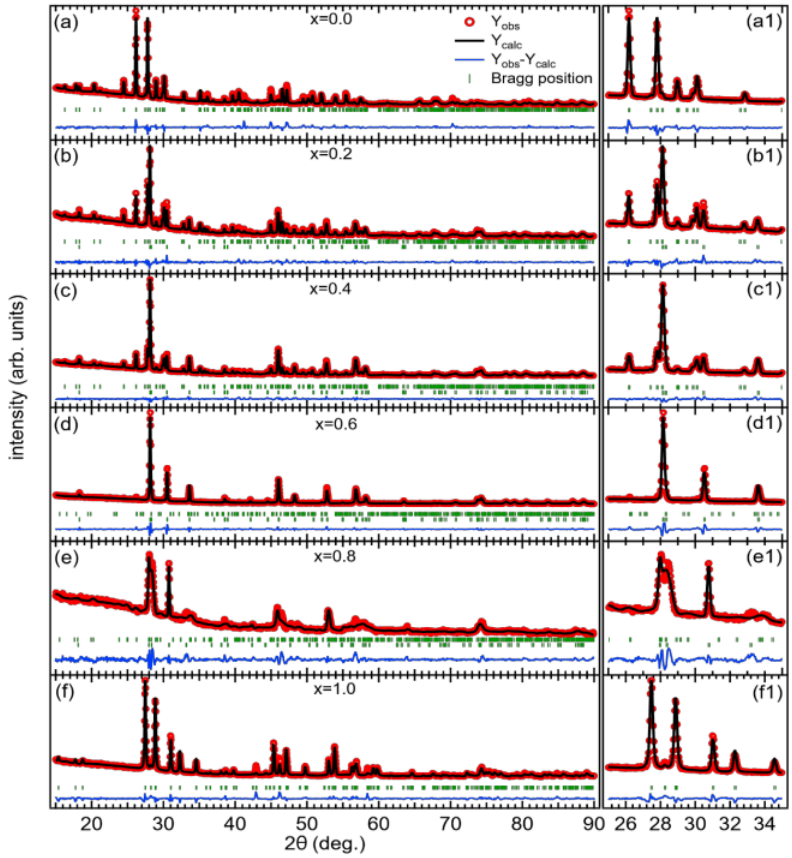


Fig. 3.1: (a–f) The Rietveld refined x-ray diffraction patterns of $LaV_{1-x}Nb_xO_4$ (x = 0–1) samples. The experimental, simulated, and difference between the experimental and simulated spectra are shown by open red circles, black solid lines, and blue solid lines, respectively. The Bragg positions corresponding to their respective space groups are shown by green vertical markers. In the side of each panel (a1–f1), we show partial amplification for clarity between 2θ = 25–35° for all the samples.

The Rietveld refined room-temperature x-ray diffraction (XRD) patterns of the polycrystalline $LaV_{1-x}Nb_xO_4$ (x = 0–1) samples are displayed in Figure 3.1 and lattice parameters of the samples are summarised in Table 3.1, where we can see that angle β is increasing in the m−m type phase of $LaV_{1-x}Nb_xO_4$ samples with Nb^{5+} substitution due to higher ionic size of Nb^{5+} as compared to V^{5+}. The crystallization of $LaV_{1-x}Nb_xO_4$is clearly observed in three different phases depending on the substitution of Nb^{5+} at the site of V^{5+}, and also been reported by Aldred *et al.* in ref. [21]. We observe that the structure changes from $m - m$ to $m - f$ with increase in the Nb^{5+} concentration from 0 to 100%. For the x = 0 and 1, a pure monoclinic phase is obtained with no impurity peaks. In between x = 0.2 and 0.8, a monoclinic monazite ($m - m$) and a tetragonal scheelite ($t - s$) type phases coexist. Moreover, all the Bragg reflections of $LaVO_4$ and $LaNbO_4$ can easily be indexed to the $m - m$ and $m - f$ phases with the space group $P2_1/n$ and I2/a for the x = 0 and 1 samples, respectively. We find that the contribution of space group $I4_1/a$ is increasing from the x = 0.2 to 0.8 samples (see Table 3.1) due to the increase of $t - s$ phase with the substitution of Nb^{5+} at the site of V^{5+} in $LaV_{1-x}Nb_xO_4$ samples. So, it can clearly be seen that the $LaV_{1-x}Nb_xO_4$ samples crystallize in monoclinic monazite (m−m) type (x = 0), coexistence of monoclinic monazite ($m - m$) and tetragonal scheelite ($t - s$) type ($0.2 \leq x \leq 0.8$), and monoclinic fergusonite ($m - f$) type (x = 1) [21, 30].

Moreover, for the x = 0 sample, the $m - m$ type crystal structure shows high intensity diffraction peaks corresponding to (200) as well as (120) crystal planes at 26.17° and 27.78°, respectively. However, the t−s type structure contains a peak corresponding to (112) plane at 28.08°, and the m−f type structure shows high intensity peaks for the (121) and (121) planes at 27.5^o and 28.9^o respectively. In the measured XRD pattern for the x = 0.2 to 0.8 samples, the diffraction peaks for the (200), (120) and (112) planes are present, which clearly indicate the co–existence of both the $m - m$ or $t - s$ type structures. The presence of (110) plane at 17.65° for the x = 0.2 and 0.4 samples is due to the dominance of m−m type structure in the $LaV_{1-x}Nb_xO_4$. The (200) and (120) peaks are also present in these samples; however, their intensity decreasing with higher concentration of Nb substitution and become negligible for the $x \geq 0.6$ sample. As the Nb^{5+} concentration becomes more than V^{5+} concentration the $t - s$ type structure dominates, which results in the reduction/absence of diffraction peaks corresponding to (200) and (120) planes. The

variation in peak intensity corresponding to (200) and (120) crystal planes and the presence of (112) plane indicate the co–existence of $t - s$ and $m - m$ type structures for the $x = 0.2$ to 0.8 samples. This also validates that the $m - m$ type structure ($P2_1/n$) is decreasing and $t–s$ type structure ($I4_1/a$) is increasing with increasing the Nb concentration, i.e., from the $x = 0.2$ to 0.8 samples. The determined % of phases by Rietveld refinement of XRD data is presented in Table 3.1. For the $x = 1$ sample, the presence of (121) and (121) peaks further confirm the $m–f$ type structure of $LaNbO_4$ and consistent with literature [31].

Note that pure $m–m$ and $m–f$ phases are observed for the $x = 0$ and 1 samples, respectively. However, for the $x = 0.2–0.8$ samples, both the monoclinic and scheelite tetragonal phases coexist in a certain ratio. These results reveal that $LaV_{1-x}Nb_xO_4$ samples undergo three phase transformation; monoclinic monazite ($m - m$) type (for the $x = 0$), two-phase equilibrium of monoclinic monazite ($m–m$) and tetragonal scheelite ($t–s$) type ($0.2 \leq x \leq 0.8$), and monoclinic fergusonite ($m - f$) type (for the $x = 1$) with increased substitution of Nb^{5+} at the V^{5+} site. It is quite interesting to note that small amount of Nb^{5+} substitution can transform $LaVO_4$ from $m–m$ phase to mix of $m–m$ and $t–s$ phases. It has also been observed that $LaNbO_4$ shows structural transition from monoclinic to a tetragonal phase at ~495°C. This structural transformation is very important in governing the protonic conductivity of $LaNbO_4$ [32]. For some compositions of $LaV_{1-x}Nb_xO_4$, this transition temperature shifts near room temperature. The reported temperature-dependent XRD measurements also suggest that at $x = 0.75$ (25% substitution of V^{5+} at Nb^{+5} sites in $LaNbO_4$) [21], it possess a tetragonal structure at room temperature as its transition temperature is 250 K. The XRD pattern below 250 K shows some residual intensity (broadened lines) of tetragonal structures because of precursor effects. Similarly, we can see broad peaks in XRD patterns for the $x = 0.8$ sample due to the above-mentioned effect [21]. As we increase the Nb concentration, we find some new peaks appearing in the $x = 0.2$ sample at 33.56^o, 52.68^o, 56.69^o, and 58.06^o. All these peaks are the symbols of t–s structure that belongs to (020), (116), (312), and (224) planes, respectively [33]. These peaks maintained up to the $x = 0.8$ sample, which confirms presence of some $t - s$ phase, and also indicate the substitution-induced phase transformation. This is an important finding that $LaNbO_4$ can possess a tetragonal structure at room temperature by just 20%

replacement of Nb^{5+} sites by the V^{5+} sites. This result opens the possibility for a wide range of applications of $LaNbO_4$ at room temperature. All these patterns discussed above suggest that substitution of larger Nb^{5+} (r = 0.48 ˚A) ion for V^{5+} (r = 0.36 ˚A) affects the lattice constant of $LaV_{1-x}Nb_xO_4$ and confirms the transformation of 3 different phases with increasing concentrations of Nb^{5+}.

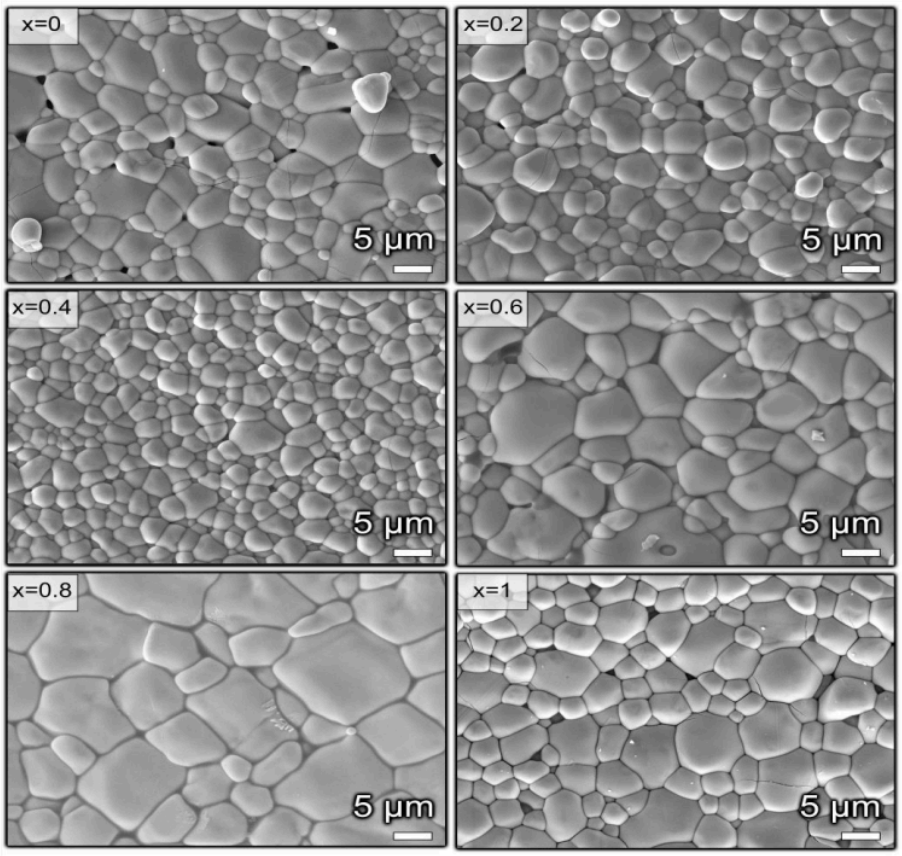


Fig. 3.2: The scanning electron microscope images of the $LaV_{1-x}Nb_xO_4$ (x = 0–1) samples.

The scanning electron microscope images of the $LaV_{1-x}Nb_xO_4$ for the x = 0–1 are shown in Figure 3.2, which depict the closed packed surface morphology in all the samples and some variation in the particle size is clearly visible. The pores are clearly visible from the top view of the surface. We can see that with the increase in Nb^{5+} concentration, the particle size slightly decreases from x = 0 to x = 0.4 sample, then increases and becomes

maximum at $x = 0.8$ and again decreases for the $x = 1$ sample. An average particle size (D) of $LaV_{1-x}Nb_xO4$ is 5.14 μm for the $x = 0$, 4.22 μm for the $x = 0.2$, 3.56 μm for the $x = 0.4$, 8.73 μm for the $x = 0.6$, 11.31 μm for the $x = 0.8$, and 5.70 μm for the $x = 1$ samples. It is found that the change in crystal surface morphology of $LaV_{1-x}Nb_xO_4$ samples with increasing Nb^{5+} concentration causes variation in the particle size and shape.

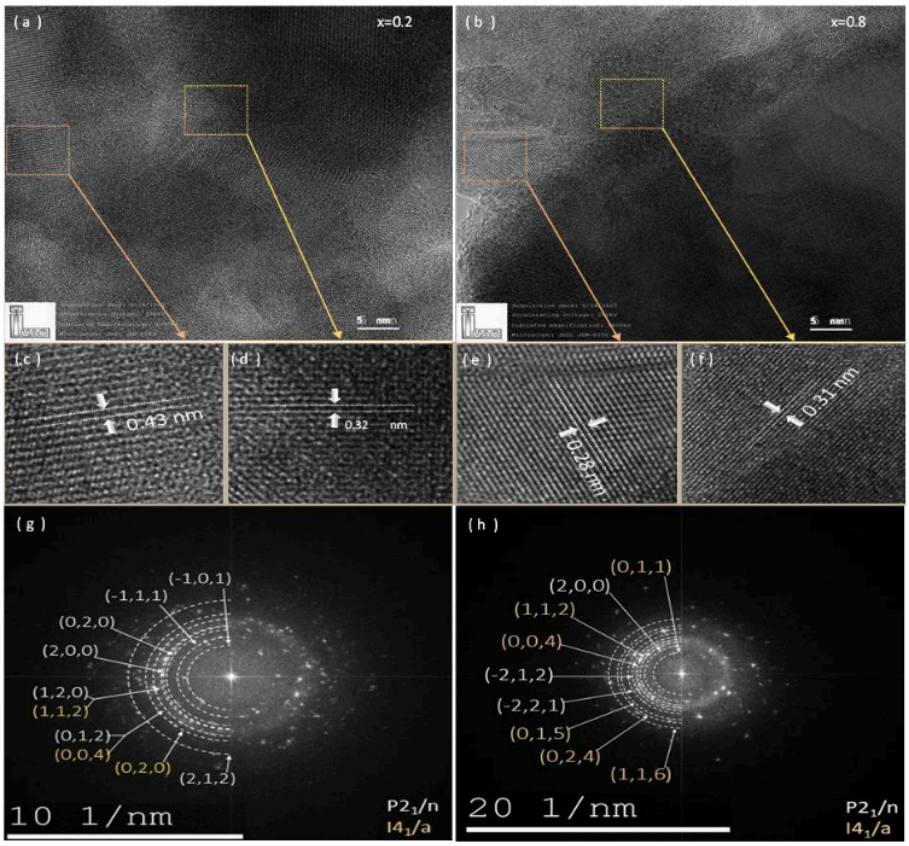


Fig. 3.3: The HR-TEM images of $LaV_{1-x}Nb_xO_4$ for the (a) $x = 0.2$ and (b) $x = 0.8$ samples. The magnified view of HRTEM images in (c, d) for the $x = 0.2$ sample, and (e, f) for the $x = 0.8$ sample. (g, h) The SAED patterns for the $x = 0.2$ and 0.8 samples, respectively.

Further, in Figure 3.3 (a, b) we display the HR-TEM images indicating distinct sets of planes with characteristic spacing for the $x = 0.2$ and 0.8 samples. The images in Figures 3.3(c, d) and (e, f) for the samples $x = 0.2$ and $x = 0.8$, respectively, show these plane sets in magnified view. The spacing between the planes is determined using ImageJ software,

and we find the *d*–spacings of 0.43 and 0.32 nm for the (-1,1,1) and (1,2,0) planes in the $P2_1/n$ phase for the $x = 0.2$ sample, and 0.28 and 0.31 nm for the (0,0,4) and (1,1,2) planes in the $I4_1/a$ phase for the $x = 0.8$ sample. However, these planes only correspond to the dominating phase of the mixed-phase samples. The selected area electron diffraction (SAED) patterns in Figures 3.3(g, h) indicate the contributions from both the phases. The indexed (*h,k,l*) planes that relate to $P2_1/n$ are coloured in white and yellow colour is designated to the $I4_1/a$ space group, as marked in Figures 3.3(g, h). We find that the analysis of HR-TEM and SAED results is consistent with the XRD refinement data for these samples, as presented in Figure 3.1(b, e).

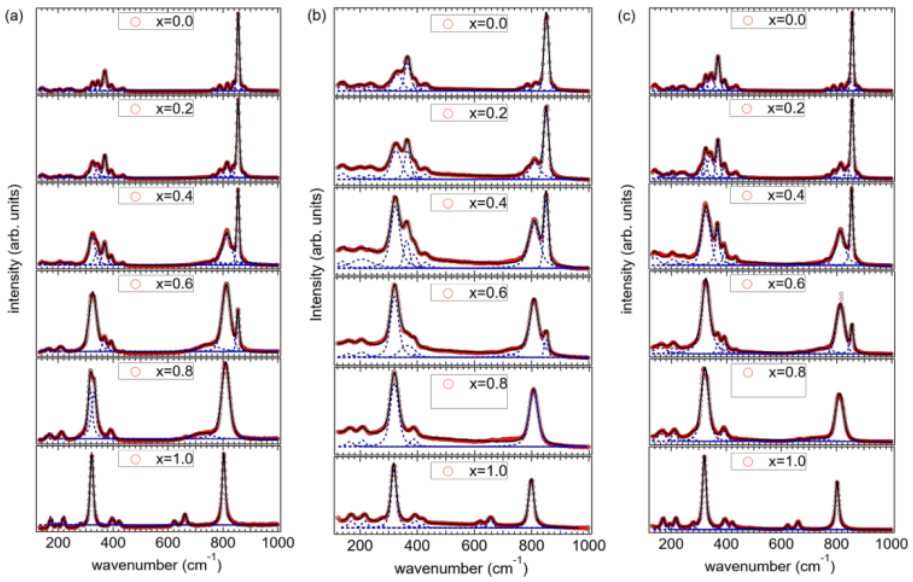


Fig. 3.4: The room temperature Raman spectra of $LaV_{1-x}Nb_xO_4$ ($x = 0$ to 1) samples using (a) 532 nm, (b) 633 nm, and (c) 785 nm excitation wavelengths. The dotted blue lines represent the Lorentzian line shape to deconvolute the individual modes.

The Raman spectra of $LaV_{1-x}Nb_xO_4$ measured at three different excitation wavelengths, 532 nm, 633 nm, and 785 nm are presented in Figure 3.4 for all the samples ($x = 0$–1). Three different excitation wavelengths are used to distinguish the fluorescence effect on the Raman signal and to avoid the background effects from the sample. We use Lorentzian line shape function to deconvolute and fit the observed individual Raman peaks, as marked in Table 3.1. We find that all the specific Raman peak positions (Raman shift) are

independent of excitation wavelength for a sample, which confirm their inherent characteristic of that particular sample, as shown in Figure 3.4.

Table 3.1: The Rietveld refinement parameters of polycrystalline $LaV_{1-x}Nb_xO_4$ (x = 0–1) samples with Nb substitution induced metastable tetragonal–scheelite phase for the x = 0.2 to 0.8 samples, determined using the FullProf software.

x	$\chi 2$	Space Group	a (˚A)	b (˚A)	c (˚A)	β(°)	Volume (˚A^3)
0	1.09	$P2_1/n$	7.042(3)	7.276(4)	6.724(7)	104.88 (6)	333.033(5)
0.2	2.63	$P2_1/n$ - 84%	7.046(1)	7.278(2)	6.733(3)	104.91(1)	333.685(4)
		$I4_1/a$ - 16%	5.336(1)	5.336(1)	11.731(2)	90	334.042(4)
0.4	2.46	$P2_1/n$ - 78%	7.043(0)	7.276(3)	6.732(4)	104.91(2)	333.397(3)
		$I4_1/a$ - 22%	5.332(3)	5.332(3)	11.735(2)	90	333.509(6)
0.6	3.70	$P2_1/n$ - 45%	6.818(9)	7.596(5)	8.030(0)	105.21(7)	401.383(6)
		$I4_1/a$ - 55%	5.329(8)	5.329(8)	11.714(8)	90	332.787(0)
0.8	4.31	$P2_1/n$ - 4%	6.878(5)	7.459(4)	7.679(8)	105.61(1)	379.517(2)
		$I4_1/a$ - 96%	5.375(4)	5.375(42)	11.624(0)	90	335.869(7)
1	4.91	I2/a	5.558(5)	11.529(1)	5.201(8)	93.99(2)	332.546(3)

The intensity of the modes may vary due to several reasons like the polarizability of the molecule, excitation wavelength of the laser source, and the concentration of the active group [34]. Though there are minor changes in the intensity variation of Raman modes measured with different excitation wavelengths, we can see that Raman active peaks are changing systematically for all the measured samples in Figure 3.4.

In the measured spectra we see 20 peaks corresponding to $LaVO_4$ and 17 peaks for $LaNbO_4$. According to the Group theory calculations $LaVO_4$ contains 72 vibrational modes and out of them, 36 modes are Raman active modes ($18A_g + 18B_g$) [35–37] (here, A and B denote symmetric and antisymmetric vibrations about the principal axis of symmetry and subscripts g indicates that the vibrations are symmetric relative to a symmetry centre, respectively). All the 20 Raman peaks for the x = 0 sample are represented from S_0 to S_{19}, as shown in the Table 3.2. The theoretical approach predicted that the $8A_g+10B_g$ modes are for $m - f$ structure, and 13 Raman-active modes in $t - s$ structure (as observed in the x = 0.6 sample), which are summarized in Table 3.2. The

reason for the absence of some of the peaks could be due to the overlap of several A_g and B_g modes and their low Raman scattering cross-section. All the assignments related to each Raman peak in $LaV_{1-x}Nb_xO_4$ are summarised in Table 3.3. We can see in Table 3.2 that the S_0 mode (127.24 cm^{-1}) is present only in $LaVO_4$ and $LaNbO_4$ samples and absent for rest of the intermediate samples. The reason for origin of S_0 mode is translational motion of La atoms in the monoclinic phase. All the concentrations from $x = 0.2$ to 0.8 in $LaV_{1-x}Nb_xO_4$ results in the formation of $t - s$ type structure or $m - m$ and $t - s$ in equilibrium type structure. So, the formation of mixed phase may result in the disappearance of S_0 mode. The S_{18} is the most intense mode for the $LaVO_4$ sample, which decreases with Nb substitution. Whereas, we find that the intensity of S_{16} mode increases with Nb substitution and the same becomes the most intense mode for the $LaNbO_4$ sample, as can be seen in Figure 3.4(a). For the $x = 0.8$ sample, the S_{18} mode completely disappears, which indicates that crystal phase transformation from a mixed phase of $m - m$ and $t - s$ in equilibrium to turning into an approximately pure (96%) $t - s$ phase [38]. This behaviour of S_0, S_{16} and S_{18} corroborate with the structural phase transformation with Nb^{+5} substitution, as has been observed in XRD analysis. Furthermore, the presence of S_8, S_9, S_{10}, S_{13}, S_{14}, S_{15}, S_{17} and S_{18} modes in the $x = 0$ sample confirms the existence of VO_4^{3-} ions since none of these modes are visible in $LaNbO_4$ [39–42].

All the Raman peaks arise due to different vibrational modes, i.e., bonds between different constituent elements, i.e., the La^{3+}, V^{5+}, Nb^{5+} and O^{2-}. The comparison of experimentally observed peak positions of distinct Raman modes, fitted using Lorentzian function, with the reported data [9, 35, 43–45], shows a high degree of similarity, as presented in Table 3.2. In the $m - m$ structured $LaVO_4$ crystal, nine O^{2-} atoms are linked to La^{3+} whereas four O^{2-} atoms and V^{5+} are joined in a tetrahedral shape. There are four different O^{2-} locations and it is bound in a 3-coordinate geometry to two equivalent La^{3+} and one equivalent V^{5+} atoms at the first site. Also, it is bound to two comparable La^{3+} and one equivalent V^{5+} atoms in a deformed single-bond geometry in the second site. Three comparable La^{3+} and one equivalent V^{5+} atoms are linked to O^{2-} in a 3-coordinate geometry at the third O^{2-} site and it is bound in a deformed single-bond geometry to three equivalent La^{3+} and one equivalent V^{5+} atom in the fourth O^{2-} site [46]. In the $m - f$ structured $LaNbO_4$ crystal, the La^{3+} is joined to eight O^{2-} atoms in an 8-coordinate

geometry and six O^{2-} atoms are bound to Nb^{5+} to create the deformed, edge-sharing NbO_6 tetrahedra. There are two different sites for O^{2-} and it is linked in a 4-coordinate geometry to two equivalent La^{3+} and two equivalent Nb^{5+} atoms at the first O^{2-} site. Also, it is bound in a 3-coordinate geometry to two equivalent La^{3+} and one Nb^{5+} atoms at the second O^{2-} site. In the analysis of vibrational modes, it has been assumed that the $LaNbO_4$ crystal is made up of La^{3+} cations and $NbO^3{}_4^-$ molecular anions [43, 46]. It is revealed experimentally that on the addition of Nb^{5+}, it replaces V^{5+} from its site and distorts $LaVO_4$'s unit cell [30]. The mode of vibrations for $LaVO_4$ is categorised as follows: (I) the zone of high wavenumber (765–874 cm^{-1}) resulting from O-V-O bond's stretching vibration (II) the intermediate (305–436 cm^{-1}) region resulting from O-V-O bond's bending vibration, and (III) the zone of low wavenumber (< 285 cm^{-1}) resulting from La atom's translation modes as the La atoms have high mass [9, 17], and the results are presented in Table 3.3. Similarly, the vibrational modes of $LaNbO_4$ are also categorized as follows: (I) high wavenumber zone (623– 803 cm^{-1}) for stretching modes of Nb-O bonds, (II) intermediate zone (322–422 cm^{-1}) for deformation/scissor modes of $NbO^3{}_4^-$, and (III) low wavenumber zone (121– 282 cm^{-1}) for rotational modes of $NbO^3{}_4^-$ and translational lattice modes that include the relative translations of anions and cations [43].

Table 3.2: The experimentally observed frequencies ω_{obs} of the individual Raman modes in $LaV_{1-x}Nb_xO_4$ (x = 0–1) samples measured at room temperature.

x	**0**	**0.2**	**0.4**	**0.6**	**0.8**	**1**
Peak	ω_{obs}	ω_{obs}	ω_{obs}	ω_{obs}	ω_{obs}	ω_{obs}
S_0	B_g(127.24)					B_g(121.86)
S_1	A_g(141.99)	A_g(140.66)	A_g(140.66)	A_g(140.66)		
S_2	B_g(154.05)	B_g(155.39)	B_g(152.71)			
S_3	A_g(187.44)	A_g(187.44)	A_g(186.11)			
S_4	B_g(206.07)	B_g(206.07)	B_g(206.079)	B_g(207.40)	B_g(211.39)	A_g(219.35)
S_5	A_g(235.26)	A_g(233.94)	A_g(233.94)			
S_6	A_g(245.84)	A_g(244.52)	A_g(244.52)			
S_7	B_g(305.11)	B_g(305.11)				
S_8	A_g(326.07)	A_g(326.07)	A_g(326.07)	A_g(324.76)	A_g(328.69)	
S_9	A_g(344.36)	A_g(344.36)	A_g(344.36)			

x	**0**	**0.2**	**0.4**	**0.6**	**0.8**	**1**
Peak	ω_{obs}	ω_{obs}	ω_{obs}	ω_{obs}	ω_{obs}	ω_{obs}
S10	A_g(370.41)	A_g(370.41)	A_g(369.11)	A_g(369.11)		
S11	B_g(393.78)	B_g(393.78)	B_g(391.19)	A_g(391.19)	A_g(388.60)	B_g(396.38)
S12	A_g(420.96)	A_g(418.37)	A_g(418.37)			
S13	B_g(436.44)	B_g(435.15)	B_g(433.86)	B_g(436.44)		
S14	A_g(765.31)	A_g(765.31)	A_g(766.54)	A_g(766.54)		
S15	B_g(788.68)	B_g(788.68)	B_g(788.68)	B_g(788.68)		
S16	A_g(816.86)	A_g(815.63)	A_g(814.41)	A_g(811.96)	A_g(807.07)	A_g(803.39)
S17	A_g(840.06)	A_g(840.06)	A_g(840.06)	A_g(840.06)		
S18	B_g(855.88)	B_g(855.88)	B_g(854.67)	B_g(854.67)		
S19	B_g(874.10)	B_g(874.10)	B_g(874.10)			
S20				A_g(170.10)	A_g(168.76)	A_g(174.10)
S21 S22					A_g(108.41)	A_g(105.72)
S23						B_g(164.75)
S24						B_g(198.09)
S25						B_g(282.77)
S26					B_g(316.91)	A_g(322.14)
S27						A_g(331.30)
S28					A_g(345.67)	B_g(343.06)
S29						B_g(405.44)
S30						A_g(422.25)
S31						B_g(623.49)
S32						A_g(648.58)
S33				B_g(669.83)	B_g(661.08)	B_g(661.08)

Table 3.3: Summary of all the 34 Raman active modes and their assignments with the help of literature (cited in the last coloum of the table) for the $LaVO_4$ and $LaNbO_4$ samples.

Peak	$LaVO_4$		$LaNbO_4$		Refs.
	ω_{th}	Assignments	ω_{th}	Assignments	
S_0	B_g(127)	Translation mode of La atoms in monoclinic phase	B_g(125.1)	Coupled translation-rotational mode of La atoms in monoclinic phase and NbO_4^{3-} around an axis perpendicular to b-axis	[19, 43, 45]
S_1	A_g(143)	Translation mode of La–O bonds			[45, 47]
S_2	B_g(158)	Translation mode of La–O bonds			[47]
S_3	A_g(188)	Translation mode of La–O bonds			[45, 47]
S_4	B_g(204)	Translation mode of La–O bonds	A_g(222.3)	Translational mode of La–O bonds along b-axis	[43, 48]
S_5	A_g(230)	Translation mode of La–O bonds			[47]
S_6	A_g(252)	Translation mode of La–O bonds			[45, 47]
S_7	B_g(316)	Bending vibration of O–V–O bonds			[45, 49]
S_8	A_g(336)	Bending vibration of O–V–O bonds			[45, 49]
S_9	A_g(355)	Bending vibration of O–V–O bonds			[45, 49]
S10	A_g(380)	Bending vibration of O–V–O bonds			[45, 49]
S11	B_g(389)	Bending vibration of O–V–O bonds	B_g(398.1)	Triply degenerate deformation mode (Rocking mode of NbO_4^{3-})	[43, 45, 49]
S12	A_g(423)	Bending vibration of O–V–O bonds			[45, 49]
S13	B_g(427)	Bending vibration of O–V–O bonds			[45, 49]
S14	A_g(784)	Stretching vibration of V–O bonds			[50]
S15	B_g(799)	Stretching vibration of V–O bonds			[50]

Peak	$LaVO_4$		$LaNbO_4$		Refs.
	ω_{th}	Assignments	ω_{th}	Assignments	
S16	A_g(806)	Stretching vibration of V–O bonds	A_g(805.2)	Non degenerate Stretching mode of Nb–O bonds	[43, 50–52]
S17	A_g(836)	Stretching vibration of V–O bonds			[50]
S18	A_g(861)	Non degenerate stretching mode of shortest V–O bonds			[45, 50]
S19	B_g(892)	Stretching vibration of O–V–O bonds			[45, 51, 52]
S20			A_g(177.1)	Translational mode along b axis	[43]
S21			B_g(114)	Rotational mode of NbO_4^{3-} along an axis perpendicular to b-axis	[43]
S22			A_g(108.6)	Rotational mode of NbO_4^{3-} along b-axis	[43, 48]
S23			B_g(170)	Translational mode parallel to ac-plane	[43]
S24			B_g(200.2)	Translational mode parallel to ac-plane	[43]
S25			B_g(284.9)	Translational mode parallel to ac-plane	[43]
S26			A_g(321.7)	Doubly degenerate scissors mode of NbO_4^{3-})	[43, 48]
S27			A_g(326.9)	Doubly degenerate scissors mode of NbO_4^{3-})	[43, 48]
S28			B_g(344)	Translational mode parallel to ac-plane	[43]
S29			B_g(404.9)	Triply degenerate deformation mode (Rocking mode of NbO_4^{3-})	[43]
S30			A_g(425.8)	Triply degenerate deformation mode (Twist mode of NbO_4^{3-})	[43]
S31			B_g(625.5)	One of triply degenerate Stretching mode of Nb–O bonds	[43, 48, 51]
S32			A_g(649)	One of triply degenerate Stretching mode of Nb–O bonds	[43, 48, 51]

Peak	$LaVO_4$		$LaNbO_4$		Refs.
	ω_{th}	Assignments	ω_{th}	Assignments	
S33			B_g(664.9)	One of triply degenerate Stretching mode of Nb-O bonds	[43, 48, 51]

The $LaNbO_4$ contains a total of three different modes: rotational modes of $NbO^{3}{}_{4}^{-}$, vibrational modes of $NbO^{3}{}_{4}^{-}$ and translation modes of La–O and O–La–O bonds. The S_0, and S_{22} peaks are visible corresponding to the combined translation-rotational (B_g) and rotational mode (A_g), respectively, while the third rotational B_g mode (S_{21}) is absent in the observed experimental Raman spectra. The vibrational modes can be categorized into (I) doubly degenerated scissor modes, (II) triply degenerated deformation mode, which further splits into a pair of degenerated rocking mode and one twist mode, (III) stretching mode, a non-degenerate and a triply degenerated with increasing order of wave number [43]. The remaining modes are all translational modes. From the Table 3.3, we can easily identify that $LaNbO_4$ Raman modes are matching well with the reported one. Two $NbO^{3}{}_{4}^{-}$ scissor modes with almost degenerated wave numbers are projected to be seen in the A_g spectrum. Out of all, the most obvious choices are S_{26} and S_{27} because the remaining A_g band's wavenumbers are too low to allocate them. In the $LaNbO_4$, as already discussed, the deformation modes are believed to be divided into two almost degenerated rocking modes (S_{11} and S_{29}) with B_g symmetry and a twist mode (S_{30}) with A_g symmetry. These modes are also present in the region of intermediate wave numbers. The stretching modes are high energy vibrations and here they are recognised as S_{16}, S_{31}, S_{32} and S_{33} peaks. As the non-degenerate symmetric mode is expected to provide the strongest band, band S_{16} is allocated to it. The remaining S_{31}, S_{32}, and S_{33} peaks are assigned to other three degenerate stretching modes. The invariance of the S_4, S_{11} and S_{16} peak positions, all through, from the $x = 0$ to 1 sample indicates no effect on translational mode along the *b*–axis, the B_g frequency of VO_4^{3-} and NbO_4^{3-} for rocking and stretching modes. The S_8 peak disappears only in $LaNbO_4$ spectrum because of absence of O-V-O bending vibrations [17, 43]. Interestingly, the S_2, S_3, S_5, S_6, S_9, S_{12} and S_{19} peaks vanished just before Nb concentration exceeds V (at x =0.4) and also S_1, S_{10}, S_{13}, S_{14}, S_{15}, S_{16}, S_{17} and S_{18} peaks vanished just after Nb concentration became more than V. It is quite possible that the low concentration of Nb in the sample results in the weakening and then disappearance of some of the spectral peaks. Due to the same reason some new peaks (S_{20} and S_{33}) appeared in x = 0.6–1 sample. Furthermore, the S_{20} peak arises due to translational mode along the *b*–axis, and S_{33} peak appeared due to one of three triply degenerate stretching modes of NbO_4^{3-} in the sample.

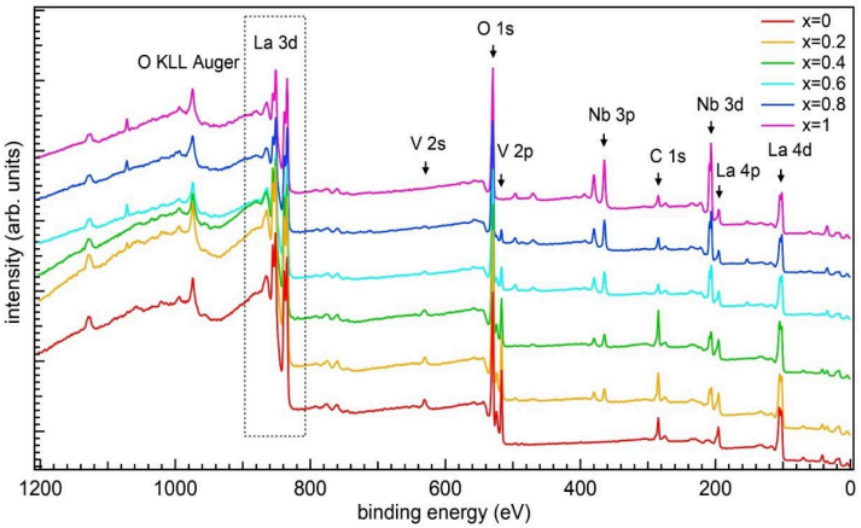


Fig. 3.5: The room temperature XPS survey spectra of $LaV_{1-x}Nb_xO_4$ (x = 0 to 1) samples.

The most intense peak in $LaNbO_4$ (S_{16}) and $LaVO_4$ (S_{18}) at higher wavenumber is due to the stretching of Nb-O_t and V-O_t bonds, where O_t represents the oxygen atoms in the terminal position [53]. The terminal position of oxygen is that where it connects the LaO_8 dodecahedra and NbO_6 octahedra in case of $LaNbO_4$ and LaO_9 muffin [54] and VO_4 tetrahedra in case of $LaVO_4$ [53]. Since the VO_4 tetrahedra appears to be intrinsic in the peak broadening, it has been found that this broadening in the Raman peaks spreads along samples with intermediate Nb and V compositions. However, in certain samples, Nb^{5+} and V^{5+} cation- related variables may also play an important role in the increasing the broadening of the peak. The broad peaks are made up of multiple modes which are normally difficult to distinguish from one another [53]. The strongest peak of $LaVO_4$ (S_{18}) is in the high wavenumber region which lies approximately 52.5 cm^{-1} on higher side of the spectrum with respect to the strongest peak of $LaNbO_4$ (S_{16}). This difference in wavenumber (Δ) is related to average bond length (d) of the atoms by $\Delta \propto 1/d^{3/2}$, as stated by the Badger rule [55]. The bond lengths V–O_t in $LaVO_4$ and Nb–O_t in $LaNbO_4$ is ~1.72 ˚A [9] and ~1.90 ˚A [53], respectively. The changes observed in the Raman spectra of the samples is quite consistent with the Badger's rule.

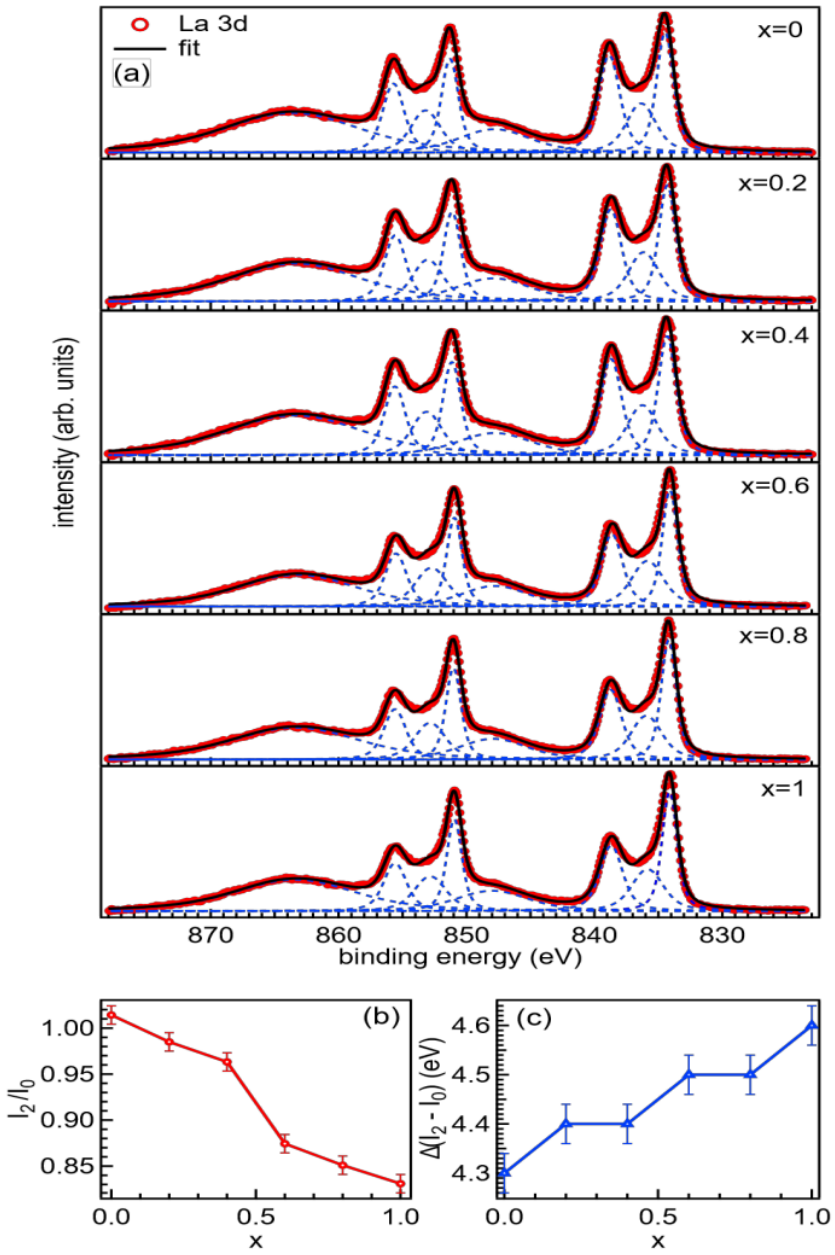


Fig. 3.6: (a) The La 3*d* core-level spectra of $LaV_{1-x}Nb_xO_4$, x = 0–1 sample. (b) The intensity ratio I_2/I_0, and (c) energy separation I_2 - I_0 as a function of doping level x. The fitted spin-orbit split components are also shown for each sample.

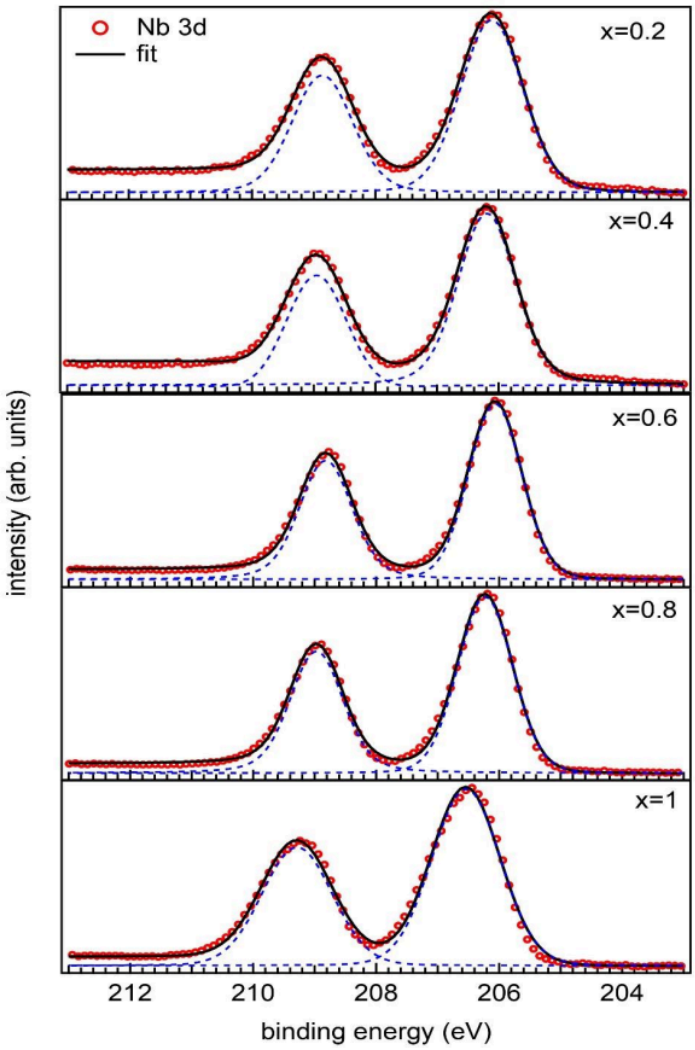


Fig. 3.7: The Nb 3*d* core level spectra of $LaV_{1-x}Nb_xO_4$, x = 0–1 sample. The fitted spin-orbit split components are also shown for each sample.

Finally, we use x-ray photoemission spectroscopy (XPS) to investigate the electronic structure by measuring the survey scan and particular elemental core-level spectra of all the prepared samples. The identified peaks in the survey spectra according to their binding energies are labelled and are in agreement with reported values, as shown in Figure 3.5. The characteristic La 3*d* peaks cluster (830–870 eV), 4*d* ($4d_{5/2}$ at 101 eV and $4d_{3/2}$ at 104 eV), and 4*p* (centred around 195 eV) [56]. The presence of these peaks of La

is clearly visible for every synthesised sample, and they are all remarkably comparable. A consistent rise in Nb 3*d* (discussed later) and Nb 3*p* ($3p_{3/2}$ at 364 eV and $3p_{1/2}$ at 379 eV) is observed along with an increase in Nb doping and this feature of Nb is absent in the $x = 0$ sample [57]. For the V 2*p* ($2p_{3/2}$ at 517 eV and $2p_{1/2}$ at 525 eV) and V 2*s* (630 eV) core level peaks, the reverse behaviour is anticipated, and it is quite evident as clearly visible in Figure 3.5 [58]. The Voigt function has been used to fit the core level spectra of the constituent elements. The fitted La 3*d* core-levels are shown in Figure 3.6(a). The spin-orbit splitting peaks present in all the samples, have been de-convoluted at binding energies 834.3±0.2 eV, 836.0±0.3 eV, 838.7±0.1 eV, 847.9±0.1 eV, 851.1±0.2 eV, 853.0±0.3 eV, 855.6±0.1 eV, and 863.4±0.2 eV (average B.E. of all the samples ± ΔB.E., calculated for the $x = 0$–1 samples). The broad diffusive satellite peaks at 847.7 eV and 863 eV in the locality of La 3*d* core-level are coming from plasmons. Because of the two final states I and II, and the subsequent spin-orbit splitting between each state, making the structure complex. The primary strong peaks ($3d_{5/2}$ at 834.3 eV and $3d_{3/2}$ at 851.1 eV, respectively) are associated with the final state I (La^{4+} $3d^9 4f^0$, L), which involves electron transfer to the continuum from the 3*d* core-level. The peaks at higher binding energies are features of final state II (La^{3+} $3d^9 4f^1$, L, -e) and this feature is experimentally unresolved which indicates multiple structure, as has been suggested by Mullica *et al.* [56]. This corresponds to the electron transfer from ligand (L, O_{2p} in our case) valance band to the empty 4*f* orbitals of La [56, 59]. This multiple structure of state II is composed of two bonding and anti-bonding states. The prominent signals at higher binding energies ($3d_{5/2}$ at 838.7 eV and $3d_{3/2}$ at 855.6 eV) are due to bonding of state II and the weak signals at lower binding energies ($3d_{5/2}$ at 836.0 eV and $3d_{3/2}$ at 853 eV) are because of anti-bonding. The average energy difference (over La core-level spectra of all the samples) between these three pairs of peaks is nearly the same (16.9 eV) for the state I, state II bonding, and state II anti-bonding, respectively. This verifies the unaltered spin-orbit energy splitting of the states of La on Nb substitution [60]. Interestingly, we find a significant and systematic change in the intensity variation of the peak at 838.7 eV (I_2) relative to the primary peak at 834.3 eV (I_0) with Nb doping. The metal-ligand orbital overlaps are reported to be accountable for such doping-induced intensity variations [61, 62] where strong ligands are found to populate the ($La^{3+}3d^9 4f^1$, L, -e) state, intensifying I_2 [63]. The intensity ratio I_2/I_0 is shown in Figure 3.7(b), which shows a consistent decrease as a function of doping *x*. This signifies that with Nb substitution, the extent of overlapping between La(4f)-O(2p) orbitals decreases monotonically. This conclusion can

also be drawn from the trend in the energy separation between I_2 and I_0 as a function of x, as shown in Figure 3.6(c). However, the separation is minute in the subsequent samples, but for the $x = 0$ and $x = 1$ the energy difference (I_2 - I_0) is found to be of the order of 0.3 eV. The value of I_2 - I_0 was found to be varying for a variety of La-containing compounds majorly because of the crystal structure, like 3.8 eV for $La_{0.5}Sr_{0.5}Co_{1-x}Nb_xO_3$ and 5.3 eV $La_{1.85}Ba_{0.15}CuO_4$ [60, 62]. Notably, this energy separation could be related to the ease of electron transfer between the ligand and the more ionic state of La, therefore having an opposite trend with the tendency of ligand's overlapping with the La 4*f* orbitals [62].

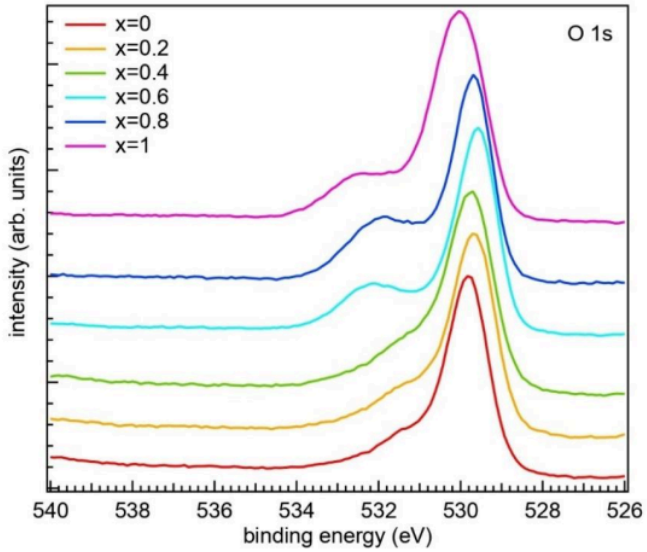


Fig. 3.8: The O 1*s* core level spectra of $LaV_{1-x}Nb_xO_4$, $x = 0$– 1 sample. Each spectrum is shifted vertically for the clarity.

The Nb 3*d* core level spectra are shown in Figure 3.7 where the spin-orbit doublet of Nb 3*d* core levels are fitted with a single peak for each component and the calculated peak positions for the Nb-doped samples are found to be $3d_{5/2}$ at 206.2±0.2 eV and $3d_{3/2}$ at 209.0±0.2 eV [64, 65]. This confirms the presence of prevailed 5+ oxidation state of Nb atom [57] in all the samples. However, for the $x = 1$ sample the Nb $3d_{5/2}$ is at a higher binding energy as compared to the other Nb-containing samples, which could be due to the charging effects and the change in chemical environments. Therefore, Atuchin *et al.* characterized the Nb state by using energy difference Δ (Nb $3d_{5/2}$ – O 1*s*) instead of solely relying on Nb $3d_{5/2}$ binding energy position [66]. The evaluated Δ (Nb $3d_{5/2}$ – O 1s) values

are found to be around 323.5 eV. The calculated energy difference with respect to O 1*s* is independent of the carbon correction. The obtained binding energy difference ≈323.5 eV is reported to be a fairly highest value for the 5+ oxidation state of Nb. We can also see that the error in the value of binding energy position Δ is only 0.1 eV in this case, while for the Nb $3d_{5/2}$, and O 1*s*, it is 0.3, and 0.2 eV, respectively. In Figure 3.8 we can also see that the O 1*s* peak is shifting to higher binding energy for the $x = 1$ sample as compared to the $x = 0$. Similarly, for the Nb $3d_{5/2}$ core-level, it is shifting to higher binding energy. The Δ(Nb $3d_{5/2}$ - O 1s) value for the $x = 1$ sample is quite consistent for all the samples, which strongly supports the electronic characterization using energy difference with respect to O 1*s* instead of absolute peak positions.

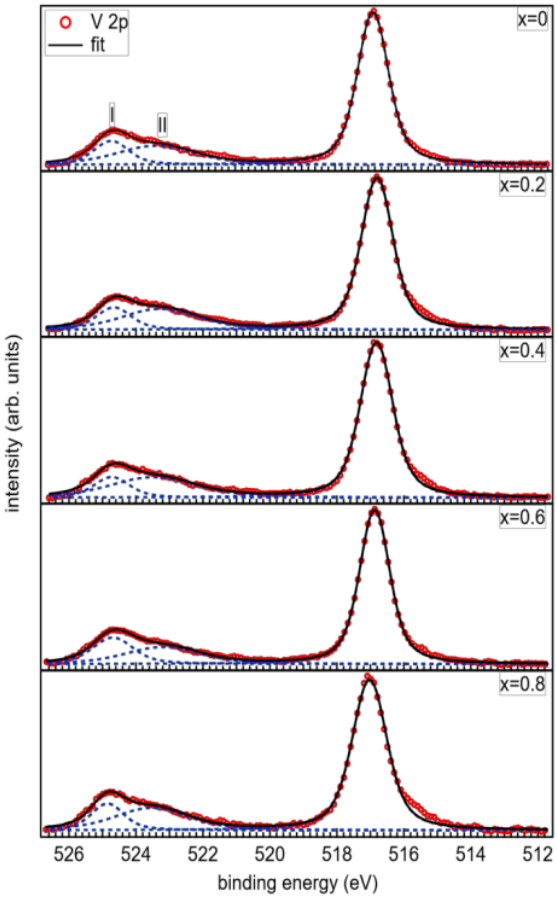


Fig. 3.9: The V 2*p* core level spectra of $LaV_{1-x}Nb_xO_4$, $x = 0–1$ sample. The fitted spin-orbit split components are also shown for each sample.

In Figure 3.9, we present the V 2*p* core level spectra for all the samples, which shows spin orbit components of $2p_{3/2}$, and $2p_{1/2}$ at 516.9 and 524.8 eV, respectively indicating V in 5+ state. Interestingly, an unusual broadening in the V $2p_{1/2}$ component is observed for all the samples, whereas no such additional component is evident in the V $2p_{3/2}$ peak at 516.9 eV. More importantly, the deconvolution of the V $2p_{1/2}$ component reveals that the FWHM of the higher energy feature (denoted by I) (1.2 eV) is nearly the same as that of $2p_{3/2}$ component (1.1 eV). In contrast, the lower energy feature (II) is significantly broader (2.8 eV). Moreover, the area ratio of the combined I and II with $2p_{3/2}$ is close to 1/2, which clearly indicates the intrinsic origin of these two features from the vanadium. In contrast to metallic V 2*p* core-level, the vanadium-based compounds have often been reported to exhibit an anomalous V $2p_{1/2}$ width as a consequence of Coster-Kronig (C-K) transitions [67]. The C-K type transition is a class of Auger transition in which an electron from a higher sub-shell of the same shell fills the core hole [68]. In the present case, the filling of $2p_{1/2}$ core hole by an electron from $2p_{3/2}$ may give rise to the C-K transitions and that can result in an additional feature in the $2p_{1/2}$ component. Therefore, it is likely that the component I is attributed to the core-hole recombination with the screening electrons, analogous to the $2p_{3/2}$, whereas an additional L_2-L_3 (C-K) relaxation process gives rise to the feature II in $2p_{1/2}$ peak [69]. No significant change in these components has been observed with the Nb substitution, indicating the robust nature of the underlined system. Further, the approach of O 1*s* energy difference is also implemented in this case as for vanadium oxides, the energy difference Δ(V $2p_{3/2}$ - O 1s) is an advantageous reference [70]. The average Δ (V $2p_{3/2}$ - O 1s) magnitude is 12.8∓0.1 eV, which is in good agreement with the literature for V^{5+} oxidation state [71].

3.4 Conclusions

In conclusion, the solid-state reaction method was used to prepare $LaV_{1-x}Nb_xO_4$ samples successfully with regular variable Nb^{5+} concentration. The XRD measurements established that the substitution of larger Nb^{5+} ion for V^{5+} affects the lattice constant of $LaV_{1-x}Nb_xO_4$ and goes through three different phase transformations [monoclinic monazite ($m - m$) type ($x = 0$), two-phase equilibrium of monoclinic monazite ($m - m$) and tetragonal scheelite ($t - s$) type ($0.2 \leq x \leq 0.8$) and monoclinic fergusonite ($m - f$) type

($x = 1$)]. The SEM micrographs helped in analysing that the particle size and shape altered due to the change in crystal phases of these samples with increasing Nb^{5+} concentration. The analysis of HR-TEM and SAED data found to be consistent with the XRD refinement data. The Raman spectra of $LaV_{1-x}Nb_xO_4$ were studied using 532 nm, 633 nm, and 785 nm excitation wavelengths. All the Raman assignments were found to have well-ordered enhancement/diminution with the increase in Nb^{5+} doping. The variation in the intensity as well as appearance/disappearance of the Raman mode with Nb concentration are coinciding with the change in the structural phases, as observed in XRD analysis. This further confirms that the phase transformation in $LaV_{1-x}Nb_xO_4$ agrees with the maximum intensity peak patterns shown in the Raman spectra of these samples and are consistent with the Badger's rule. The XPS analysis reveal the changes in Nb 3*d* and V 2*p* core-level spectral intensities of the samples with the increase in Nb^{5+} concentration. The equal spin-orbit energy splitting of the states was confirmed by the average energy difference (over La core spectra of all samples) for state I, state II bonding, and state II anti-bonding and the observed changes in their relative intensities with Nb substitution are due to the metal ligand orbitals overlap. These findings provide valuable insights into the structural and electronic properties of $LaV_{1-x}Nb_xO_4$ samples and their potential use in different fields of practical applications.

Chapter 4

Dielectric Behaviour and Impedance Spectroscopy of Niobium Substituted Lanthanum based Orthovanadates at High Temperatures

In this chapter, we present the detailed study of the temperature dependent dielectric properties, impedance spectroscopy and electrical conductivity of $LaV_{1-x}Nb_xO_4$ (x = 0–1) samples prepared by the solid-state reaction method. The dielectric constant (ε_r') increases (decreases) with increase in the temperature (frequency); while the magnitude of ε_r' remains almost invariant (order of 10^4 at 100 Hz and 600°C) with x. The single-phase x = 0 (monoclinic-monazite, $P2_1/n$) and x = 1 (monoclinic fergusonite, $I2/a$) samples show the lower values of loss factor [tanδ = (4–8)] as compared to the x = 0–0.8 samples [tanδ = (12–18)] having mixed tetragonal and monoclinic phases, which indicates the strong correlation between the crystal structure and the dielectric properties. The real part of impedance (Z') decreases with both temperature and frequency, and the observed weak relaxation remains almost unaltered with x. The imaginary part of impedance (Z'') shows strong relaxation peaks shifting towards higher temperatures with frequency, which is attributed to the effect of grains, grain boundaries, and electrodes in the samples. The activation energy of the relaxation process is estimated to be 0.8–1.0 eV for the x = 0–0.6 samples, and ≈1.4 eV for the x = 0.8; whereas the x = 1 sample shows two values (≈0.5 eV and ≈1.0 eV) in the higher and lower temperature range, respectively. Further, the change in total conductivity with the angular frequency, which found to be in the range of 10^{-3} to 10^{-5} S/m, is fitted using the Jonsher power law. The analysis suggests the overlapping large polaron tunneling (OLPT) model for all the samples, whereas the x = 1 sample exhibit a transition near 480°C and at higher temperatures it shows non-overlapping small polaron tunneling (NSPT) and quantum mechanical tunneling (QMT). This transition is corroborated by the tangent loss curves and may be associated with the change in structure.

4.1 Introduction

In last few decades, the orthovanadates with general formula RVO_4, where R refers to rare earth elements, have widely attracted the attention of scientific community due to their vast technological applications in catalysts, as luminescent materials, polarizers, and laser host materials [1]. In this family, the $LaVO_4$ is turned out to be particularly important in the recent time because of its use as an electrode material for Lithium-ion batteries (LIBs) as it shows large specific capacity as well as long cyclic life [2]. The $LaVO_4$ crystallises in tetragonal zircon type polymorphs with space group $I4_1/amd$ and monoclinic monazite type polymorphs with space group $P2_1/n$, following the trend of the rare-earth family [3]. However, it also deviates from the trend by thermally stabilizing in the monazite type structure and being metastable at ambient temperatures [3]. This is due to the higher oxygen coordination number in the monazite as compared to zircon type structure and largest ionic radius of La^{3+} in the lanthanide family [4–6]. A pattern of VO_4 tetrahedra with four distinct V–O bonds and RO_8 dodecahedra sharing edges alternately and connected in chains along the *c*-axis can be found in the zircon structure [7]. In the monazite structure, RO_9 polyhedra are linked to deformed VO_4 tetrahedra with four distinct V–O links, sharing their edges [8]. According to the refs. [9] and [10], the Zircon type $LaVO_4$ cannot be synthesized at ambient temperatures using the traditional solid state reaction technique; however, it can be produced and stabilized using the hydrothermal method. The influence of substituting La by another rare earth elements has been significantly explored for the $LaVO_4$ family; however, the doping/substation at the V-site is still in its infancy, as evidenced by the fact that only a handful of studies have been conducted so far [3, 11, 12]. The rare-earth niobate $LaNbO_4$ on the other hand is well-known to show the temperature and chemical pressure (doping) induced structural transformation [13, 14]. The $LaNbO_4$ transforms from the monoclinic fergusonite (space group *I2/a*) structure at the low temperature to the tetragonal scheelite (space group $I4_1/a$) phase above ~495°C [13]. Similarly, it also shows a structural trans-formation on replacing 25% of Nb^{5+} with V^{5+} [14]. Because of its intriguing characteristics, including proton conductivity [15], excellent dielectric, and high energy release using X–ray stimulation [16]and hence wide technological applications in sensors [17], contrast agents, waveguides, ferroelectrics [18], phosphors

[19], laser crystals [20], scintillators [21], luminophores, LEDs, etc., the $LaNbO_4$ is getting a special attention of the scientific community from several decades. Therefore, we choose to replace V by Nb atoms in $LaV_{1-x}Nb_xO_4$, as Nb shares many properties with vanadium and is found right beneath it in the periodic chart, to examine the influence of B-site atoms on the high temperature structural transition and hence the physical properties of these compounds. Though, the vanadium costs have historically lagged behind those of niobium, but it has lately increased by about 300%, which has created strong economic incentives to transition to niobium. The tetrahedrally coordinated niobium has bigger ionic radius (0.48 Å) and is isoelectronic to the vanadium ion (V^{+5}) [22] and hence most suitable to exert the chemical pressure in the crystal lattice. Further, the nontoxic nature of Nb make it suitable candidate for the industrial applications. Moreover, the La-Nb based perovskite oxides have been also extensively studied due to their important fundamental as well as functional properties [23–29]. Recently, we reported the vibrational, structural as well as electronic properties of the $LaV_{1-x}Nb_xO_4$ (x =0– 1) samples using the x-ray diffraction (XRD), Raman and x-ray photoemission spectroscopy [3]. The x = 0 and 1 samples were found to crystallize in the single phase monoclinic-monazite ($P2_1/n$) and monoclinic fergusonite ($I2/a$) type structures at the room temperature, respectively; whereas the monoclinic-monazite ($P2_1/n$) and tetragonal scheelite ($I4_1/a$) phases coexist in the x = 0.2–0.8 samples and phase fraction of later increases with the Nb substitution [3]. The fact that the $LaNbO_4$ possesses the tetragonal structure when measured at room temperature by substituting about 20% of Nb^{5+} concentration at the V^{5+} site is an important finding, which makes a variety of room-temperature applications possible, as this transformation plays a significant role in regulating the protonic conductivity of $LaNbO_4$ [30]. Moreover, for certain compositions of $LaV_{1-x}Nb_xO_4$, the transition temperature can occur close to room temperature [14]. At x=0.75, for instance, temperature-dependent XRD measurements indicate that $LaV_{1-x}Nb_xO_4$ should possess a tetragonal structure when measured at room temperature, with its transition at around 250 K. Nevertheless, the XRD pattern below this transition also shows minor residual intensity in the form of broadened lines, which may be the effect of precursors [14]. Similarly, the XRD patterns of x=0.8 samples also exhibit broad peaks, likely due to the same effect [14]. Therefore, it is vital to investigate the high temperature phase transition and their

influence on the dielectric and ac impedance spectroscopy with Nb substitution in $LaV_{1-x}Nb_xO_4$ samples. The impedance spectroscopy is widely used to study the electrical properties of materials to understand their various possible applications such as solid oxide fuel cells (SOFCs). One of the advantages of impedance spectroscopy is its ability to provide information about the properties of a material or system over a wide frequency range, typically from a few Hertz to several mega Hertz. This can be particularly useful for studying materials that exhibit complex electrical behaviour, such as those with multiple structural phases or with a distribution of relaxation times [31–34]. Therefore, in this article, our objectives are to comprehensively investigate the temperature dependent conductivity, impedance spectroscopy, and dielectric properties of $LaV_{1-x}Nb_xO_4$ (x = 0–1) samples. These measurements are made of the dielectric constant and tangent loss at temperatures ranging from 25°C to 600°C and in a wide range of frequency (f) from 100 Hz to 1 MHz We demonstrate that the dielectric constant increases with temperature and decreases in magnitude with frequency. The magnitude of the dielectric constant is not significantly changed by the addition of Nb^{5+} in place of V^{5+}, and anomalous behaviour is observed from x = 0.2 to 0.8 due to their mixed states, whereas the x = 0 sample shows no peak and the x = 1 sample shows a weak relaxation in higher temperature range. For the x = 0– 0.8 samples, the tangent loss displays the peaks in the higher temperature range above 360°C, whereas the x = 1 displays a weak relaxation peak, shifting towards higher temperatures. The real component of the impedance (Z') decreases with temperature and frequency, and a weak relaxation is observed in all the samples, which remains almost invariant with x. The imaginary component of impedance (Z'') exhibits prominent relaxation peaks that shift towards higher temperatures with frequency, which further illuminating the influence of the grain, grain boundary, and electrode in the samples. In the Z''–f plots, the behaviour from x = 0 to 0.6 is identical, but the x = 0.8 and 1 samples exhibit a relaxation in the lower frequency area that exhibits both the grain effect and the grain boundary effect. In order to look at the lower frequency components, such as the grain boundary and electrode influence, the modulous spectroscopy is also used. Additionally, the total conductivity is measured with varied frequency in the 360°C–560°C temperature range and fitted with the Jonsher power law. The x = 0.8 sample shows the lowest conductivity, which is related to the largest grain size and highest Nb concentration in

the coexisting phases of these samples. Interestingly, we find the overlapping large polaron tunnelling (OLPT) behaviour for all the samples, whereas the x = 1 sample undergoes non-overlapping small polaron tunnelling (NSPT) and quantum mechanical tunnelling (QMT) behaviour at higher temperatures.

4.2 Experimental

We use the conventional solid state reaction method to prepare the $LaV_{1-x}Nb_xO_4$ (x = 0–1, Δx=0.2) bulk samples. The details of the synthesis process, and their structural and electronic properties can be found in our earlier report [3]. The prepared samples were cold pressed in the form of circular pellets of 10 mm diameter and 1-2 mm thickness at 14 MPa before the final annealing at 1250°C. The pellets were then polished and painted with sliver paste on both the sides for the dielectric measurements. The temperature dependent dielectric measurements and ac impedance spectroscopy were then performed on all the samples using HIOKI 3536 LCR meter from 25°C to 600°C in the large frequency range from 100 Hz to 1 MHz at 1 V excitation voltage, under the vacuum conditions of $\sim 3\times10^{-2}$ mbar. The complex dielectric constant (ε_r'), tangent loss (tanδ), complex electric modulus (M), and ac conductivity are calculated using the temperature dependent complex impedance (Z) and phase angle (θ) measured using the LCR meter. It involves applying a small, alternating voltage to a sample and measuring the resulting current response over a range of frequencies. By analysing the relationship between the current and voltage, the impedance of the sample can be determined. We use the following formulas to calculate various electrical parameters:

$$Z = Z' + iZ'' \tag{1}$$

$$M = i\omega C_0 Z = M' + iM'' \tag{2}$$

where, $Z' = |Z|\ cos\theta$ and $Z'' = |Z|\ sin\theta$ are real and imaginary parts of complex impedance, M′ and M″ are real and imaginary parts of complex electric modulus, $\omega = 2\pi f$ is the angular frequency, C_0 is the capacitance in the vacuum, defined as $C_0 = A\varepsilon_0/d$, where A is the area of electrodes and d is the separation between them.

Using equations (1) and (2), the M′ and M″ can be expressed as:

$$M' = \omega C_0 Z''; \; M'' = \omega C_0 Z' \tag{3}$$

Here, the dielectric constant can be written in terms of the inverse of electric modulus, i.e.

$$\varepsilon_r = \varepsilon_r' + i\varepsilon_r'' = 1/M \tag{4}$$

where the ε_r' and ε_r'' are real and imaginary parts of ε_r, respectively.

Using equations (2), (3) and (4), we get

$$\varepsilon_r' = Z'' / \omega C_0 Z^2; \; \varepsilon_r'' = Z'' / \omega C_0 Z^2 \tag{5}$$

We utilize the above equations to compute the ε_r', Z', Z'', and M'' parameters, as discussed in detail below.

4.3 Results and Discussion

The temperature dependent real part of dielectric constant (ε_r') is presented in Figures 1(a–f) for $LaV_{1-x}Nb_xO_4$ (x = 0–1) samples at the selected frequencies. The dielectric constant of a material determines the amount of electric charge that can be stored in a capacitor made from the material, as well as the strength of the electric field that can be sustained before the material breaks down. For the x = 0 sample, no peak is observed in the measured temperature range and the ε_r' decreases with increase in the frequency [see Figure 4.1(a)]. The ε_r' remains almost temperature independent up to around 300°C and then increases abruptly with further increase in the temperature. The decrease in the ε_r' with frequency is because of the reduction of space charge polarization [35– 38]. The presence of space charge polarization at lower frequency creates a potential barrier which leads to the building-up of charges at the grain boundary, resulting the higher values of]. It is conventional to use the thermal energy to demonstrate the relation between the dielectric constant and the change in the temperature [39]. The mobility of charge carriers and, therefore, their rate of hopping are improved at higher temperatures by the additional thermal energy, which is insufficient at the lower temperatures, causing the observed enhancement in the ε_r' with temperature.

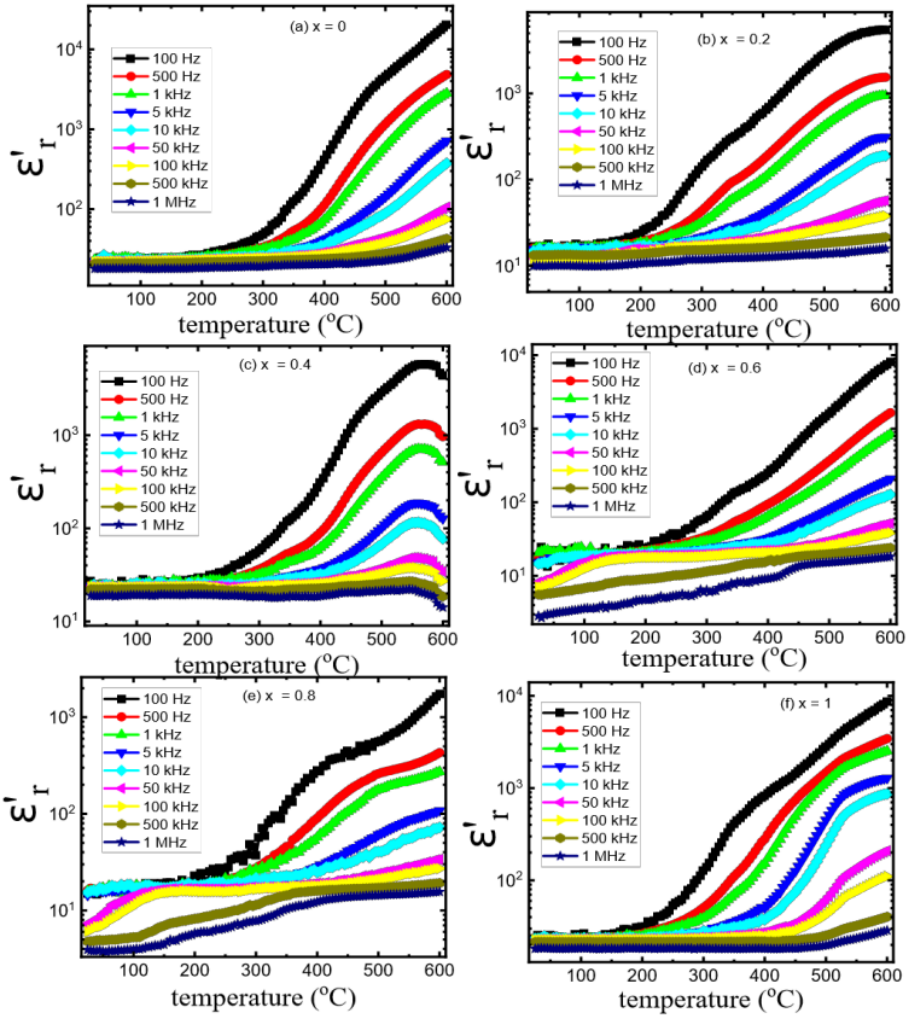


Fig. 4.1: (a–f) The temperature dependent real part of dielectric constant (ε_r') for $LaV_{1-x}Nb_xO_4$ (x = 0–1) samples from 25°C–600°C in the frequency range of 100 Hz–1 MHz.

The dielectric polarization increases with increase in the temperature, which enhances the ε_r' at higher temperatures up to a certain limit, called 'phase transition temperature' and at this temperature the polarization decreases to almost zero, there-fore the ε_r' starts decreasing with temperature [40, 41]. However, no phase transition has been observed for the x=0 sample in the measured temperature range (up to 600°C). Similarly, for the x = 0.2 sample, no peak is observed decrease in the phase transition temperature and hence saturation in the dielectric constant. Moreover, a peak is observed near 550°C

with further increase in the Nb substitution for the x = 0.4 sample [see Figure 4.1(c)], the position of which remains almost invariant with increase in the frequency. Interestingly, for the x =0.6 and 0.8 samples, an additional dielectric relaxation peak is observed at significantly lower temperatures (200–300°C), which shifts to the higher values with increase in the excitation frequencies [see Figure 4.1(d, e)]. The increase in the tetragonal scheelite ($I4_1/a$) phases with the Nb substitution is expected to give rise to this additional relaxation peak in these samples [3]. Moreover, the x = 1 sample shows a similar behavior to the x = 0 [except a weak relaxation around 500°C; see Figure 4.1(f)], which can be attributed to the presence of single phase in both of these samples [3].

To gain a deeper understanding of the material's behavior, we perform detailed analysis of the temperature dependent tangent dielectric loss, represented as $\tan\delta = \varepsilon_r'/\varepsilon_r''$ for all the samples, as shown in Figures 4.2(a– f). Here, we investigate how different samples respond to changes in temperature and excitation frequency by analyzing their tangent dielectric loss, which is a measure of how the material dissipates energy when subjected to an alternating electric field. Note that all the samples in this study exhibit peaks in their tan δ curves, which are a significant indicator of how the material responds to changes with the variation in temperature and excitation frequency. The location of the peak in tanδ shifts to higher temperatures as the excitation frequency increases. This shift implies that with the application of higher frequencies, the material's response to temperature changes at higher temperatures. It is an important behavior to note because it indicates a thermally triggered relaxation process [42]. The magnitude of the peak in tanδ decreases as the excitation frequency increases for most of the samples. This behavior suggests that at higher frequencies, the material's dielectric loss is reduced. However, there is an exception with the sample where x = 1, where the height of the peak in tanδ actually increases with the frequency until it reaches around 100 kHz. After this point, it starts to decrease as the frequency increases further [see Figure 4.2(f)]. It should be noted that the increase in tanδ at higher temperatures is primarily due to the direct current (*dc*) conductivity. In other words, the behavior of the material at high temperatures is influenced significantly by its ability to conduct the electric current. Interestingly, the tanδ values increases with Nb substitution up to x = 0.4 sample and

then start decreasing at higher Nb concentration. It is observed that the samples with single phases (with $x = 0$ and $x = 1$) have lower dielectric loss values compared to those with mixed phases (with $x = 0.2–0.8$). This indicates that the presence of mixed phases affects the dielectric properties of the material. For the samples with mixed phases (specifically, $x = 0.2–0.8$), the interaction between the different phases results in anomalous behavior in the tanδ curves. This anomalous behavior is observed in higher frequencies and lower temperature regimes [3]. It suggests that the combination of different phases introduces complex interactions that affect how the material responds to changes in temperature and excitation frequency. The observed shifts in peak positions, frequency-dependent magnitudes, and differences between single-phase and mixed-phase samples provide insights into the material's electrical properties and its complex behavior under varying conditions. These findings are important for understanding the material's suitability for specific applications and may have implications for the design of electronic devices. From the above analysis and discussion, we reveal that the samples with mixed phases ($x = 0.2–0.8$) exhibit anomalous behavior in their ε_r' and tanδ characteristics. The presence of mixed phases introduces complex interactions that govern how the electric dipoles respond to the change in temperature and excitation frequency. Now, we further delved insight into the investigation by analyzing the impedance (Z) and modulus (M) spectra of all the samples. The aim is to unravel how the grains (individual crystal structures) and grain boundaries (interfaces between these crystal structures) contribute to the observed relaxation processes in theϵ_r'(T) (real part of dielectric permittivity as a function of temperature) and tanδ(T) (tangent of dielectric loss as a function of we observed that the significant and rapid increase in the temperature) spectra. From the temperature-dependent dielectric constant is within the range of 360 °C to 560 data of ε_r' and *tanδ* in the temperature range of 25 to °C. Also, this temperature range exhibited the most pro600°C for all the samples in Figures 4.1 and 4.2, respectively, we observed that the significant and rapid increase in the dielectric constant is within the range of 360°C to 560°C. Also, this temperature range exhibited the most pronounced peaks in the tangent loss for all the samples. Therefore, we focus our analysis solely in this specific temperature range (360 °C to 560 °C) to investigate parameters such as impedance, electric modulus, and conductivity. The approach allows us to gain insights into the

behavior of the grain and the effects on grain boundaries resulting from Nb doping in $LaV_{1-x}Nb_xO_4$. These findings provide valuable information about the electrical properties of the material and how they relate to its microstructure, which is crucial for understandings its potential applications.

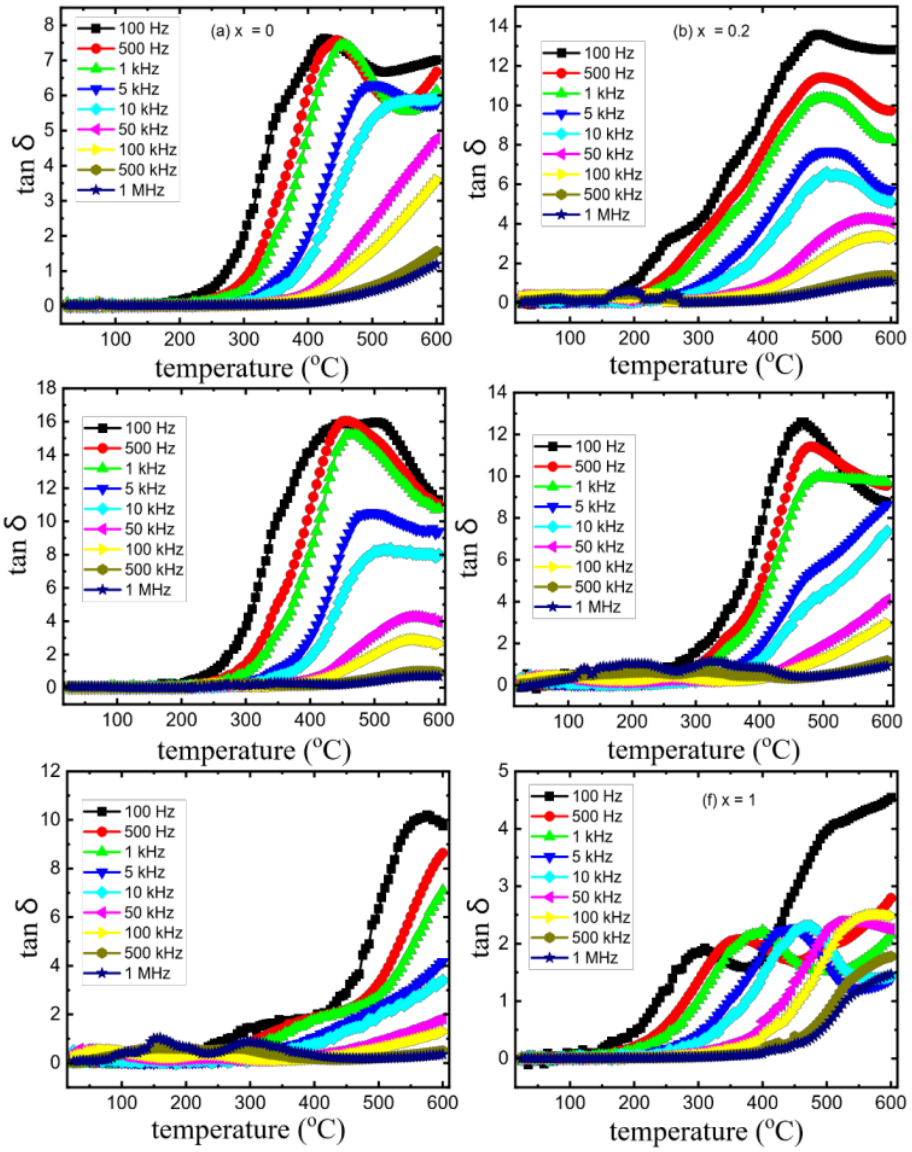


Fig. 4.2: (a–f) The dielectric loss (tan δ) for $LaV_{1-x}Nb_xO_4$ (x = 0–1) samples plotted as a function of temperature at the selected frequencies.

Figure 4.3(a–f) display the real part of impedance (Z') as a function of frequency for all the samples at selected temperatures. The Z' is a measure of the opposition that a material presents to the flow of alternating current. The key observation is that the order of Z' remains nearly constant regardless of the Nb substitution in the samples. However, the value of Z' decreases with increasing temperature for all the samples, which is indicative of the semiconducting or insulating nature of these materials.

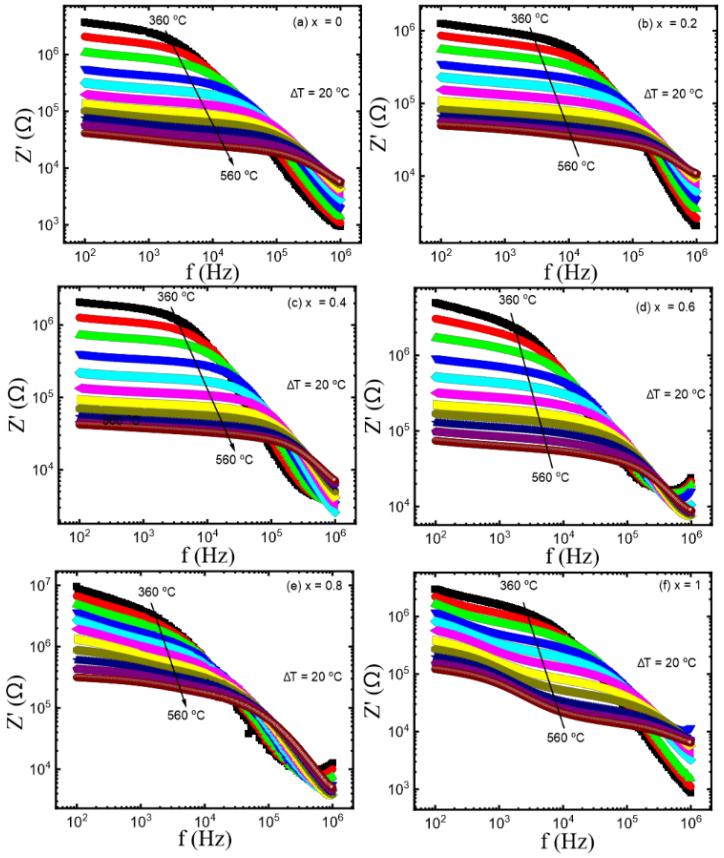


Fig. 4.3: (a–f) The real part of impedance (Z') of $LaV_{1-x}Nb_xO_4$ (x = 0–1) samples plotted as a function of frequency from 100 Hz to 1 MHz at the selected temperature from 360°C–560°C.

In other words, as the temperature rises, the ability of the material to conduct electric current decreases. The impedance behavior can be divided into two regions: (1) frequency-independent region and (2) frequency-dependent region. The first region is associated with *dc* conductivity, which means that the charge carriers (electrons or ions) can move over extended distances successfully through a hopping mechanism. In this process, the neighbouring charge carriers relax to the location of the moving carrier. This mechanism leads to the *dc* conductivity at low frequencies. The second region is linked to the alternating current (*ac*) conductivity. Here, the charge carriers have limited or localized movement and fail to hop effectively, instead, they return to their original positions. This mechanism results in dispersive *ac* conductivity at higher frequencies. We find that the *ac* conductivity dominates above a critical frequency, and this critical frequency is determined by the sample's temperature and remains nearly constant across different values of the Nb concentration (x). In other words, the transition from *dc* to *ac* conductivity occurs at a specific frequency that depends on temperature, but found to be independent of x [see Figure 4.3(a–f)].

Further, the imaginary part of the impedance (Z'') for all the samples is investigated to gain more understanding into various contributing factors, including the effects of electrodes, individual grains, and grain boundaries. Figure 4.4(a–f) present the imaginary part of the impedance (Z'') for all the samples, which is a measure of the phase difference between the applied voltage and the resulting current. In the context of this study, it provides information about the relaxation processes within the material. In the Z'' spectra, relaxation maxima are observed, which are characteristic peaks at specific frequencies. These peaks offer details about the contribution of various factors: grain (bulk), grain boundary and ceramic-electrode interface. The samples with x values ranging from 0 to 0.6 exhibit well-defined relaxation peaks in the higher frequency range [see Figure 4.4(a–d)]. These peaks are attributed to the grain or bulk effect within the samples. In other words, they represent how the individual crystalline grains in the material respond to the applied electrical field. In the samples with x = 0–0.6, a weaker relaxation is also observed in the low-frequency range at higher temperatures. This lower-frequency relaxation is associated with the grain boundary mechanism, which involves how charge carriers move and interact at the interfaces between different crystalline grains.

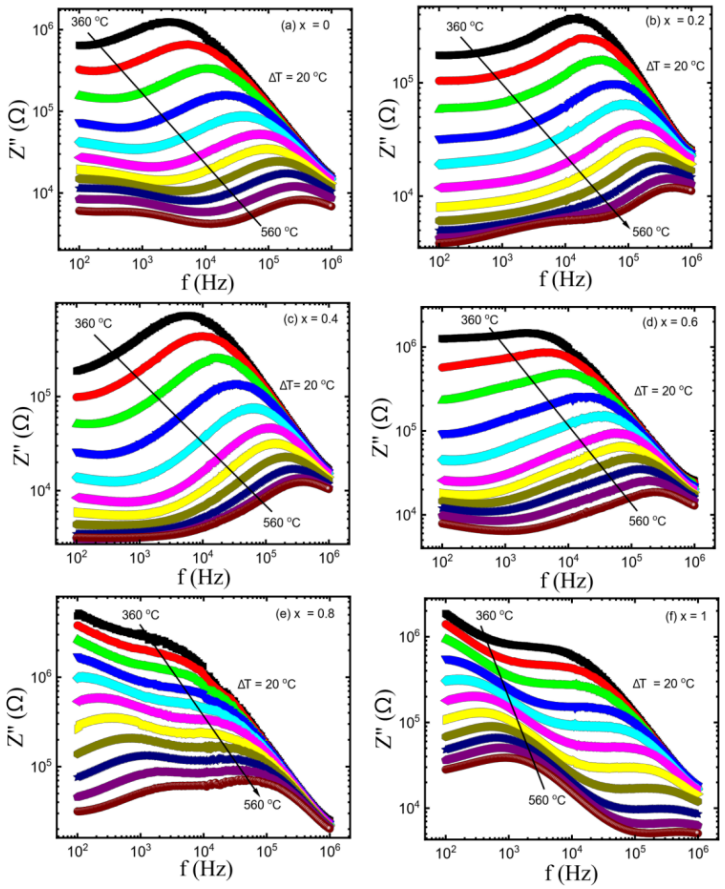


Fig. 4.4: (a-f) The imaginary part of impedance ($Z^{''}$) of $LaV_{1-x}Nb_xO_4$ (x = 0–1) samples plotted as a function of frequency from 100 Hz to 1 MHz at the selected temperatures from 360°C–560°C.

Additionally, the electrode interfaces between the material and the measuring electrodes can contribute to relaxation peaks in the low-frequency region [43–45]. As the temperature increases, the relaxation maxima in $Z^{''}$ tend to migrate toward higher frequencies, and their intensity weakens. The temperature-dependent behavior suggests that the relaxation

processes within the material are influenced by temperature, with relaxation occurring at higher frequencies as the temperature increases. For the samples with higher Nb substitution (x = 0.8 and 1), stronger relaxation peaks are observed in the lower-frequency regime compared to the samples with x values of 0 to 0.6 as well as at higher frequencies. This suggests that the substitution of Nb^{5+} at the V^{5+} site triggers grain boundary relaxation mechanisms in these samples, especially when x is equal to and greater than 0.8.

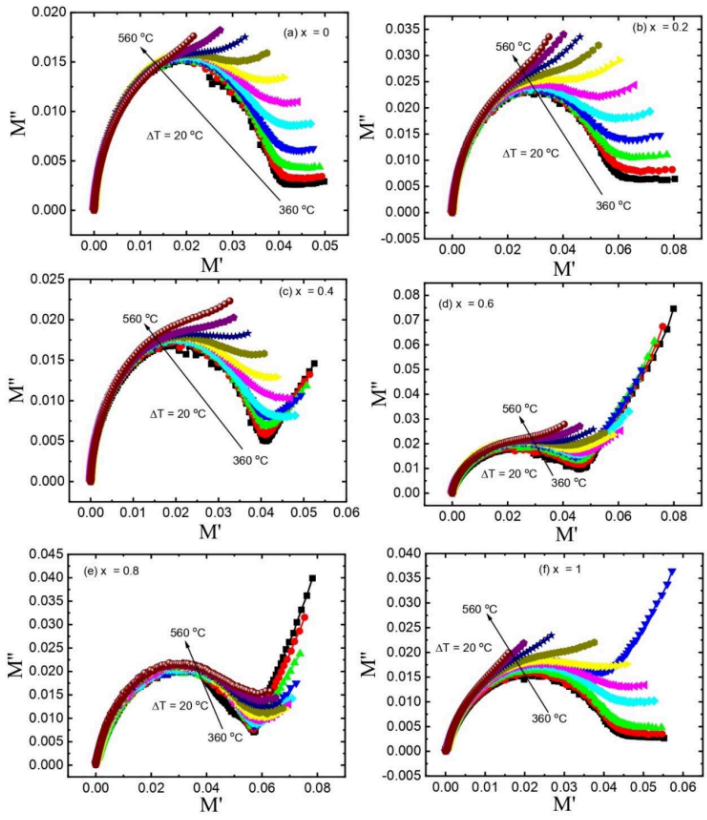


Fig. 4.5: (a-f) The imaginary (M″) versus real (M′) parts of electric modulus as a function of frequency from 100 Hz to 1 MHz at various temperatures from 360°C to 560°C for the $LaV_{1-x}Nb_xO_4$ (x = 0 - 1) samples.

It is important to plot the Nyquist modulus to comprehend the process underlying the relaxation behavior in these samples [46]. The modulus spectra [imaginary M″) versus real (M′)] that shows the behavior of different semicircular arcs, which are illustrated to distinguish each relaxation mechanism, as shown in Figure 4.5(a–f) for the samples. One semicircular arc can be seen in the real (M') versus imaginary (M'') modulus spectra for all the samples, which indicates that one of the relaxation processes has been severely inhibited by the surface polarization effect. When a small arc is formed at the end of the M' axis, it indicates a minor grain contribution, and when the temperature increases the arc eventually vanishes. This clearly demonstrates how the grain contribution finally diminishes with increase in the temperature. The M' versus M'' modulus spectra show that the electrode polarization at high temperature, extracted by the impedance spectroscopy, is drastically inhibited in this condition [47, 48]. At the higher frequencies, the grain boundary and electrode ceramic effects can also be seen, which increases with Nb^{5+} concentration and are not visible in impedance plots. In the samples x = 0.4, 0.6 and 0.8, electrode ceramic interface effects are more prominent which may be due to occurrence of mixed phases because of the significant contribution of both Nb^{5+} and V^{5+} elements.

In order to understand this mechanism, we use the relationship $2\pi\tau f_{max}=1$, where f_{max} represent the frequency at the peak in Z'' to determine the dielectric relaxation time (τ). In Figure 4.6, we plot the τ as a function of inverse of temperature for all the samples. We find that the relaxation time decreases when the temperature increases and it follow the Arrhenius relation for all the samples:

$$\tau = \tau_0 \exp -E_a/k_BT \quad (6)$$

where E_a is the activation energy of the charge carriers, k_B is the Boltzmann's constant, and τ_0 represents the pre-exponential factor in the relaxation time. The activation energy is typically associated with breaking and forming the chemical bonds, i.e., the minimum amount of energy required for a given relaxation process to activate. The estimated values of activation energy for the x = 0–0.8 samples are found to be 0.98 eV, 0.84 eV, 1.0 eV, 0.88 eV, and 1.41 eV, respectively. The x = 0.8 sample shows maximum activation energy among all, which may be associated with the highest Nb concentration

for the exponent m, and (c) the constant B as a function of temperature for the $LaV_{1-x}Nb_xO_4$ (x = 0–1) samples. The coexisting monoclinic-monazite ($P2_1/n$) and tetragonal scheelite ($I4_1/a$) phases, and hence largest average particle size of this samples, observed from the scanning electron microscopy (SEM) [3]. In case of the x = 1 sample, a change in the activation energy is observed near 460°C from 1.02 eV to 0.48 eV, which can also be reflected in Figure 4.2(f), where an additional relaxation peak is observed in this sample. The transformation of the x = 1 sample from the monoclinic fergusonite (space group $I2/a$) structure at the low temperature to the tetragonal scheelite (space group $I4_1/a$) phase at the higher temperature, and hence availability of the large thermal energy of the charge carriers results in this observed reduction in the activation energy above a threshold temperature of around 460°C [13].

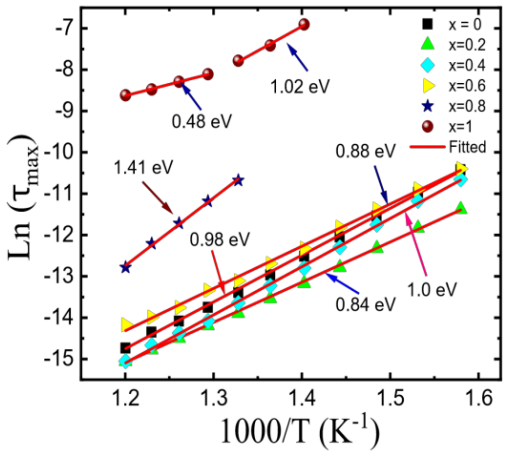


Fig. 4.6: The variation in the relaxation time with inverse of the temperature for $LaV_{1-x}Nb_xO_4$ (x = 0–1) samples. The solid red lines represent the best fit using the Arrhenius equation.

In Figure 4.7(a–f), we present the total conductivity (σ) of the samples as a function of angular frequency (ω) in the temperature range of 360°C–560°C. The solid lines represent the best fit of the experimental data using Jonscher Power Law (JPL) equation:

$$\sigma = \sigma_{dc} + B\omega^m \qquad (7)$$

where σ_{dc} represents the *dc* conductivity, $B\omega^m$ represents the *ac* conductivity (σ_{ac}), where both the *B* and *m* are the measure of strength of polarization and degrees of interaction of charge carriers, respectively. Both of these quantities are supposed to be dependent on temperature. We find that the σ values are strongly frequency dependent and gradually increases at the higher frequencies.

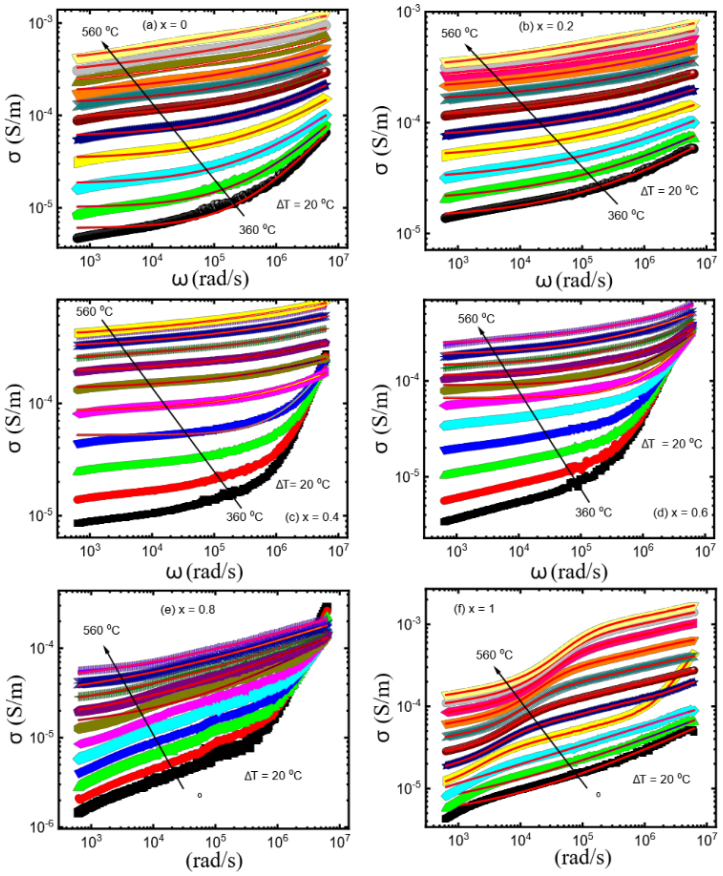


Fig. 4.7: The variation in the relaxation time with inverse of temperature for $LaV_{1-x}Nb_xO_4$ (x = 0–1) samples. The solid red lines represent the best fit using the Arrhenius equation.

Further, the conductivity increases monotonically with increase in temperature for all the samples. Note that at lower temperatures the conductivity increases towards higher frequency; however, it shifts towards the saturation at higher temperatures, which indicates a threshold in the conductance mechanism in the materials. At the lower temperature and high frequency region, the conductivity becomes frequency dependent and this frequency dependence increases from $x = 0$ to 0.8, whereas for the $x = 1$ sample a weak relaxation in the conductivity is observed in the low frequency region, which is more clearly visible above 400°C, which may be attributed to the presence of single monoclinic (*I2/a*) phase in this sample [3]. The total conductivity for the $x = 0$, 0.2 and 1 follows Jonscher Power Law equation in the temperature range of 360°C–560°C, whereas for the $x = 0.4$, 0.6 and 0.8 sample it follows the Jonscher Power Law equation above 420°C, 460°C and 480°C temperatures, respectively.

Finally, in Figure 4.8(a) we show the variation of the σ_{dc} with the temperature where we observe that the σ_{dc} increases non-linearly in the temperature range of 360°C– 560°C, which shows the semiconducting/insulating nature of the materials. There have been various models reported to understand the conductivity of different complex oxide samples on the basis of exponent *m* as well as the polaron tunneling. It is important to note that a local lattice deformation can result due to the addition of charge transporters to a site in a solid. Further, a polaron can be created by the arrangement of electrons as well as the local distortion. In the current study, we find that the *m* values decrease with temperature for all the samples, except for $x = 1$, which shows the decreasing valley near 480°C and the subsequent increase in value indicates the presence of the overlapping large polaron tunneling (OLPT) conduction mechanism [49, 50]. In this mechanism, the polaron clouds extend considerably beyond the typical interatomic distances [51]. As the temperature increases, the *m* values shown in Figure 4.8(b) exhibits a linear ascent until it reaches approximately 540°C, elucidating the behavior of non-overlapping small polaron tunnelling (NSPT) [52]. During this phase, the polarons are confined to the extent that their distortion clouds do not intersect. Consequently, the electron's tunnel between states near the Fermi level, and the tunnelling energy remains unaffected by inter-site distances [51]. The *m* value eventually levels off at around 560°C, a phenomenon explicable by quantum mechanical tunneling (QMT) [53].

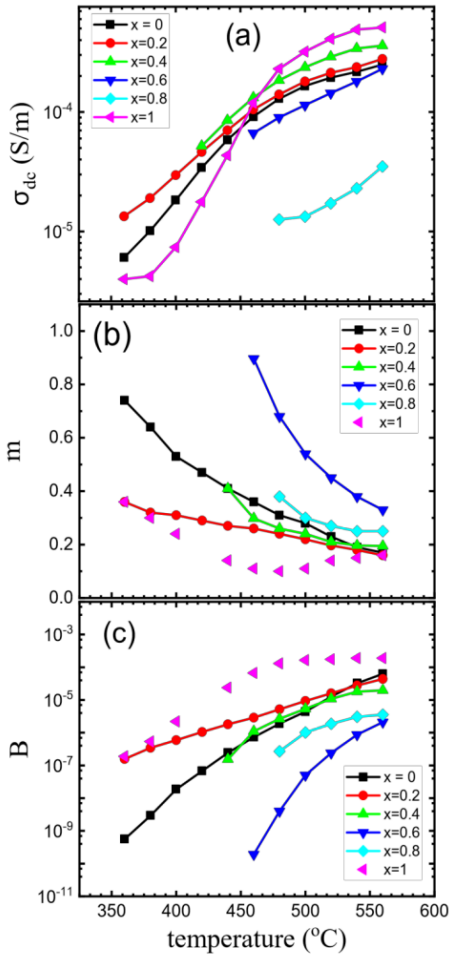


Fig. 4.8: The best fit parameters of the *ac* conductivity using Jonscher power law, (a) the *dc* conductivity (b) the exponent m, and (c) the constant B as a function of temperature for the $LaV_{1-x}Nb_xO_4$ (x = 0–1) samples.

Notably, the temperature independence of m in this model distinguishes it [54]. This characteristic underscores that conduction occurs primarily through the tunneling of

electrons between defect states near the Fermi level, without the generation of polarons. Similarly, the values of B shown in Figure 4.8(c) increases nonlinearly with temperature for all the samples, except for the $x = 1$, which shows the saturation near 560°C, which means the polarization strength is also getting saturated at higher temperatures, which is found to be consistent with the dielectric behavior, as shown in Figure 4.2.

4.4 Summary and Conclusions

We measured the dielectric constant and tangent loss at temperatures ranging from 25°C to 600°C and a wide range of frequencies (100 Hz to 1 MHz) for $LaV_{1-x}Nb_xO_4$ ($x = 0$–1) samples. We found that the dielectric constant increased with temperatures, but decreased in magnitude with frequency having the value $\approx 10^4$ at 100 Hz and 600°C. The iso-electronic substitution of Nb^{5+} at V^{5+} site did not significantly affect the magnitude of the dielectric constant. The anomalous behavior in $\varepsilon_r'(T)$ curves have been observed for the $x = 0.2$–0.8 samples due to their mixed structural phases, whereas no relaxation peak was observed for the $x = 0$ sample, and a weak relaxation was seen for the $x = 1$ sample at the higher temperatures. The mixed phase in the $x = 0$ to 0.8 samples show the significantly higher values of the tangent loss as compared to the single phase $x = 0$ and 1 samples. The real part of the impedance (Z') spectroscopy decreased with temperature and frequency, and a weak relaxation was observed in all the samples with negligible changes in magnitude with x. The imaginary part of the impedance (Z'') exhibited strong relaxation peaks that shifted toward higher temperatures with frequency, which described the grain, grain boundary, and electrode effects in the samples. The Z''–f plots exhibited similar behavior for the $x = 0$ to 0.6 samples, but for the $x = 0.8$ and 1, the relaxation was observed in the lower frequency region, indicating the grain boundary effect along with the grain effect. The activation energy of the relaxation processes for the $x = 0$–0.6 samples found to be in the range of 0.8 to 1.0 eV, whereas for the $x = 0.8$, the activation energy was calculated to be around 1.4 eV due to highest Nb concentration in the multiphase samples. Further, for the $x = 1$ sample, two values of the activation energy were observed, i.e., around 1.0 eV and 0.5 eV, which indicated the transition near 460°C. We measured the total conductivity (10^{-3} to 10^{-5} S/m) with varying frequency in the temperature range of 360°–560°C and fitted it with the Jonsher power law. The fitted *dc* conductivity behavior showed the semiconducting

characteristics of all the samples, with x = 0.8 having the lowest conductivity. The analysis showed that all the samples exhibited OLPT mechanism, whereas the x = 1 exhibited a transition near 480°C, which was also reflected in the tangent loss plots. As an exception, we find NSPT and QMT mechanisms for the x = 1 sample at higher temperatures.

Chapter 5

Physical and Dielectric Properties of Polycrystalline $LaV_{0.5}Nb_{0.5}O_4$

In this chapter, we investigate the structural, electronic, vibrational, and dielectric properties of polycrystalline $LaV_{0.5}Nb_{0.5}O_4$ samples, prepared at two sintering temperatures (1000˚C and 1250˚C). The introduction of Nb^{5+} at the V^{5+} site leads to notable structural and vibrational changes, which can be attributed to their isoelectronic nature and the comparatively larger ionic radius of Nb^{5+}. The Rietveld refinement of the X-ray diffraction patterns confirms a coexistence of monoclinic ($P2_1/n$) and scheelite-type tetragonal ($I4_1/a$) phases; for example, with a fraction of 4% and 96% for the sample annealed at 1250˚C. The particle morphology has altered from spherical (1000˚C) to irregular-shaped (1250˚C) as a result of increase in annealing temperature. The Raman spectroscopy, Fourier Transform Infrared spectroscopy and X-ray Photoemission Spectroscopy have been used to understand the vibrational and electronic properties. An optical band gap of 2.7 eV for the sample sintered at 1250˚C is calculated using Ultraviolet-vis diffuse reflectance spectroscopy measurements. The dielectric studies shows the higher dielectric permittivity (ϵ_r) and lower dielectric loss for the sample annealed at 1250˚C.

5.1 Introduction

In last few decades, rare-earth orthovanadates have emerged as a significant class of functional materials with broad environmental and industry applications spanning as luminescent materials, catalysis, solid oxide fuel cells, battery electrodes, thermometers and photocatalysts [1–5]. The orthovanadates with general formula RVO_4, where R is a rare-earth ion, such as La^{3+}, Gd^{3+}, Y^{3+} etc., represent a versatile family of materials having the VO_4^{3-} tetrahedral units, which serve as the fundamental building blocks [6–9]. It allows the rare earth cations to form a crystal field, which upon perturbation, results in energy transition and phenomena of photoluminescence [10]. In the family, the lanthanum based orthovanadates, i.e., $LaVO_4$ has been considered most interesting due to its exceptional optical, electronic and structural properties [3] as well as used for

targeted alpha therapy in cancer treatment through radionuclide encapsulation using ^{223}Ra to form La(^{223}Ra)VO_4 [11]. Interestingly, the $LaVO_4$ exhibits peculiar structural polymorphism, crystallizing primarily in two structure types: the tetragonal (t-) zircon-type (space group $I4_1/amd$ [141]) and the monoclinic (m-) monazite-type (space group $P2_1/n$ [14][12, 13]. In the monoclinic monazite structure, La^{3+} ions are coordinated by nine oxygen atoms forming edge sharing LaO_9 polyhedra and connected with distorted VO_4 tetrahedra with four different V–O bond lengths. However, in the tetragonal zircon structure, La^{3+} ions are eight-fold coordinated with the equal V–O bond lengths and linked together through chains along the c–axis. Importantly, the $LaVO_4$ shows stability in monoclinic monazite structure at room temperature with La^{3+} ion's high tendency to crystallize in nine-coordination as compared to the eight coordination in tetragonal zircon structure [12]. This is mainly because the phase stability is dependent on the cation radius and La^{3+} has the largest ionic radius (1.16 Å) as compared to other rare earth cations. The tetragonal (zircon-type) phase of $LaVO_4$ is metastable at room temperature, but can be synthesized through solution-based methods such as hydrothermal [12, 14]. Interestingly, the tetragonal structure exhibits superior luminescence properties due to the presence of four identical V–O bonds (angle $\approx 153^{\circ}$), which facilitate more efficient energy transfer [15]. In contrast, the monoclinic monozite phase has smaller bond angles, resulting in less effective energy transfer [15]. The $LaVO_4$ is a self-activated ABO_4 type host compound, emitting broad blue emission from 380 nm to 450 nm region with maxima at 430 nm upon UV light excitation. This corresponds to a transition from two close lying $^1A_1(^1E)$ and $^1E_1(^1T_2)$ excited states to $^1A_2(^1T_1)$, ground state of $(VO_4)^{3-}$ion [16]. Here, the Lanthanum is significantly more abundant and less expensive than Yttrium, making $LaVO_4^-$ based materials economically attractive alternatives to the widely used YVO_4 phosphors [17]. This cost advantage is particularly important for large-scale applications in lighting and display technologies.

Notably, the structural diversity enables tunable optical and electronic properties through composition and external conditions such as pH, temperature and pressure [11, 12, 18]. Therefore, substitution at V^{5+} site in $LaVO_4$ has been explored through various dopants, such as Mn^{4+} where $LaV_{1-x}Mn_xO_{4-\delta}$ ($0 \leq x \leq 1$) mixed oxides were synthesized

in single-phase with reproducible redox behavior ($LaVO_4$ to $LaVO_3$), which indicate that the Mn doping lowered reduction/oxidation temperatures and enhanced oxygen vacancy formation and mobility for catalytic performance [19]. Interestingly, substituting low-cost Nb^{5+} at the V^{5+} site in $LaVO_4$ motivated by the intriguing structural and optical behavior arising from the isoelectronic character (d^0 electronic configuration) and larger ionic radii of Nb^{5+} as compared to V^{5+} [5–7]. It has also been well-demonstrated that even small amounts of Nb^{5+} substitution ($x \geq 0.05$) can induce the formation of the scheelite-tetragonal phase ($I4_1/a$) along- side the monoclinic phase at room temperature [5]. The presence of the tetragonal phase significantly enhances photoluminescence properties and the structural transformation can be controlled by varying the Nb concentration [5–7]. Meanwhile, the end composition in the series, i.e., the $LaNbO_4$ is a rare-earth niobate and structurally transforms from monoclinic fergusonite ($I2/a$) to tetragonal scheelite ($I4_1/a$) at 495°C [20]. On the other hand, Ding et al. reported the $LaNbO_4$ in monoclinic phase, which exhibits interesting luminiscent features with fluorescence lifetime of 5.51 μs [21]. In a similar fashion, when V^{5+} ion is substituted at the Nb^{5+}, the composition induced structural transition is observed [22]. Upon excitation with a UV or X-ray source, charge transfer from O 2*p* to Nb 4*d* band in $LaNbO_4$ yielded a blue luminescent material, as demonstrated by Blasse et al. in ref. [23]. However, the composition $LaV_{0.5}Nb_{0.5}O_4$ remains largely unexplored and presents significant scope for detailed investigation particularly to see the effect of sintering temperature during the synthesis process as well as temperature dependent dielectric properties [5–7].

Therefore, the primary aim of this work is to study polycrystalline lanthanum orthovanadate with niobium substitution, specifically targeting the composition $LaV_{1-x}Nb_xO_4$ where x equals 0.5, utilizing the solid-state method and investigate sintering temperature induced phase transformation and understand the dielectric properties. Interestingly, the crystal structure and morphology of the orthovanadates is strongly dependent upon the synthesis approach, annealing temperature and concentration of active ions. Herein, the $LaV_{0.5}Nb_{0.5}O_4$ sample crystallize in two distinct, monoclinic monazite type and tetragonal zirconite type phases in different fractions, as confirmed by the Rietveld refinement of X-ray diffraction (XRD) patterns.

The scanning electron microscopy (SEM) measurements unveil the morphological variations with the sintering temperature. The Raman spectroscopy and Fourier transform infrared spectroscopy (FTIR) measurements identify the presence of vibrational bonds in the prepared samples. The energy band gap values have been estimated through ultraviolet-visible diffuse reflectance spectroscopy measurements. The core-level X-ray photoemission spectroscopy studies depict the electronic structure and oxidation state of the constituent elements in both the samples. The microstructure has been successfully confirmed by the high-resolution transmission electron microscopy measurements. The dielectric measurements reveal the dielectric permittivity (ϵ_r) and dielectric loss in the temperature range of 100 K to 400 K for the samples annealed at 1000˚C and 1250˚C. The *a.c.* conductivity studies are performed to understand the charge carrier dynamics with variable temperature and frequencies.

5.2 Experimental

The $LaV_{0.5}Nb_{0.5}O_4$ bulk sample was synthesized via a conventional solid-state reaction route. Prior to synthesis, La_2O_3 was pre-heated at 900˚C for 6 h with a ramp rate of 4 ˚C min^{-1} in order to remove the adsorbed moisture. The calcined La_2O_3 was quenched to room temperature and weighed immediately to prevent re-hydration. High-purity La_2O_3, V_2O_5, and Nb_2O_5 were mixed in the stoichiometric ratio to obtain a 2 g final yield of the powder. The precursors were thoroughly mixed and ground in an agate mortar and pestle for 6 h to ensure homogeneous mixing. The resulting powder was pelletized under a uniaxial pressure of 1500 kg cm^{-2}, followed by calcination at 1000˚C for 17 h with a heating rate of 5 ˚C min^{-1}. The calcined product was reground for approximately 5 h to ensure homogeneity and subsequently re-pelletized under the same applied pressure (1500 kg cm^{-2}). The final sintering was carried out at 1250˚C for 13 h with a ramp rate of 5˚C min^{-1}. The $LaV_{0.5}Nb_{0.5}O_4$ samples annealed at 1000˚C and 1250˚C are abbreviated as LVNO-1000 and LVNO-1250, respectively.

The X-ray diffraction (XRD) measurements were carried out using a Panalytical X'Pert3 diffractometer equipped with Cu Kα radiation (λ = 1.5406 Å). The Rietveld refinement of the powder XRD patterns is performed using the FullProf software, with the background fitted using linear interpolation between the data points. The

morphology of the bulk samples is examined using a field-emission scanning electron microscope (FE-SEM, Technai Magna LMU). The elemental mappings are probed through the EDX detector system (EDAX AMETEK, Octane Elite Super EDS). The Fourier-transform infrared spectroscopy (FTIR, Thermo Nicolet IS-50) is performed in Attenuated Total Reflectance (ATR) mode over the spectral range of 400–4000 cm^{-1} to analyse vibrational modes. The X-ray photoelectron spectroscopy (XPS, Kratos AXIS Supra) is employed to investigate the valence state using monochromatic Al Kα radiation (1486.6 eV) as the excitation source, with a pass energy of 20 eV and a step size of 0.1 eV. The spectral fitting is performed using FitYk software with Voigt function (Shape factor = 0.6), and the C 1*s* peak at 284.6 eV was used as the reference for calibration. The microstructure of the bulk samples is examined using transmission electron microscopy (TEM, JEM-ARM200F NEOARM). The Raman spectroscopy is performed using a Renishaw inVia confocal Raman microscope equipped with a 532 nm laser, a 2400 lines/mm grating, and a laser power of 10 mW to investigate the vibrational modes of the samples. The UV-vis (Ultraviolet-visible) diffuse reflectance spectroscopy (DRS) measurements are conducted using a Perkin Elmer's Lambda 1050 model in the spectral range of 300–2500 nm to measure the absorption edge energy of the samples using the Barium Sulfate standard. The pellets were polished and painted with sliver paste on both the sides for the dielectric measurements. The dielectric studies are done in the temperature range of 90–400 K by varying the frequency from 100 Hz–2 MHz using the Agilent LCR meter (model E4980A). The temperature is varied using the Lakeshore temperature controller (model-340) and temperature was measured using the Pt-100 sensor. The measurements are performed in the vacuum of the order 10^{-2} mbar by placing the sample holder in liquid nitrogen Dewar.

5.3 Results and Discussion

The room temperature Rietveld refined XRD patterns of as-prepared polycrystalline $LaV_{0.5}Nb_{0.5}O_4$ samples, annealed at 1000°C and 1250°C are depicted in Fig. 5.1(a,b), respectively. It is observed that the measured XRD pattern consists of a mixture of monoclinic ($P2_1/n$) and scheelite-tetragonal ($I4_1/a$) phases in varying proportions, rather

than a single P21/n phase [22]. The structural phase transformation in the LVNO sample is caused by the Nb^{5+} substitution at the V^{5+} site in a tetrahedral coordination, because the ionic radius of Nb^{5+} (0.48 Å) is larger than that of V^{5+} (0.355 Å) [24].

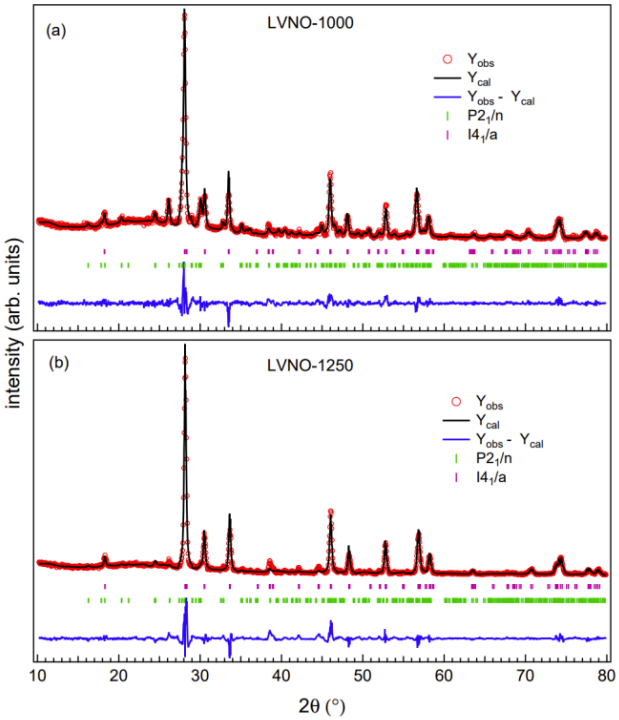


Fig. 5.1: The room temperature XRD patterns with Rietveld refinement of (a) LVNO-1000 and (b) LVNO-1250 samples. The open red circles, black solid line, and blue solid line exhibits the experimental, calculated, and the difference between experimental and calculated pattern, respectively. The vertical green and purple markers show the Bragg positions corresponding to the $P2_1/n$ and $I4_1/a$ space groups.

It is also reported in the literature that end members, the $LaVO_4$ and $LaNbO_4$ co-exist in the monoclinic monazite ($P2_1/n$) and fergusonite monoclinic ($I2/a$) phases, respectively, at room temperature [25, 26]. Consequently, it is anticipated that Nb^{5+} substitution in $LaVO_4$ will induce a phase transformation from $P2_1/n$ to $I2/a$. In the $LaVO_4$ sample,

synthesized at 1000˚C, the XRD pattern is well fitted using monoclinic ($P2_1/n$) and scheelite-tetragonal ($I4_1/a$). The phase exhibits diffraction peaks characteristic of a crystalline solid; however, the peaks appear relatively broad and of lower intensity compared to those of the sample sintered at 1250˚C. This broadening indicates a reduced degree of crystallinity and/or smaller crystallite size in the LVNO-1000 sample. In contrast, the LVNO-1250 sample displays sharp and intense diffraction peaks, signifying enhanced crystallinity and larger crystallite dimensions, as shown in Fig. 5.1(b). The higher synthesis temperature likely promotes more complete crystallization and grain growth. The diffraction peaks for both the samples sintered at 1000˚C and 1250˚C correspond to two structural phases: the scheelite-type tetragonal phase ($I4_1/a$) and the monoclinic phase ($P2_1/n$).

The lattice parameters and wyckoff positions of LVNO-1000 and LVNO-1250 samples are summarized in Table 5.1 and Table 5.2, respectively. It is observed that angle β has slightly increased with increase in sintering temperature, as a result of increase in tetragonal phase fraction. The quantification of the relative phase fractions for both the samples has also been investigated through Rietveld refinement. The phase fractions of 51% tetragonal ($I4_1/a$) and 49% monoclinic ($P2_1/n$) are calculated for the LVNO-1000 sample. On the other hand, the LVNO-1250 sample exhibits a dominant tetragonal fraction of 96% and a monoclinic fraction of 4%. The predominance of the tetragonal phase at the higher temperature is consistent with its thermodynamic stability and structure becomes more homogeneous through completion of solid-state reaction. This is consistent with the previ-ous work, where sintering of $LaV_{1-x}Nb_xO_4$ (x = 0.1, 0.2) at 1450˚C promoted the stabilization of scheelite-tetragonal phase [5]. In addition, Xie et al. reported the mechanism of formation of tetragonal phase as a result of intermediate complex $V_xO_y^{(2y-5x)-}$, which forces La^{3+} to coordinate in fewer coordination value (here, 8) due to strong stearic hindrance [27]. This increment in tetragonal phase fraction is better for superior luminescent characteristics [28].

Table 5.1: The structural and atomic parameters obtained from Rietveld refinement of the sample sintered at 1000°C.

Tetragonal Phase: $a = b = 5.348$ Å, $c = 11.694$ Å					
Atom	x	y	z	Occ.	Site
Nb	0.0000	0.0000	0.0000	1.00	36f
O	0.2635	0.8049	0.1435	1.00	36f
La	0.0000	0.0000	0.5000	1.00	6b
Monoclinic Phase: $a = 7.054$ Å, $b = 7.278$ Å, $c = 6.731$ Å $\beta = 104.909°$					
Atom	x	y	z	Occ.	Site
V	0.3071	0.1657	0.6066	1.00	36f
O1	0.2438	0.0155	0.4594	1.00	36f
O2	0.3676	0.3134	0.5676	1.00	36f
O3	0.4553	0.0593	0.8394	1.00	6b
O4	0.1324	0.2049	0.7648	1.00	18e
La	0.2723	0.1613	0.1128	1.00	18e

Table 5.2: The structural and atomic parameters obtained from Rietveld refinement of LVNO sintered at 1250°C.

Tetragonal Phase: $a = b = 5.327$ Å, $c = 11.716$ Å					
Atom	x	y	z	Occ.	Site
Nb	0.0000	0.0000	0.0000	1.00	36f
O	0.2500	0.7682	0.1576	1.00	36f
La	0.0000	0.0000	0.5000	1.00	6b
Monoclinic Phase: $a = 7.027$ Å, $b = 7.293$ Å, $c = 6.732$ Å $\beta = 104.947°$					
Atom	x	y	z	Occ.	Site
V	0.3024	0.1699	0.5733	1.00	36f
O1	0.1951	0.0846	0.4725	1.00	36f
O2	0.5818	0.3642	0.5407	1.04	36f
O3	0.8340	0.1151	0.7265	0.95	6b
O4	0.0960	0.6676	0.2146	0.76	18e
La	1.6958	0.2865	0.1337	1.00	18e

The FE-SEM images of the LVNO samples, sintered at 1000˚C and 1250˚C are presented in Fig. 5.2(a–f). The LVNO-1000 sample shows an average particle size of approximately 0.8 µm. In contrast, the LVNO-1250 sample exhibits a non-uniform particle size distribution ranging from 0.2 µm to several micrometers, as depicted in Fig. 5.2(b). The grain size has increased with the increase in sintering temperature, as the shape changing from spherical (at 1000˚C) to irregular-shaped (at 1250˚C) particles. The morphological difference along with the visible textural changes, such as inevitable agglomeration in the LVNO-1250 sample, provide additional evidence of the temperature-induced phase transformation.

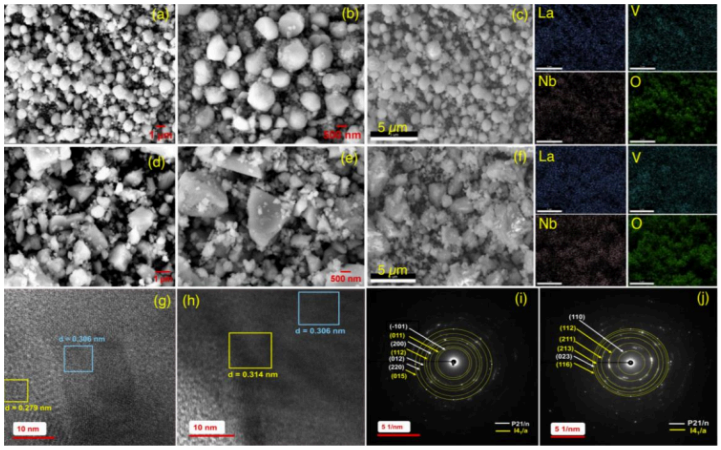


Fig. 5.2: The FE-SEM images of the LVNO-1000 sample at (a) 1µm, (b) 500 nm and (c) probed region of scan (at 5µm) with the corresponding elemental mappings of all elements; the FE-SEM images of the LVNO-1250 sample at (d) 1µm, (e) 500 nm and (f) probed region of scan (at 5µm) with the corresponding elemental mappings of all elements; the HR-TEM images of (g) sintered at 1000˚C and (h) sintered at 1250˚C with the marked d-spacings across the selected region; the SAED patterns for the LVNO-1000 (i) and LVNO-1250 (j), respectively.

The grain boundaries diffuse, smaller particles rearrange to large sized particles and coalescence occurs as a result of high temperature annealing [29]. Furthermore, the uniform distribution of elements in LVNO-1000 and LVNO-1250 samples can be clearly observed in Fig. 5.2(c, f). The HR-TEM analysis of the LVNO-1000 sample

clearly reveals its biphasic nature, with distinct coexisting lattice fringes exhibiting d-spacings of approximately 0.28 nm and 0.3 nm, depicted in Fig. 5.2(g). The indexed (h, k, l) planes that relate to $P2_1/n$ and $I4_1/a$ are colored in white and yellow, respectively, see Fig. 5.2(g, h). The corresponding SAED pattern further confirms the mixed phase structural arrangement, where the reflections (-101), (200), (012) and (220) belong to the monoclinic phase and (011), (112) and (015) belong to the tetragonal phase, see Fig. 5.2(i, j). For the LVNO-1250 sample, the HR-TEM images indicate a dominant tetragonal phase [see Fig. 5.2(h)], with measured d-spacings shifting to around 0.31 nm, which are characteristic of the major tetragonal reflections. The SAED pattern for this sample is overwhelmingly dominated by diffraction spots consistent with the $I4_1/a$ phase, including the (112), (211), and (213) reflections [see Fig. 5.2(j)], providing strong evidence that higher sintering temperature promotes the stabilization and predominance of the tetragonal phase. This is in agreement with the refined X-ray diffraction analysis, presented in Figs. 5.2(a, b).

In order to confirm the structure and possibility of infrared active modes of the $LaV_{0.5}Nb_{0.5}O_4$ sample, the ATR-FTIR measurements have been performed, as depicted in Fig. 5.3(a), with the closer view shown in the inset. The observed well-resolved bands are marked with the black vertical arrows [inset of Fig. 3(a)] and are in close agreement with ref. [5]. Herein, a strong and distinct band is observed at 432 cm^{-1}, with a weak band at 478 cm^{-1}, which are linked to the v_4 bending vibrations of the $(V/Nb)O_4^{3-}$ tetrahedra [3]. Similarly, wide bands are observed between 600–900 cm^{-1}, where a peak at 804 cm^{-1} corresponds to the antisymmetric stretching vibrations of VO_4^{3-}tetrahedra. Meanwhile, the peaks at 820, 835 and 848 correspond to the v_3 stretching vibrations of VO_4^{3-} tetrahedra [30] and show a small shift in the peaks in comparison to pristine $LaVO_4$ sample [5]. In addition, the peaks at 679, 729 and 761 cm^{-1} have been originated with the incorporation of Nb at V site and are absent in the $LaVO_4$ sample. These features can be correlated with the additional symmetry modes, arising from the mixed scheelite-tetragonal phase, as proven in X-ray diffraction measurements. However, the ATR-FTIR spectra for LVNO-1250 sample shows less intense band around 417 cm^{-1} , while the

peaks in the range of 600-900 cm^{-1} appear as a single broad band, depicted in Fig. 5.3(a). It can be inferred that IR activity gets reduced with increasing temperatures due to increase in thermal energy and as a result, intensity of specific vibrational bands are reduced.

The UV-vis DRS measurements are conducted to understand the absorption edge energy of the synthesized LVNO samples, sintered at 1000˚C and 1250˚C. The reflectance spectra [see Fig. 5.3(b)] observed for both the samples is converted to Tauc plot using the Tauc method [31]. The diffuse reflectance spectra (DRS) are employed to calculate the Kubelka-Munk (K-M) function [$F(R_\infty)$], shown in Fig. 3(c), which can be treated in terms of diffuse semi-infinite reflectance ($R_\infty = R_{sample}/R_{standard}$) as written below [32]:

$$F(R_\infty) = (1 - R_\infty)2/2\, R_\infty \quad (1)$$

The band gap of the LVNO samples can be obtained from the absorption threshold energy, which is the x−axis intercept of the Tauc plot [see Fig. 3(c)] and related as [33]:

$$(\alpha h\nu) = k(h\nu - Eg)^{\eta} \quad (2)$$

where α, ν, k, E_g and η are the absorption coefficient, frequency, absorption constant, band gap energy and exponent of the equation, respectively [34]. The value of the exponent η depends on the type of the transition/band gap in the material and can have values of 1/2, 2, 3/2 and 3 for the direct allowed, indirect allowed, direct forbidden and indirect forbidden transitions, respectively [31, 34]. However, in the case of diffuse reflectance spectra, the α in Tauc plot can be replaced by the K-M function to estimate the band gap of the material [3]. As reported in [5], the LVNO samples has indirect band gap, therefore, the value of exponent, η is 2, therefore, $[F(R_\infty) \times h\nu]^{1/2}$ versus hν is plotted for both the samples, shown in Fig. 5.3(c). This curve shows the linear and nonlinear portions which are the characteristics for allowed transitions. The linear portion of the curve which lies in the range approximately 3 eV to 4.5 eV characterizes the fundamental absorption of the materials and the non-linear portion of the curve correspond to a residual absorption, which involves defect states.

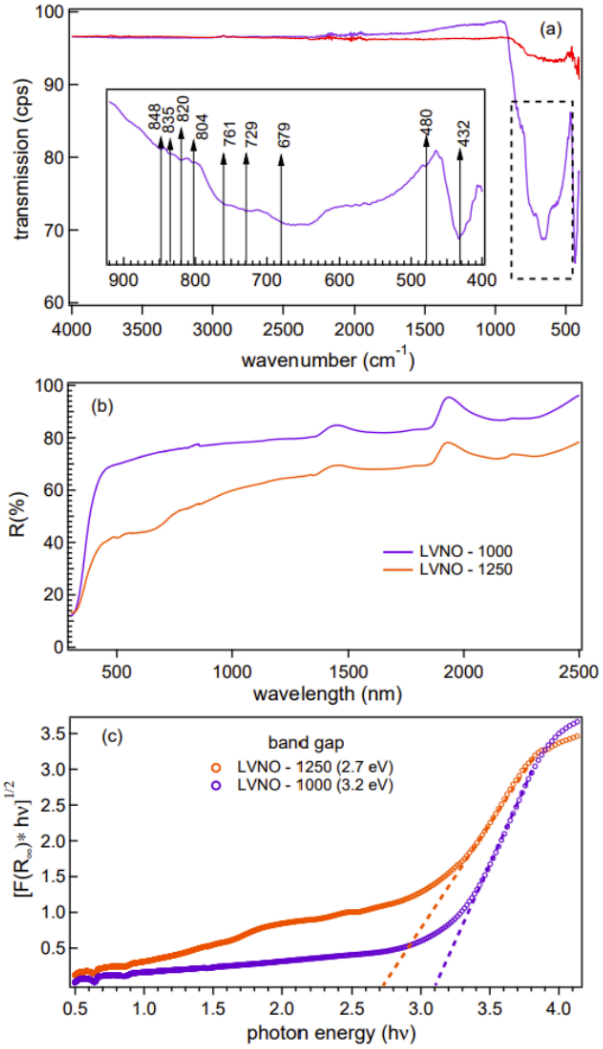


Fig. 5.3: (a) The FTIR spectra, (b) the UV-vis DRS plots and (c) the Kubelka-Munk plots obtained from the DRS data for the LVNO-1000 and LVNO-1250 samples, respectively.

The x−axis intercept along the optical absorption edge of the samples estimates the optical band gap, which is calculated as 3.2 and 2.7 eV for the 1000˚C and 1250˚C, respectively. Also, Sun et al. reported that monoclinic LaVO4 phase possess indirect band gap of 3.5 eV, while tetragonal phase has direct band gap of 3 eV through the first-principle calculations [35]. Therefore, it can be clearly inferred that band gap decreases upon increasing the sintering temperature, as a result of increase in tetragonal phase in LVNO-1250 sample and further enhances the photoluminescence. This is also in agreement with the previously reported literature [3, 5, 33].

Moreover, the Raman spectra recorded at a room temperature using a 532 nm excitation laser line for both the samples are presented in the Fig. 5.4(a-d). A Voigt profile function is employed to deconvolute and fit the observed Raman modes, as mentioned in the Table 5.3. The intensity of observed Raman modes may fluctuate due to various factors, including the molecule's polarizability, the excitation wavelength of the laser source, and the concentration of the active groups [6]. The detailed description of the various types of Raman modes has been discussed in our previous works [5, 6]. As per the group theory calculations reported, m-$LaVO_4$ consists of 72 vibrational modes ($18B_u + 18A_u + 18A_g + 18B_g$), which includes 3 acoustic modes ($A_u + 2B_u$), 33 infrared-active modes ($16B_u + 17A_u$), and 36 Raman active modes ($18A_g + 18B_g$) [35]. In this context, we employ Mulliken symbols, with notations A and B indicating that the vibrations are symmetric and anti-symmetric relative to the major axis of symmetry, respectively. The subscripts *g* and *u* denote that the vibrations are symmetric and anti-symmetric, respectively, concerning a center of symmetry. Meanwhile, the vibrational frequencies of tetragonal $LaVO_4$ (t-$LaVO_4$) consists of 36 vibrational modes and 33 zone-center optical phonon modes, with five E_g, four E_u, four B_{1g}, three A_{2u}, two A_{1g}, two B_{2u}, and one each of the A_{1u}, A_{2g}, B_{1u}, and B_{2g} symmetry representations. Among these, the A_{2u} and E_u modes are infrared active, whereas the A_{1g}, B_{1g}, B_{2g}, and E_g modes are Raman active. However, the remaining A_{1u}, A_{2g}, B_{1u}, and B_{2u} modes are silent. The Raman, A_g, and B_g modes can be experimentally identified by polarized Raman measurements. The detailed description of the modes can be referred to references in [6, 35, 36].

The Raman modes in the lower wavenumber region for the LVNO-1000 and LVNO-1250 samples are presented as P0 to P23 and P24 to P32, respectively, in Fig. 5.4. Meanwhile, the corresponding details of Raman modes are described in Table III. In the $LaV_{0.5}Nb_{0.5}O_4$, the Raman peaks appear as a result of various vibrational bonds among La^{3+}, V^{5+}, Nb^{5+} and O^{2-}. The Raman modes in the wavenumber region (600–800 cm^{-1}) are related to the stretching vibrations of O–(V/Nb)–O bonds and modes (300–450 cm^{-1}) correspond to the bending vibrations of O–V–O bonds and deformation/scissior modes of NbO_4^{3-}[6]. The Raman modes in the low wavenumber region are associated with the translational lattice modes of La (due to its lower mass) and rotational modes of NbO_4^{3-} [35]. Here, the P6 mode at 127.8 and 127.0 cm^{-1} in LVNO-1000 and LVNO-1250 is linked with the translational motion of La atoms in the monoclinic phase. The P8 mode in the higher wavenumber region, located at 858.8 cm^{-1} is the most intense mode, while the intensity of P6 mode enahnced with increase in temperature.

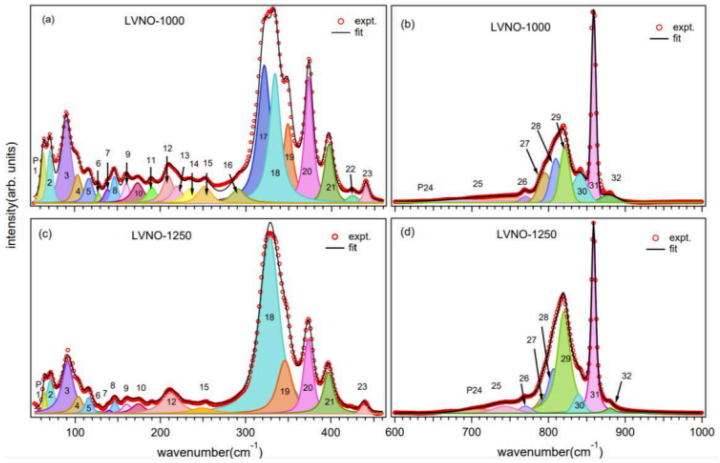


Fig. 5.4: The room temperature Raman spectra of LVNO sample, (a, b) sintered at 1000˚C and (c, d) for sample sintered at 1250˚C in the low and middle wavenumber regions, respectively; fitted using the Voigt peak function and solid thick black line presents the total fit of the measured spectra.

Table 5.3: The peak fitting parameters for the observed vibrational frequencies (ω_{obs}) of the LVNO-1000 and LVNO-1250 samples at room temperature in the wavenumber regions (50–1000 cm^{-1}).

Sample	LVNO-1000	LVNO-1250
Peak	ω_{obs}	ω_{obs}
P1	$A_g(63.8)$	$A_g(64.2)$
P2	$A_g(71.2)$	$A_g(70.9)$
P3	$B_{1u}(90.2)$	$B_{1u}(91.0)$
P4	$B_g(103.5)$	$B_g(103.)$
P5	$B_{1g}(116.7)$	$B_{1g}(115.9)$
P6	$B_g(127.8)$	$B_g(127.0)$
P7	$E_g(138.4)$	$E_g(139.6)$
P8	$A_{2g}(146.8)$	$A_{2g}(146.4)$
P9	$B_g(159.8)$	$B_g(160.6)$
P10	$A_g(173.4)$	$A_g(174.1)$
P11	$A_g(189.8)$	$A_g(189.7)$
P12	$B_g(209.8)$	$B_{1g}(211.9)$
P13	$B_g(219.9)$	
P14	$A_g(232.8)$	
P15	$B_{2g}(251.6)$	$B_{2g}(249.1)$
P16	$B_g(285.6)$	
P17	$A_{1u}(320.0)$	
P18	$A_g(332.0)$	$A_{1g}(328.2)$
P19	$E_g(347.7)$	$E_g(346.2)$
P20	$A_g(373.6)$	$A_g(373.6)$
P21	$B_g(396.9)$	$B_g(397.2)$
P22	$A_g(423.4)$	
P23	$B_g(439.9)$	$B_g(438.5)$
P24	693.3	$A_g(710.3)$
P25	$B_g(747.7)$	$B_g(742.9)$
P26	$A_g(770.0)$	$A_g(769.9)$
P27	$B_g(795.5)$	$B_g(794.4)$
P28	$A_g(809.5)$	$A_g(806.7)$
P29	$A_g(821.1)$	$A_g(820.0)$
P30	$A_g(840.8)$	$A_g(839.3)$
P31	$B_g(858.8)$	$B_g(858.8)$
P32	$B_g(878.5)$	$B_g(880.2)$

Herein, the peak (P12) at 209.8 cm^{-1} assigned to the Ag mode corresponds to the torsional vibration of the VO4 units, with the La atoms remaining nearly stationary. The peaks at 334 cm^{-1} (P17) and 400 cm^{-1} (P20) are attributed to Ag modes associated with the bending vibrations of the O–V–O bonds. Furthermore, the peak observed at 839 cm^{-1} (P30) corresponds to the Ag mode, from the stretching vibrations of the O–V–O bonds. Furthermore, the presence of P8, P9, P10, P13, P14, P15, P17 and P18 modes confirms the existence of VO_4^{3-}ion because none of these modes are visible in $LaNbO_4$ [36]. In addition, there is an enhancement in the integrated intensity (P6) in the LVNO-1250, relative to LVNO-1000 [see Fig. 5.4(b, c)]. This behavior is related to the fact that the increase in the scheelite-tetragonal phase with increasing sintering temperature. These monotonous effects on the vibrational spectra are correlated to the substitution induced deformation of the VO_4^{3-} tetrahedra and is clearly reflected in the FTIR spectra of the LVNO-1250 sample [see Fig. 5.3(a)]. For the LVNO-1000 sample, the effects correspond to the translational vibrations of La–O bonds and the rotational motions of NbO_4^{3-}units. The peaks observed in the intermediate region (250–450 cm^{-1}) are associated with the O–V–O bending vibrations and the scissoring modes of NbO_4^{3-}. Meanwhile, in the high-wavenumber region (600–900 cm^{-1}), the Raman features arise from the stretching modes of Nb–O and V–O bonds. It can be clearly seen in Fig. 4(c) that the number of vibration bonds for LVNO-1250 sample decreases in comparison to the LVNO-1000 sample, which is in agreement with the lower coordination number (8) and the high symmetry (*D2d*) of the La^{3+} ions in the tetragonal phase [13]. In addition, Sun et al. also reported that Raman peaks for the tetragonal $LaVO_4$ are less as compared to the monoclinic $LaVO_4$ due to the high symmetry (*D2d*) of La^{3+} ions, through the theoretical calculations [35].

Furthermore, the x-ray photoemission spectroscopy (XPS) is employed to probe the electronic structure by measuring the survey scan and specific elemental core-level spectra for both the samples. The detected peaks in the survey spectrum are assigned by their binding energies and exhibit strong correlation with the reported values [6], as demonstrated in Fig. 5.5(a). The Nb 3*d* core-level spectra for both the samples confirm the Nb^{5+} oxidation state [37, 38], as shown in Fig. 5.5(b, f). For both the samples, the Nb $3d_{5/2}$ and Nb $3d_{3/2}$ peaks are observed at around 207.3 eV and 210.2 eV, respectively,

with a spin–orbit splitting of around 2.9 eV [39]. The O 1*s* peak [see Fig. 5(e, i)] is observed at 529.8 eV (lattice oxygen) and the energy difference between Nb $3d_{5/2}$ and O 1s is 322.5 eV. The O 1*s* peak, used as the binding-energy reference to compensate for charging effects, is centered at 530.2 eV, giving an energy difference of 322.9 eV between the Nb $3d_{5/2}$ and O 1*s* levels [40]. There is an unidentified contribution at 205.2 eV, shown in pink color in Fig. 5(f). The energy difference of Nb $3d_{5/2}$ and O 1*s* is quite consistent, which reinforces Nb^{+5} oxidation state in both the samples.

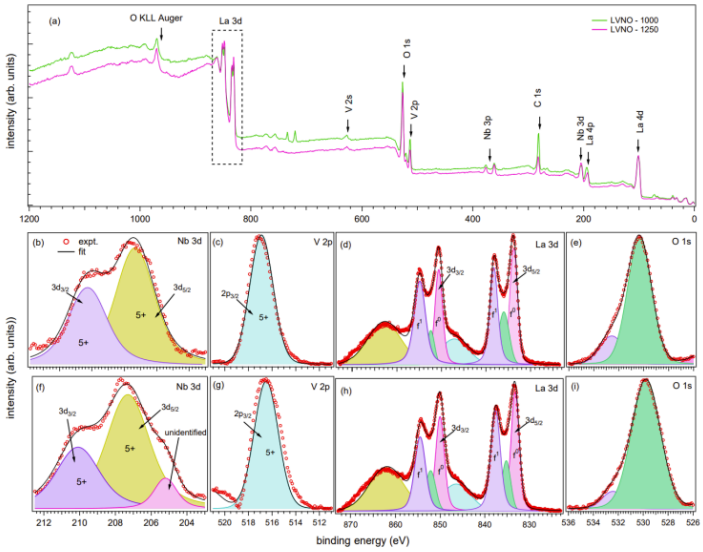


Fig. 5.5: (a) The room temperature XPS survey spectrum; the core level spectra of (b, f) Nb 3*d*; (c, g) V 2*p*; (d, h) La 3*d* and (e, i) O 1*s* elements of the LVNO sample sintered at 1000˚C (b, c, d, e) and 1250˚C (f, g, h, i), respectively.

Also, the V 2*p* core-level spectra for both the samples in Figs. 5.5(c, g), the primary V $2p_{3/2}$ peak occur at 516.9 eV, consistent with V^{5+} oxidation [41]. The La 3*d* core-level spectra for both the samples exhibit the characteristic spin–orbit splitting ($3d_{5/2}$ and $3d_{3/2}$) in Fig. 5.5(d, h). For the LVNO-1000 sample, the primary photoemission peaks are observed at 833.8 eV ($3d_{5/2}$) and 850.6 eV ($3d_{3/2}$), corresponding to a spin–orbit

separation of 16.8 eV [42], confirming the La^{3+} oxidation state [43]. However, a double peak structure is observed in the spin-orbit component, denoted by f^0 and f^1, corresponding to the $3d^9 4f^0$ and $3d^9 f^1 \underline{L}$ configurations, shown in Fig. 5.5(d, h). Here, the L signifies the hole in the O 2*p* valence orbital and arises from the electron transfer from the ligand valence band to empty 4*f* orbitals [37, 44, 45]. In addition to the La 3*d* main peaks, broad satellite features at 847.9 and 862 eV are observed due to the plasmons [6]. For the LVNO-1250 sample, a small shift of 0.6 eV in the main La peaks toward lower binding energy is observed. The primary peaks appear at 833.2 eV ($3d_{5/2}$) and 850.0 eV ($3d_{3/2}$), with a spin–orbit splitting of 16.8 eV, while the corresponding satellite peaks occur at 837.6 eV and 854.5 eV. The energy separation between the primary and satellite peaks, which reflects the degree of metal–ligand orbital overlap [43], is calculated to be around 4.45 eV for both the samples.

Finally, the temperature dependence of dielectric permittivity and dielectric loss of the LVNO samples are shown in Fig. 5.6. The results show a decrease in dielectric permittivity (ϵ_r) with increasing frequency and an increase in permittivity with increasing temperature for both the samples, as shown in Fig. 5.6(a, c). The frequency-dependent behavior of the LVNO samples at selected temperatures can be explained using the space charge polarization mechanism [46–48]. According to this model, at lower frequencies, the charge carriers follow the applied field, which produces a higher amount of polarization, leading to a higher permittivity. The sample sintered at 1250˚C exhibit higher permittivity compared to the one sintered at 1000˚C, as a higher sintering temperature leads to greater densification and larger grain size of the ceramics, which improves the accumulation of charge carriers at the interface. The higher sintering temperature, accompanied by an increase in grain size, results a decrease in insulating grain boundaries, leading to an increase in polarization and, consequently, dielectric permittivity [49, 50]. The higher amount of polarization gives rise to a large permittivity, as observed for the sample sintered at 1250˚C [51, 52]. The temperature-dependent variations in permittivity are explained in terms of thermal activation of charge carriers. As the temperature is increased at a fixed frequency, the thermal energy associated with the dipoles helps them to orient along the direction of the applied field; hence, the dielectric permittivity is increased with an increase in temperature. The total

dielectric permittivity is the combined effect of the applied frequency and measured temperature. A similar type of temperature-dependent behavior is also observed for the dielectric loss data, as shown in Figs. 5.6(b, d). The lower dielectric loss at higher sintering temperature is attributed to the greater densification (as porosity leads to dissipating the energy in dielectric materials) of the ceramics and a decrease in oxygen vacancies. An increase in dielectric loss with temperature is due to an increase in space charge polarization, which leads to an increase in conductivity of the ceramic samples, hence an enhancement in the dielectric loss. The dielectric loss at high temperature is mainly attributed to the conduction loss. The frequency-dependent dielectric loss data show an increase in dielectric loss above 100 kHz, indicating that the resonance frequency for the LVNO molecule is above 100 kHz. The comparison of dielectric permittivity Fig. 5.6(e) and dielectric loss Fig. 5.6(f) shows a higher permittivity and lower dielectric loss for sample sintered at 1250˚C.

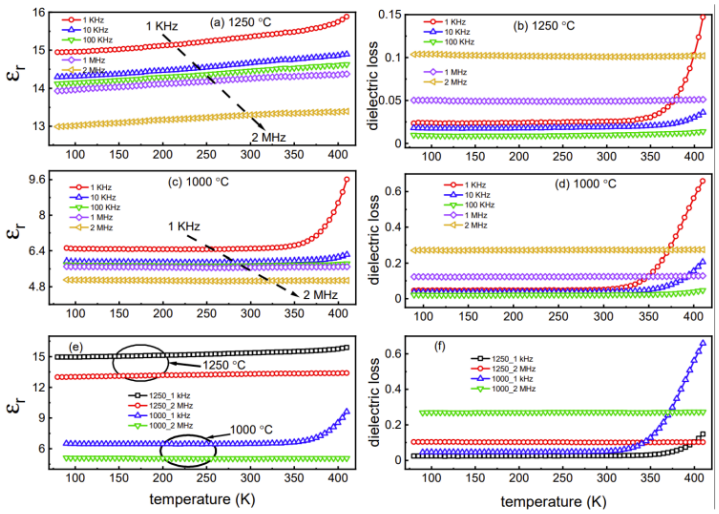


Fig. 5.6: The variations of electric permittivity (ϵ_r) and dielectric loss at various temperatures for selected frequencies for both the samples, sintered 1000˚C and 1250˚C temperatures; (a-d) the variations of electric permittivity and dielectric loss at various temperatures, (e-f) a comparison of electric permittivity and dielectric loss at two different frequencies of 1 kHz and 2 MHz, respectively. The arrow in this figure shows the direction of increasing frequency.

Moreover, the variation of real (Z′) and imaginary (Z″) parts of total impedance at selected temperatures is shown in Fig. 5.7.

The impedance data are normalized by the geometrical correction factor A/d , where A is the total electrode area and d is the thickness of the sample. The real part of impedance (Z′) is categorized into two: (a) frequency-dependent data at lower frequencies related to the a.c. conduction in the material gives a rapid decrease in the impedance due to the interfacial polarization, and (b) merging of all curves with each other indicates the possible release of space charge due to reduction in potential barriers. The rapid decreasing behavior of the real impedance with frequency is due to an enhancement in the mobility of charge carriers [53]. The analysis shows that the real part of the total impedance (Z′) increases with temperature, indicating the enhancement in the resistive nature of the LVNO samples, see Fig. 5.7(a, c). The imaginary part (Z″) decreases with temperature or nearly remains the same with temperature, indicating no variations in the capacitive nature of the samples, see Fig. 5.7(b, d). The higher values of impedance at lower frequencies are due to interfacial polarization, where the capacitive nature of the samples dominates according to the time constant and temperature of the samples. The sample sintered at 1250˚C show the lower values of real impedance (Z′), indicating the better crystalline nature of the sample having the lower porosity with larger grain size [54], as supported by the dielectric permittivity and loss data shown in Fig. 5.6.

Note that the *a.c.* conductivity is a response of the carriers in phase with the applied electric field, which depends on the frequency of the applied field and temperature. It is a combined response of relaxation, localized hopping and diffusion of charge carriers. The variation in conductivity with frequency is a crucial tool for determining the type of carriers that dominate in the total conductivity. If the conductivity increases (decreases) with an increase in frequency, the conductivity is dominated by the contributions from the bound (free) charge carriers [46, 55–57]. In an alternating electric field, the charge carriers move from one state to another by a hopping conduction. At lower frequencies, carriers undergo long-range hopping due to the considerable time period available to them; in contrast, a shorter time period at higher frequencies results in short-range hopping. The hopping probability increases with temperature due to an increase in the

activation energies of carriers as well as a reduction in barrier height, resulting in an increase in conductivity. The *a.c.* conductivity, depends also on the sample dimensions, can be calculated using the following relation [56–58]:

$$\sigma_{ac}(\omega) = t/A[Z'/(Z'^2 + Z''^2)] \quad (3)$$

Here, t is the thickness of the dielectric material, A is the total area of the metal electrodes, Z′ and Z″ are the real and imaginary impedance of the total impedance Z.

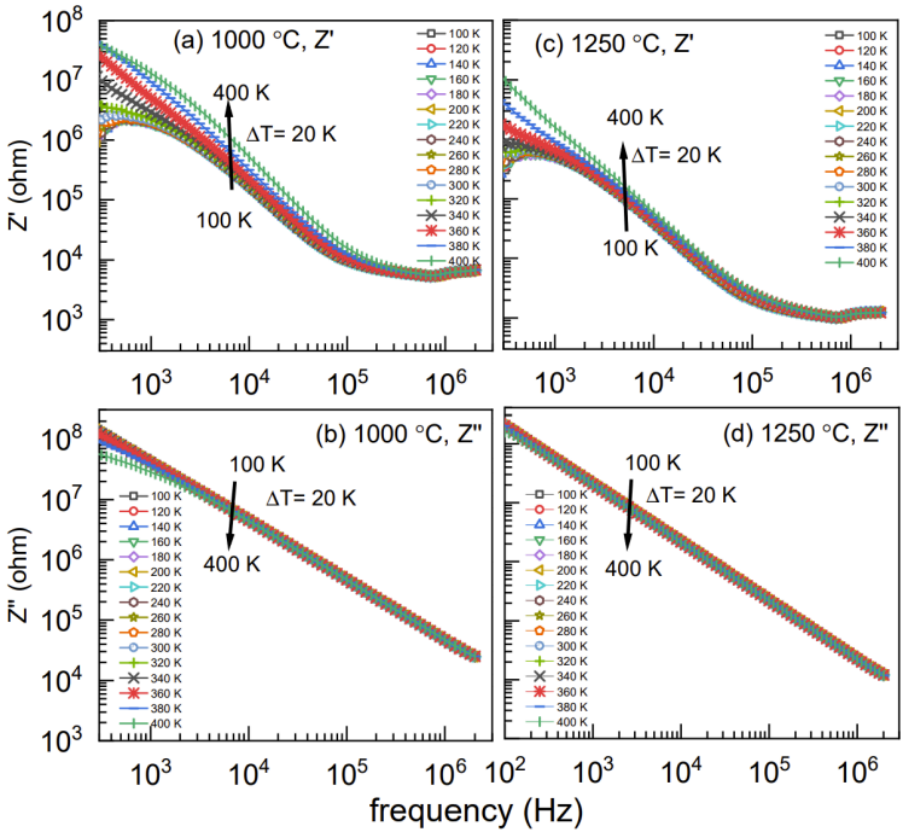


Fig. 5.7: The real (Z′) and imaginary (Z″) parts of total impedance (Z), (a, b) for the LVNO-1000 and (c, d) for the LVNO-1250 samples. The arrow shows the direction of increasing temperatures.

Further, the *a.c.* conductivity calculated using equation 3 is shown in Fig. 5.8 at selected temperatures. The conductivity is found to increase with an increase in temperature due

to the thermal activation of charge carriers; however, the conductivity remains in a similar order for samples sintered at 1000˚C and 1250˚C. It is found that conductivity increases with frequency for both the samples, confirming the contributions from the bound charge carriers. The conductivity data show two different types of regions: (a) a plateau-like region at lower frequencies and (b) dispersive type behavior at higher frequencies. This type of frequency-dependent variation in conductivity is explained on the basis of the Funke jump relaxation model [59]. According to this model, charge carriers follow long-range motion at lower frequencies, resulting in a frequency-independent contribution. On the other hand, at higher frequencies, the dispersive nature is due to the competition between successful and unsuccessful hopping due to the shorter time period available with carriers. The analysis shows that the discrete nature of conductivity at lower frequencies is due to the accumulation of space charge over the potential barriers, while the merging of the conductivity data at higher frequencies for both the samples confirm the reduction of potential barriers at higher frequencies due to the possible release of space charge. The sample sintered at 1000˚C exhibits a large dispersive nature, as small grain size and lower densification result in a large potential barrier, thereby increasing the ratio of unsuccessful hopping to successful hopping. On the other hand, sample sintered at 1250˚C exhibit a larger grain size and higher densification, resulting in a higher amount of successful hopping over potential barriers, thus a decrease in dispersive behavior is observed. The analysis also shows that the dispersive nature shifts towards the higher frequency side with an increase in temperature for both the samples, which can be explained by the enhancement in thermal activation energy available with the carriers. At higher frequencies, lesser time scale leads to the unsuccessful hopping of carriers towards neighboring sites. As the temperature increases, the average thermal energy available to carriers is enhanced, allowing long-range hopping even for the shorter periods available at higher frequencies. The long-range hopping extends the dispersive nature towards the higher frequency side with an increase in temperature for both the samples [55, 60, 61].

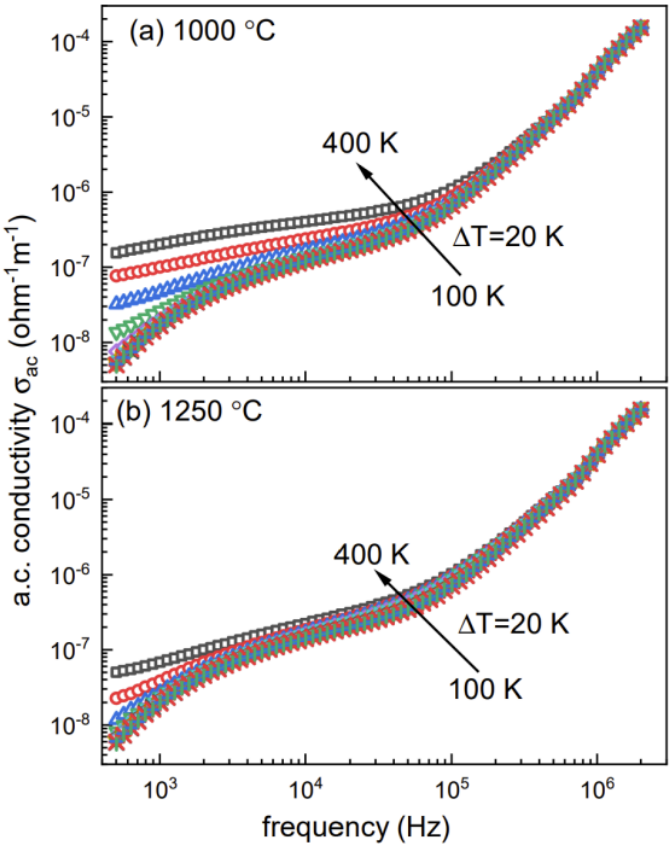


Fig. 5.8: The variation of ac conductivity with frequency for (a) 1000˚C and (b) 1250˚C sintered samples. The arrow shows the direction of increasing temperature.

5.4 Conclusions

The $LaV_{0.5}Nb_{0.5}O_4$ samples were successfully synthesized via the conventional solid-state reaction route. A pronounced dependence of the physical and dielectric properties on the sintering temperatures 1000˚C and 1250˚C has been observed. The room-temperature Rietveld refinement of the powder X-ray diffraction patterns reveal an increase in the tetragonal phase fraction to 96%, accompanied by a minor monoclinic phase fraction of 4%, upon sintering at 1250˚C. The FE-SEM analysis illustrates the surface morphology, which indicates a clear increase in particle size with increasing sintering temperature. The high-resolution transmission electron microscopy further confirms the crystallinity and coexistence of mixed phases in both the samples. The

Raman and Fourier transform infrared spectroscopy measurements validate the presence of the characteristic vibrational modes. The UV–vis diffuse reflectance spectroscopy indicates an optical band gap of 3.2 eV for the sample sintered at 1000˚C; however, as the tetragonal phase becomes more prominent at 1250˚C, the band gap narrows to 2.7 eV, which is advantageous for luminescent applications. The x-ray photoemission spectroscopy reveals the electronic structure and confirms the valence state of the constituent elements. Lastly, the dielectric studies reveal that the sample annealed at 1250˚C exhibits higher dielectric permittivity (ϵr) and lower dielectric loss. These results clearly demonstrate that the sintering temperature plays a crucial role in tailoring the physical, electronic, and dielectric properties of $LaV_{0.5}Nb_{0.5}O_4$ orthovanadate.

Chapter 6

Conclusion, Future Scope and Social Impact

6.1 Conclusion

The present research work focuses on understanding the effect of Nb substitution on the structural, vibrational, dielectric, and electrical properties of lanthanum orthovanadate based ceramics.

The study systematically investigates phase evolution, dielectric relaxation, impedance behaviour, and conduction mechanisms in $LaV_{1-x}Nb_xO_4$ ($0 \leq x \leq 1$) compounds prepared using the conventional solid-state reaction method. The obtained results demonstrate that controlled Nb incorporation significantly modifies the crystal structure, local lattice environment, and functional response of the material system. The findings of this work provide useful insight into the role of chemical pressure and defect engineering in tailoring multifunctional oxide ceramics for advanced technological applications. Furthermore, the present investigation highlights the possibility of utilizing rare-earth orthovanadates in high-k dielectric devices, electrochemical systems, sensors, and other electronic applications requiring stable dielectric and electrical performance. The detailed structural and impedance analysis carried out in this study establishes a clear relationship between phase transformation, defect formation, and electrical transport behaviour in Nb substituted $LaVO_4$ ceramics.

$LaV_{1-x}Nb_xO_4$ (x = 0 to 1) ceramics with different Nb concentrations were successfully synthesized through the conventional solid-state reaction route followed by controlled calcination and sintering. The structural analysis carried out using X-ray diffraction and Rietveld refinement confirmed gradual phase evolution from monoclinic monazite phase to tetragonal scheelite phase and finally towards monoclinic fergusonite phase with increasing Nb concentration. The observed structural transformation was mainly associated with ionic size mismatch between V^{5+} and Nb^{5+}, which introduced internal chemical pressure and lattice distortion within the crystal framework. Raman spectroscopic studies further supported the structural transition and indicated changes in

local symmetry, bonding environment, and vibrational characteristics of the material system.

Microstructural investigations using SEM and HR-TEM revealed significant variation in grain morphology, crystallite size, and grain boundary distribution with increasing Nb content. The incorporation of Nb generated microstructural disorder and lattice strain, which strongly influenced the dielectric and electrical properties of the ceramics. XPS analysis confirmed the presence of V^{5+}, Nb^{5+}, and oxygen vacancy related defect states. These defect states were found to play an important role in charge transport, dielectric polarization, and relaxation mechanisms within the material system.

Dielectric measurements performed over a wide frequency and temperature range showed strong dependence of dielectric constant and dielectric loss on composition, frequency, and thermal conditions. Nb substituted samples exhibited improved dielectric response and better frequency stability compared to pure $LaVO_4$. The enhancement in dielectric permittivity was mainly associated with increased lattice polarizability and interfacial polarization caused by oxygen vacancies and grain boundary effects. The dielectric relaxation behaviour was found to be non-Debye in nature, indicating the existence of distributed relaxation processes within the ceramics. Maxwell–Wagner polarization and space charge polarization were observed to contribute significantly at lower frequencies and elevated temperatures.

Complex impedance spectroscopy studies confirmed the electrically heterogeneous nature of the polycrystalline ceramics. Separate grain and grain boundary contributions were clearly observed in Nyquist plots. The frequency-dependent conductivity behaviour followed Jonscher's universal power law, suggesting thermally activated hopping conduction mechanisms. A gradual reduction in activation energy with increasing Nb concentration indicated enhanced charge carrier mobility and improved electrical conduction. The conduction process was mainly governed by small polaron hopping assisted by oxygen vacancies and local structural distortion. The combined modulus and impedance analysis also provided detailed understanding of dielectric relaxation and charge carrier dynamics in the prepared ceramics.

The present study further revealed that Nb substitution modifies the electronic structure of $LaVO_4$ by influencing the interaction among Nb-4d, V-3d, and O-2p orbitals. These changes resulted in bandgap tuning and enhanced electronic delocalization, which affected both dielectric and electrical transport behaviour.

Further, the $LaV_{0.5}Nb_{0.5}O_4$, with samples annealed at 1000°C and 1250°C examined for their thermal treatment impacts. Structural analysis of these samples through X-ray diffraction (XRD) reveals the coexistence of monoclinic monazite-type and tetragonal scheelite-type phases, noting how higher sintering temperatures increase the tetragonal phase fraction and improve crystallinity. Further, the coexistence of monazite, scheelite, and fergusonite phases provides additional flexibility for tailoring the material properties according to specific application requirements.

Overall, the present investigation establishes that controlled Nb substitution is an effective approach for engineering the structural and functional properties of lanthanum orthovanadate based ceramics $LaV_{1-x}Nb_xO_4$ ($0 \leq x \leq 1$). The improved dielectric response, stable electrical characteristics, and tunable phase behaviour make these materials promising candidates for dielectric capacitors, sensors, photocatalytic systems, and advanced electronic devices.

6.2 Future Scope and Social Impact

The present work opens several possibilities for further research on rare-earth orthovanadate based multifunctional ceramics. Future investigations may focus on experimental optimization of synthesis conditions in order to achieve better phase purity, controlled grain growth, and reduced defect concentration. Additional studies involving thin-film fabrication, rare-earth codoping, and nano-structuring may further improve the dielectric and electrical performance of $LaVO_4$-based materials. Detailed optical and photocatalytic investigations can also be carried out to explore the applicability of these ceramics in visible-light driven environmental and energy-related applications. Furthermore, advanced theoretical calculations and firstprinciples studies

may help in understanding the role of defect states, electronic band structure, and charge transport mechanisms at the atomic level.

The impedance and dielectric behaviour observed in the present study suggest that these materials may be useful for high-frequency dielectric devices, electrochemical systems, and sensor technologies. Future work may therefore focus on device fabrication and performance evaluation under practical operating conditions. The role of oxygen vacancies and defect engineering in controlling conductivity and polarization behaviour can also be explored in greater detail for developing advanced functional oxide ceramics.

From a broader perspective, the development of efficient dielectric and multifunctional oxide materials is important for next-generation electronic technologies and sustainable energy systems. Materials with stable dielectric response and improved electrical performance can contribute toward the fabrication of energy-efficient electronic components and miniaturized devices. The use of rare-earth orthovanadate based ceramics in sensors, capacitors, and electrochemical systems may also support technological advancement in communication, energy storage, and environmental monitoring sectors.

The findings of the present work are expected to contribute toward scientific progress in the field of functional oxide materials and advanced ceramics. Hence, development of such materials can promote indigenous research, strengthen materials science-based technologies, and support sustainable industrial growth. In addition, the advancement of multifunctional ceramics with improved electrical and dielectric performance aligns with the global objective of developing environmentally stable, energy-efficient, and technologically advanced material systems for future applications.

Followings scope may be explored in the field of functional oxide material and advanced ceramic materials like $LaV_{1-x}Nb_xO_4$ series-

1. Nanoscale Engineering: Synthesizing $LaV_{1-x}Nb_xO_4$ nanoparticles via sol-gel, hydrothermal, or microwave-assisted methods may expose more active sites and reduce interfacial impedance.

2. Green and Sustainable Synthesis: Eco-friendly methods like combustion synthesis using plant extracts, urea-based combustion, and citrate-nitrate routes can be explored to reduce energy consumption and environmental impact.
3. Thin Films and Device Fabrication: Integrating these materials as thin films using pulsed laser deposition (PLD), spin coating, or sputtering may lead to applications in MEMS, sensors, and micro capacitors.
4. Multifunctional Composites: Forming composites with CeO_2, $GdVO_4$, ZnO, or graphene oxide could enable synergistic behaviour for multifunctionality (photocatalysis + sensing).
5. Theoretical Modelling: First-principles DFT calculations on defect formation energy, phonon dispersion, and charge density difference plots can further guide experimental efforts.
6. Gas Sensing and Humidity Detection: Testing $LaV_{1-x}Nb_xO_4$ for CO, NO_2, NH_3, and H_2 detection via impedance modulation and surface adsorption analysis under real-time conditions.
7. Doping with Rare-Earth Ions: Co-doping with Nd^{3+}, Sm^{3+}, and Gd^{3+} could enhance dielectric non-linearity, increase permittivity, or introduce tunable emission.
8. Machine Learning for Property Prediction: Data-driven prediction of optimal compositions and processing parameters using ML regression models.
9. Radiation-Hardened Applications: Investigation of stability under ionizing radiation for potential space or nuclear industry applications.

PhD_Thesis_Ashok_Kumar_combined_for_plag_check.pdf

ORIGINALITY REPORT

3%	1%	2%	1%
SIMILARITY INDEX	INTERNET SOURCES	PUBLICATIONS	STUDENT PAPERS

MATCH ALL SOURCES (ONLY SELECTED SOURCE PRINTED)

< 1%

★ dspace.lboro.ac.uk

Internet Source

Exclude quotes	On	Exclude matches	< 14 words
Exclude bibliography	On		

PhD_Thesis_Ashok_Kumar_combined_for_plag_check.pdf

GRADEMARK REPORT

FINAL GRADE

/0

GENERAL COMMENTS

PAGE 1

PAGE 2

PAGE 3

PAGE 4

PAGE 5

PAGE 6

PAGE 7

PAGE 8

PAGE 9

PAGE 10

PAGE 11

PAGE 12

PAGE 13

PAGE 14

PAGE 15

PAGE 16

PAGE 17

PAGE 18

PAGE 19

PAGE 20

PAGE 21

PAGE 22

PAGE 23

PAGE 24

PAGE 25

PAGE 26

PAGE 27

PAGE 28

PAGE 29

PAGE 30

PAGE 31

PAGE 32

PAGE 33

PAGE 34

PAGE 35

PAGE 36

PAGE 37

PAGE 38

PAGE 39

PAGE 40

PAGE 41

PAGE 42

PAGE 43

PAGE 44

PAGE 45

PAGE 46

PAGE 47

PAGE 48

PAGE 49

PAGE 50

PAGE 51

PAGE 52

PAGE 53

PAGE 54

PAGE 55

PAGE 56

PAGE 57

PAGE 58

PAGE 59

PAGE 60

PAGE 61

PAGE 62

PAGE 63

PAGE 64

PAGE 65

PAGE 66

PAGE 67

PAGE 68

PAGE 69

PAGE 70

PAGE 71

PAGE 72

PAGE 73

PAGE 74

PAGE 75

PAGE 76

PAGE 77

PAGE 78

PAGE 79

PAGE 80

PAGE 81

PAGE 82

PAGE 83

PAGE 84

PAGE 85

PAGE 86

PAGE 87

PAGE 88

PAGE 89

PAGE 90

PAGE 91

PAGE 92

PAGE 93

PAGE 94

PAGE 95

PAGE 96

PAGE 97

PAGE 98

PAGE 99

PAGE 100

PAGE 101

PAGE 102

PAGE 103

PAGE 104

PAGE 105

PAGE 106

PAGE 107

PAGE 108

PAGE 109

PAGE 110

PAGE 111

PAGE 112

PAGE 113

PAGE 114

PAGE 115

PAGE 116

PAGE 117

PAGE 118

PAGE 119

PAGE 120

PAGE 121

PAGE 122

PAGE 123

PAGE 124

PAGE 125

PAGE 126

PAGE 127

PAGE 128

PAGE 129

PAGE 130